

Optimalisering av ringledning for Peltonturbin

Bjørn Winther Solemslie

Master i produktutvikling og produksjon
Oppgaven levert: Juni 2010
Hovedveileder: Torbjørn Kristian Nielsen, EPT

Oppgavetekst

Bakgrunn:

Under prosjektoppgaven ble det gjennomført målinger av tapsforhold i en ringledning for en Peltonturbin. Ringledningen er langt fra optimal.

I Masteroppgaven skal det designes en mer optimal ringledning. Videre skal det måles et komplett Hill-diagram for turbinen med det skovlesette som er montert. Hydro Energi vil levere et visst antall skovlesett hvor bestpunktvirkningsgraden måles og sammenlignes med opprinnelige skovlesett.

Mål:

Optimalisere ringledningen for Peltonturbin og måle komplett Hill-diagram for turbinen med eksisterende skovlesett og bestpunktvirkningsgrad for et antall skovlesett.

Oppgaven bearbeides ut fra følgende punkter:

1. Utrede kriterier for optimal design av ringledninger, analysere eksisterende ringledning og foreslå endringer.
2. Måle et komplett Hill-diagram for eksisterende løpehjul.
3. Måle bestpunktvirkningsgrad for andre skovlesett
4. Hvis tiden tillater, måle Hill-diagram for det beste skovlesettet.

Oppgaven gitt: 18. januar 2010

Hovedveileder: Torbjørn Kristian Nielsen, EPT

MASTEROPPGAVE

for

Stud.techn. Bjørn Winther Solemslie

Våren 2010

Optimalisering av ringledning for Peltoneturbin *Optimization of distribution system for a Pelton turbine*

Bakgrunn

Under prosjektoppgaven ble det gjennomført målinger av tapsforhold i en ringledning for en Peltoneturbin. Ringledningen er langt fra optimal.

I Masteroppgaven skal det designes en mer optimal ringledning. Videre skal det måles et komplett Hill-diagram for turbinen med det skovlsettet som er montert. Hydro Energi vil levere et visst antall skovlsett hvor bestpunktvirkningsgraden måles og sammenlignes med det opprinnelige skovlsettet.

Mål

Optimalisere ringledningen for Peltoneturbin og måle komplett Hill-diagram for turbinen med eksisterende skovlsett og bestpunktvirkningsgraden for et antall skovlsett.

Oppgaven bearbeides ut fra følgende punkter

1. Utrede kriterier for optimal design av ringledninger, analysere eksisterende ringledning og foreslå endringer
2. Måle et komplett Hill-diagram for eksisterende løpehjul
3. Måle bestpunktvirkningsgrad for andre skovlsett
4. Hvis tiden tillater, måle Hill-diagram for det beste skovlsettet

---- " ---

Senest 14 dager etter utlevering av oppgaven skal kandidaten levere/sende instituttet en detaljert fremdrift- og eventuelt forsøksplan for oppgaven til evaluering og eventuelt diskusjon med faglig ansvarlig/veiledere. Detaljer ved eventuell utførelse av dataprogrammer skal avtales nærmere i samråd med faglig ansvarlig.

Besvarelsen redigeres mest mulig som en forskningsrapport med et sammendrag både på norsk og engelsk, konklusjon, litteraturliste, innholdsfortegnelse etc. Ved utarbeidelsen av teksten skal kandidaten legge vekt på å gjøre teksten oversiktlig og velskrevet. Med henblikk på lesning av besvarelsen er det viktig at de nødvendige henvisninger for korresponderende steder i tekst, tabeller og figurer anføres på begge steder. Ved bedømmelsen legges det stor vekt på at resultatene er grundig bearbeidet, at de oppstilles tabellarisk og/eller grafisk på en oversiktlig måte, og at de er diskutert utførlig.

Alle benyttede kilder, også muntlige opplysninger, skal oppgis på fullstendig måte. For tidsskrifter og bøker oppgis forfatter, tittel, årgang, sidetall og eventuelt figurnummer.

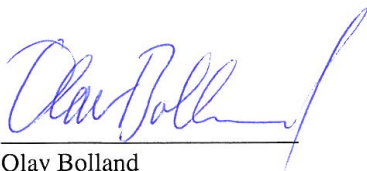
Det forutsettes at kandidaten tar initiativ til og holder nødvendig kontakt med faglærer og veileder(e). Kandidaten skal rette seg etter de reglementer og retningslinjer som gjelder ved alle (andre) fagmiljøer som kandidaten har kontakt med gjennom sin utførelse av oppgaven, samt etter eventuelle pålegg fra Institutt for energi- og prosesssteknikk.

I henhold til ”Utfyllende regler til studieforskriften for teknologistudiet/sivilingeniørstudiet” ved NTNU § 20, forbeholder instituttet seg retten til å benytte alle resultater og data til undervisnings- og forskningsformål, samt til fremtidige publikasjoner.

Ett -1 komplett eksemplar av originalbesvarelsen av oppgaven skal innleveres til samme adressat som den ble utlevert fra. Det skal medfølge et konsentrert sammendrag på maksimalt én maskinskrevet side med dobbel linjeavstand med forfatternavn og oppgavetittel for evt. referering i tidsskrifter).

Til Instituttet innleveres to - 2 komplette kopier av besvarelsen. Ytterligere kopier til eventuelle medveiledere/oppnavigivere skal avtales med, og eventuelt leveres direkte til de respektive. Til instituttet innleveres også en komplett kopi (inkl. konsentrerte sammendrag) på CD-ROM i Word-format eller tilsvarende.

NTNU, Institutt for energi- og prosesssteknikk, 12. januar 2010



Olav Bolland
Instituttleder



Torbjørn K. Nielsen
Faglig ansvarlig/veileder

Preface

During the work on this thesis I've learnt a lot about experimental work and CFD simulations. Much of the knowledge about the two topics has been gained by trial and error. Assembling and instrumenting the test rig has been time consuming since I didn't always know what end to begin in. Without the help of Joar Hilstad, Trygve Opland, Halvor Haukvik and Per Eivind Helmersen in the laboratory the experiments would not have been possible to carry out.

The mixture of theoretical and lab work during this thesis has been an enjoyable setting which has allowed me practice my fascination for both lines of work. The opportunity to expand my knowledge within AutoDesk Inventor, LabView, MATLAB, ANSYS Workbench and CFX as well as learning some SolidWork has been one of the more enjoyable experiences in my academic career. The openness of professors towards discussing problems that arose during the work has also been a source of inspiration. I would like to thank the scientific staff and especially my supervisor Tobjørn K. Nielsen for the help and guidance I've received while solving issues that emerged.

In addition I would like to thank the rest of the staff and students at Vannkraftlaboratoriet for a great learning and social environment. Especially the scientific assistant Mette Eltvik for her endless patience and knowledge when it comes to ANSYS and CFX. A special thanks goes to

Ramus Næss Haugli for his good talks and discussions around problems and the good talks about nothing. In addition, I would like to thank Sindre Lavik Gidskehaug for his good company in the small hours of the night and the good discussions both academic and about life in general. Last but not least I would like to thank my girlfriend, Elisabeth Varsi Stubbrud, for the good discussions and for having a finished dinner to coming home to when days got long.

Bjørn W. Solemslie

Bjørn Winther Solemslie
Trondheim, July 14, 2010

Sammenheng

Hydroenergi er en norsk produsent av vannturbiner med godt etablert kunnskap innen Kaplan og Francis turbiner. Selskapet har designet flere Pelton skovler med det mål å redusere kavitasjon. Selskapet ønsket å finne et fullstendig Hill-diagram for en av skovlene på en 5 jets Pelton turbin. Andre design skulle bli testet i beste punktet og sammenlignet med nevnte design. I tillegg ønsket de å undersøke optimal design av ringledningen for turbinen.

Tester ble utført ved Vannkraftlaboratoriet ved NTNU. Grunnet flere havari i løpet av testperioden ble antall forsøk redusert til kun å finne Hill-diagram som et av designene. Det designet som skulle testes fullt ut ble ødelagt i et av havariene etter at tester med 1 dyse åpen var fullført. De ble erstattet med skovler med samme geometri men med en 2° høyere pitch vinkel. Effekten av den økte pitch vinkelen kunne ikke tallfestes. Sammenligning av tester gjort med 1 og 2 dyser indikerer derimot en mulig innvirkning på plasseringen av beste punkter med hensyn til rotasjonshastighet.

Et sett av kriterier for optimal design av ringledningen ble funnet og den opprinnelige ringledningen ble redesignet for å møte disse. De redesignede ringledningene gjennomgikk simuleringer i *Computational Fluid Dynamics* (CFD) basert på tidligere simulering av den opprinnelige ringledningen som er verifisert med eksperimenter. Simuleringene viste en forbedring av falltap ringledningen. I utløpet til dysene ble det observert ugunstig strømming, men dette er antatt å være grunnet feil i modellen.

Den hydrauliske virkningsgraden til de testede skovlene ble funnet å være lavere enn på de beste Pelton-turbinene på markedet.

Abstract

The hydro power turbine producer Hydroenergi is well established knowledge base within Kaplan and Francis turbines. The company aims to improve the knowledge within Pelton turbines but have struggled with cavitation problems. They have therefor produced multiple designs of Pelton buckets with the aim to reduce cavitation. The company wanted to establish complete Hill diagram of a bucket design on a 5 jet Pelton turbine. Other designs were to be tested at the best point of efficiency against the said design. In addition they wished to investigate optimal distributor design. Tests were done at Vannkraftlaboratoriet at NTNU. Because of multiple failures during the experiments they were reduced to only include a crude Hill diagram for one of the designs. The buckets that were to be tested fully were destroyed in a breakdown after the test with 1 nozzle was completed. They were replaced with buckets with the same geometry but with a 2° higher pitch angle. The effect of this pitch angle increase was not quantified but the results indicate that it may have an effect on the location of the best point of efficiency with regard to rotational speed.

A set of conditions for distributor design were found and the original distributor was redesigned to meet these. The redesigned distributor underwent *Computational Fluid Dynamics* (CFD) simulations based on a previously simulation of the original distributor verified with experiments. The simulations showed an improvement in the losses in the distributor but also included unreliabilities due to modeling errors.

The hydraulic efficiency of the buckets tested was found to be lower than state of the art Pelton turbines.

Contents

Preface	i
Sammendrag - Norwegian	iii
Abstract	v
Table of content	xi
List of Figures	xvii
List of Tables	xix
Nomenclature	xxi
1 Introduction	1
2 Theory	3
2.1 Optimization of Pelton Turbine Parameters	3
2.1.1 Optimal Rotational Speed	3
2.1.2 Optimal Bucket Dimensions	5
2.1.3 Optimal Pelton Distributor Design	5
2.2 Model Testing	7
2.3 Hydraulic Efficiency	8
2.4 Distributor Optimization	9

3	Background	13
3.1	Summary of Previous Efficiency Experiments	13
3.1.1	Efficiency Test with 5 Nozzles	13
3.1.2	Efficiency Test of Different Bucket Sizes with 1 Nozzle	14
3.2	Summary of Previous Head Loss Experiments	16
3.3	Summary of Previous Simulations	18
4	Experimental Setup and Methode	21
4.1	Instrumentation	22
4.1.1	Volume Flow Measurement	24
4.1.2	Torque and Rotational Speed Measurement	24
4.1.3	Pressure Measurement	24
4.1.4	Temperature Measurement	25
4.2	Calibration	26
4.2.1	Volume Flow Meter	26
4.2.2	Torque Transducer	27
4.2.3	Differential Pressure Transmitter	28
4.3	Problems Encountered dring the Experiments	29
4.4	Designing the Test Matrix	30
4.5	Adjustment of Static Head during the Experiments	31
4.6	Post Processing of Data from the Experiments	32
5	Optimization of the Distributor	33
5.1	Optimization of the Throat	35
5.2	Additional Primitive Guide Vanes	35
5.3	Change of the Throat Length and Position	36
6	Simulation	39
6.1	CAD-Modeling	39
6.2	Meshing	40
6.3	Simulation and Boundary Conditions	42

7	Uncertainty Analysis	45
7.1	Uncertainty in Experiments	45
7.2	Propagation of Uncertainties	45
7.3	Uncertainties in the Calibration	45
7.4	Uncertainty of the Tests	50
7.4.1	Total Uncertainty of each Component	50
7.4.2	Uncertainty in the Differential Pressure Measurements	51
7.4.3	Uncertainty in the Volume Flow Measurements	52
7.4.4	Uncertainty in the Torque Measurements	53
7.4.5	Uncertainty in the Temperature Measurements	53
7.4.6	Uncertainty in Calculating Density of Water	54
7.4.7	Uncertainty in the Rotational Speed Measurement	54
7.4.8	Total Uncertainty for the Hydraulic Efficiency	54
8	Results	57
8.1	Results from the Experiments	57
8.2	Results from the Simulations	65
9	Discussion	73
9.1	Hill Diagram	73
9.2	Effect of Increased Pitch Angle	76
9.3	Effect of Lowered Effective Head	79
9.4	Optimal Distributor Design	79
10	Conclusion and Further Work	81
	Bibliography	84
A	Instrumentation	85
A.1	Torque measurement	85
A.2	Rotational Speed measurement	85
A.3	Volumetric Flow measurement	88

B Calibration	91
B.1 Torque Calibration	92
B.2 Calibration of the Volume Flow Meter	93
B.2.1 Substitution Calibration Procedure	94
C Distributors After Optimization	101
D Uncertainty Analysis	105
D.1 Systematic errors	107
D.2 Random errors	108
D.3 Method for Finding Regression Errors	110
D.4 Propagation of uncertainties	112
D.5 Errors in the Calibration	113
D.5.1 Errors in the Calibration of the Volume Flow Meter	113
D.5.2 Errors in the Calibration of the Torque Transducer .	115
D.6 Errors in the measurements	115
D.6.1 Errors in the Volume Flow Measurements	116
D.6.2 Errors in the Temperature Measurements	116
D.6.3 Errors in the Torque Measurements	117
E Frequency and Nozzle House Failure	119
E.1 Frequency Converter Failure	119
E.2 Nozzle Housing Failure and Repair	119
F Results	125
F.1 Experimental results	125
F.2 Simulation results	129
G Matlab Code	133
G.1 Matlab Code for Importing Data	134
G.2 Matlab Code for Creating Hill-Diagram	138
H Calibration Certificates	143
H.1 GE Druck P3223-1	143
H.2 SeaBird SBE 38	150

H.3 Weight used during the calibration of the torque transducer	152
---	-----

List of Figures

2.1	Velocity diagram for a Pelton turbine [1]	4
2.2	Traditional Pelton distributor made up of short pipe sections fabricated from steel plates [4]	6
2.3	Schematic figure of a Pelton machine [4]	9
3.1	Hydraulic Efficiency at near constant $n_{11} = 41.5$	14
3.2	Relation between hydraulic efficiency and efficient head [11]	15
3.3	Hydraulic Efficiency for the large (a), medium (b) and small (c) bucket [11]	16
3.4	The distributor with the main pipe and the outlet to nozzle 1 indicated	18
3.5	Head loss from previous experiments with uncertainty and head loss from simulations at 60% nozzle opening. Corrected version of [12] where the uncertainty shown is relative but should be absolute.	19
3.6	Discharge due to throat over nozzle outlet and equal discharge at 60% nozzle opening, [12]	19
3.7	Absolute Velocity through the Distributor	20
4.1	Experimental Setup	22
4.2	Schematic overview of the instrument setup	23
4.3	Instrument location on test rig	23

4.4	Fuji FKKW37V differential pressure transducer (a) and the ring manifold pressure outtake (b)	25
4.5	Calibration curve for volume flow meter	26
4.6	Setup for torque transducer calibration	27
4.7	Calibration curve for torque transducer	28
4.8	Calibration curve for the differential pressure transmitter . .	29
5.1	Schematic drawing of the distributor	34
5.2	The nozzle outlet with the cut producing the primitive guide vane indicated.	36
5.3	Nozzle 1 (a) and nozzle 4 (b)	37
5.4	Outlet to nozzle 3 as on the throat optimized distributor (a), when it was changed to mimic that at nozzle 1 (b) and nozzle 4 (c)	37
5.5	Pressure contour at nozzle 3	38
6.1	CAD-model of distributor (a) and CAD-model of water filled volume (b)	40
6.2	Final CAD-model	41
6.3	Final mesh of CAD-model	41
6.4	Pressure outtakes on the main pipe.	42
6.5	Mesh, outlets and inlets in CFX-Pre	44
7.1	Calibration curve and 95% confidence interval scaled by 100 for the differential pressure transmitter	47
7.2	Calibration curve and 95% confidence interval scaled by 1000 for the volume flow meter	49
7.3	Calibration curve and 95% confidence interval scaled by 100 for the torque transducer	50
8.1	Hill diagram for 1 nozzle plotted against Q_{11}	58
8.2	Hill diagram for 2 nozzles plotted against Q_{11}	58

8.3	Complete Hill diagram plotted against Q_{11} with $n_{11} = 40.5$ and $n_{11} = 41.5$ indicated and the efficiency lines for different number of nozzles and the fitted line with $n_{11} = 40.5$ plotted against Q_{11}	60
8.4	Complete hill diagram plotted against Q_{11z} with $n_{11} = 40.5$ and $n_{11} = 41.5$ indicated in the upper part of the figure. The lower part of the figure shows the efficiency lines for different number of nozzles with constant $n_{11} = 40.5$ plotted against Q_{11z}	62
8.5	The head loss through the distributor for the original and different optimization strategies.	65
8.6	Velocity contours on the original (a) and throat optimized (b) distributor.	66
8.7	Vector plot of the velocity in the outlet to nozzle 1 in the original (a) and throat optimized (b) distributor.	68
8.8	Total pressure contours and velocity vectors at to outlet to nozzle 1 on the original (a) and throat optimized (b) distributor.	69
8.9	Total pressure contours on the original (a) and throat optimized (b) distributor.	70
9.1	Hill diagram with the transition between the number of nozzles open indicated	74
9.2	The relative velocity of the water as the bucket first enters the jet at a two pitch angles where the lower is the largest. The nozzle in this figure is copied from Figur 1.8 in [1].	76
9.3	Effect of change in pitch angle on the angle of attack for the jet on the bucket, β . This figure is made from parts of Figure 4.5, 7.1 and 14.6 in [10]	77
9.4	A bucket located in the jet seen from behind with the outflow at two different pitch angles	78
9.5	Entrance to nozzle 1 outlet on the original (a) and throat optimized (b) distributor	80

A.1	The HBM T10F Torque Flange (a) and a picture of how it was mounted on the test rig (b)	86
A.2	Principal of optical rotational speed measuring	87
A.3	Krohne Aquaflex F Electromagnetic Flow Meter	89
A.4	Krohne IFW 300 W Signal Converter	89
B.1	Torque Calibration Setup	93
C.1	The throat optimized distributor	102
C.2	The throat optimized distributor with primitive guide vanes	103
C.3	The throat optimized distributor with the throat mimicking that at nozzle 1 (a) and nozzle 4 (b)	104
D.1	Effect of hysteresis on instrument reading [14, Figure 2.5]	108
D.2	Example of nonlinearity and zero offset[14, Figure 2.6]	109
D.3	A Student-t distribution with different number of measurement points (a) and a Normal distribution with confidence interval (b)	110
E.1	Nozzle 3 (a) and nozzle 5 (b) after the failure	121
E.2	The front of the nozzle housing before (a) and after (b) the improvements	122
E.3	The ring before and after the improvements	122
E.4	The 4 buckets that were broken off the turbine by the rings	123
E.5	The turbine in place in the turbine housing after the failure	123
E.6	The turbine after it was taken out	124
F.1	Full Hill diagram with measurement points indicated	125
F.2	Hill diagram for 3 nozzle	126
F.3	Hill diagram for 4 nozzles	126
F.4	Hill diagram for 5 nozzles	127
F.5	Total pressure (a) and velocity (b) contours on the throat optimized distributor with primitive guide vanes	129

F.6	Total pressure (a) and velocity (b) contours on the throat optimized distributor with the throat mimicking that at nozzle 1.	130
F.7	Total pressure (a) and velocity (b) contours on the throat optimized distributor with the throat mimicking that at nozzle 4.	131

List of Tables

3.1	Loss in efficient head, H_e , through the turbine with reference pressure upstream of the volume flow meter as seen in Figure 4.3	17
4.1	Test Matrix	31
5.1	Change in area after throat optimization	35
6.1	Boundary conditions used during the simulation	42
7.1	Component errors in the calibration of an instrument	46
7.2	Errors in the uncertainty in the calibration of the volume flow meter	48
7.3	Errors in the uncertainty in the calibration of the torque transducer	49
7.4	Component errors in the test	51
7.5	Errors in the uncertainty in the volume flow measurements .	52
7.6	Errors in the uncertainty in the torque measurements	53
7.7	Errors in the uncertainty in the temperature measurements	54
B.1	Calibration of weight used in Torque cell calibration	92

Nomenclature

arm	Torque arm	m
dA_i	Area difference, throat, at the outlet to nozzle i	m^2
B	Bucket width	m
c	Absolute water velocity	m/s
dc	Velocity difference	m/s
D	Diameter	m
E	Specific Hydraulic Energy	J/kg
e_X	Total absolute error in quantity X	
F	Force	N
f	Friction factor	
$f_{X_{cal}}$	Total relative uncertainty of calibration of the instrument measuring the quantity X	
f_X	Total relative error in quantity X	
g	Acceleration of gravity	m/s^2

Δh	Height difference	m
H_e	Effective head	m
H_{dyn}	Dynamic head	m
H_{stat}	Static head	m
ΔH_f	Friction head loss	m
ΔH_K	Head loss due to geometry	m
K	Loss coefficient	
L	Characteristic length	
m	Mass	kg
N	Number of measurements	
n	Rotational speed	rpm
n_{11}	Modified speed factor	$rpm\sqrt{m}$
n_{ED}	Speed factor	
P	Power	W
P_m	Mechanical power	W
P_h	Hydraulic power	W
P_{Lm}	Power dissipated in bearings and shaft seals	W
p_{amb}	Atmospheric pressure	Pa
p_M	Measured static pressure	Pa
Δp	Differential pressure	Pa
Q	Volumetric flow	m^3/s

NOMENCLATURE

xxiii

Q_{11}	Modified discharge factor	$l/sm^{5/2}$
Q_{11z}	Modified nozzle discharge factor	$1/s\sqrt{m}$
Q_{ED}	Discharge factor	
dQ	Discharge through nozzle	m^3
Re	Reynolds number	
S_X	Standard deviation of the output of the measurements	
S_{XX}	Experimental error variation of input around the linear approximation	
S_{XY}	Experimental error co-variation of output and input around the linear approximation	
S_{YY}	Experimental error variation of output around the linear approximation	
T	Temperature	$^{\circ}\text{C}$
$t_{\alpha/2}$	Student t-value for confidence level $1 - \alpha$	
u	Peripheral velocity	m/s
\bar{X}	Arithmetic mean of measurements	
x_i	Length of throat at the outlet to nozzle i	m^2
Z	Number of nozzles	
Greek Letters		
α	Confidence level, $1 - \alpha$	
β	Jet angle of attack on the bucket	$^{\circ}$
ϵ	Wall roughness	mm

η_h	Hydraulic efficiency	
$\mu_{Y x_0}$	Mean response of Y with the input x_0	
ν	Kinematic Viscosity	m^2/s
ω	Rotational speed	$1/s$
ϕ	Nozzle loss coefficient	
$\bar{\rho}$	Mean water density	kg/m^3
ρ	Water density	kg/m^3
τ	Torque	Nm

Abbreviation

CFD Computational Fluid Dynamics

NTNU Norwegian University of Science and Technology

SST Shear Stress Transport

Chapter 1

Introduction

Norway is blessed with a topology suited for production of electricity by hydro power. While hydro power is considered a clean energy source, it is always of the highest interest to achieve the best possible efficiency. As the focus on climate change has increased and its effects on the planet has become more visible, a high efficiency has become even more sought after.

The Pelton turbine is an impulse turbine and is one of the turbines used in Norwegian hydro power. It is used for high heads and relatively low volume flows which and operates in atmospheric pressure. The turbine type is different from reaction turbines, e.g. Francis and Kaplan turbines, because all the energy extracted from the water is in the form of velocity energy. The water is introduced on the turbine by a jet emitted from one or more nozzles where the pressure energy in the flow is transformed to velocity. The turbines optimal rotational speed is dependent on the velocity out of the jet which is dependent on efficient head. If multiple nozzles are used and the losses through the distributor are significant the different nozzles will operate at a different effective head and hence the rotational speed will only be optimal for some.

Hydroenergi is one of the producers of hydro power turbines in Norway.

They have a great amount of knowledge within Kaplan and Francis turbines and are currently looking to expand their knowledge within Pelton turbines. In their previous bucket designs they have struggled with cavitation problems and they have therefor produced multiple design with the aim to reduce these problems. The existence of cavitation may cause fatigue on the bucket and thereby lower the efficiency of the turbine over time. They are interested in testing the efficiency of the new designs has not been decreased compared to the original. The head loss through their distributor design has previously been investigated and found to be significant. They therefor aim to improve the design by either optimizing the existing design or by redesigning the distributor completely.

Chapter 2

Theory

A Pelton turbine is an impulse turbine which is characterized by the fact that all the energy the runner extracts from the water is associated with velocity.

2.1 Optimization of Pelton Turbine Parameters

In order to maximize the power generated the optimal hydraulic operational point is investigated.

2.1.1 Optimal Rotational Speed

Equation (2.1), Euler's turbine equation [1] shows the ratio between the energy available in the flow and the energy transferred to the turbine. The subscripts denote the inlet, 1, outlet, 2, of the turbine and the peripheral velocity component, u .

$$\eta_h = \frac{c_{u1}u_1 - c_{u2}u_2}{gH_e} \quad (2.1)$$

From Equation (2.1) it is possible to find the optimal rotational speed of a Pelton turbine. With the assumption that the absolute velocity of the water exiting the turbine is zero at the best point of operation, $c_{u2} = 0$

all the energy in the water is transferred to the turbine. However, in real life this would leave the water still when exiting the bucket and leave it to hit the backside of the next bucket, back wash. This simplification is still assumed to be a good approximation to use when determining the optimal peripheral speed u . By this Equation (2.1) is reduced to:

$$\eta_h = \frac{c_{u1}u_1}{gH_e} \quad (2.2)$$

Figure 2.1 shows the velocity diagrams for the flow entering, index 1, and exiting, index 2, the runner of a Pelton turbine. c denotes the absolute velocity, w the velocity relative to the runner and u the peripheral velocity of the runner.

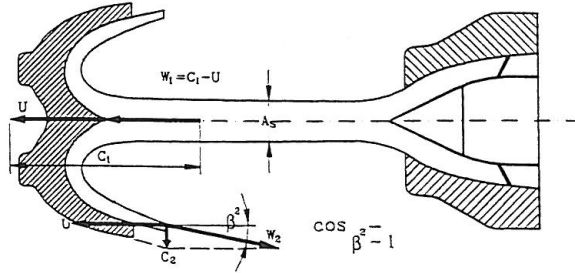


Figure 2.1: Velocity diagram for a Pelton turbine [1]

The figure shows that the flow exiting the nozzle only has a velocity component in the peripheral direction, $c_{u1} = c_1$. If the losses through the nozzle are denoted by the loss coefficient ϕ [9], the velocity out of the nozzle may be expressed as:

$$c_1 = \phi \sqrt{2gH_e} \quad (2.3)$$

By solving Equation (2.2) for u_1 with c_1 from Equation (2.3) one can obtain an expression for the optimal peripheral speed is obtained.

$$u_1 = \frac{\eta_h g H_e}{c_1} = \frac{\eta_h g H_e c_1}{\phi^2 2g H_e} = \frac{\eta_h c_1}{2\phi^2} \quad (2.4)$$

By assuming hydraulic efficiency, $\eta_h = 0.90$, and a loss coefficient through the nozzle $\phi = 0.97$ [9], the expression for the optimal peripheral velocity is reduced to:

$$u_1 = 0.4783 \cdot c_1 \quad (2.5)$$

With the rotational speed of the turbine defined as $\omega = 2u/D$, the expression for the optimal rotational speed is as shown in Equation (2.6)

$$\omega = 1.312 \frac{\sqrt{gH_e}}{D} \quad (2.6)$$

2.1.2 Optimal Bucket Dimensions

Pelton theory claims that the hydraulic efficiency will increase with a decreasing diameter to bucket width ratio, D/B . However, this value can not be reduce below a certain limit since significantly large buckets compared to the diameter will produce large areas where the water does not interact with any buckets. Brekke [2] finds, based on empirics, the optimal dimensions for the Pelton bucket by setting a minimum number of buckets and a minimum bucket width with regards to the jet diameter and the number of jets.

2.1.3 Optimal Pelton Distributor Design

The distributor for a Pelton turbine leads the water to nozzles where the pressure energy is transformed to velocity energy before it hits the runner. A traditional Pelton distributor with nozzles is shown in Figure 2.2. The shape and uniformity of the individual jets from the nozzles is strongly connected with the efficiency of the turbine. In addition, the jets from the nozzles should be identical so that the rotational speed is optimal with regard to the jet velocity as described in Chapter 2.1.1. The optimal distributor for a Pelton turbine should fulfill the following points:

- Minimal head loss through the distributor so that variations in the discharge velocity between the nozzles are minimized.
- The mean velocity over the pipe cross sections along the distributor should be near constant. This is important to minimize the variation in the losses that are dependent on the velocity. This will reduce the variation in effective head due to a difference in losses through the distributor.
- All sharp bends produce a swirling secondary flow after the bend [15] and therefore the bends in the distributor should be smooth. This is especially important for the bends directly upstream of the outlets to the nozzles. This is due to the fact that the presence of a swirl at the inlet to the nozzle may worsen the condition of the jet [16].

In the project work leading up to this thesis the head loss through the distributor was measured and the results are presented in Chapter 3.2.

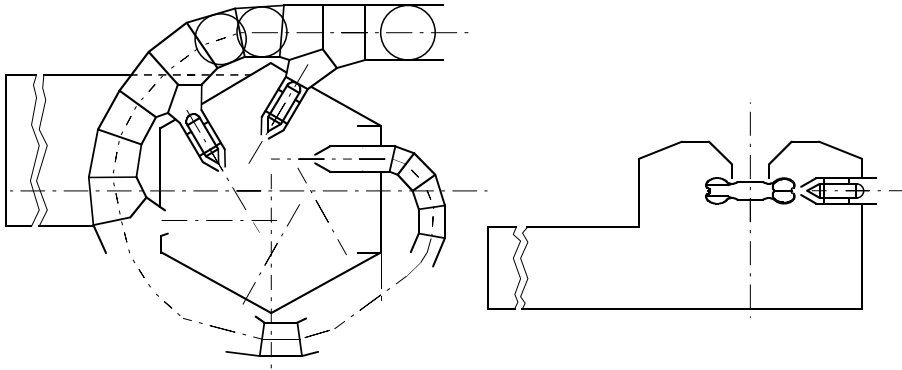


Figure 2.2: Traditional Pelton distributor made up of short pipe sections fabricated from steel plates [4]

2.2 Model Testing

During the design process of a new turbine model tests are often conducted before a prototype is produced. This is because the production costs for a model are lower due to the smaller size. A model test is therefore a good tool in predicting the operation of the actual turbine. According to IEC 60193 [4] the following conditions must be fulfilled for a model test to be viable.

The geometric similarity is related to the actual shape of the turbine, this is done by making the model as an exact replica of the prototype but smaller in all dimensions [4].

The hydraulic similarity reflects the ratio of forces affecting the model compared to the prototype [4]. On Pelton turbines the hydraulic similarity is defined as when the reduced quantities; discharge factor, Q_{ED} , and speed factor, n_{ED} , are the same for both prototype and model. In Norway it is common practice to use Q_{11} and n_{11} instead of Q_{ED} and n_{ED} and therefore these reduced quantities have been used throughout this report. The reduced quantities are defined in Equation (2.7) and (2.8).

$$(n_{11})_{\text{Prototype}} = (n_{11})_{\text{Model}} = \left(\frac{nD}{\sqrt{H_e}} \right)_{\text{Model}} \quad (2.7)$$

$$(Q_{11})_{\text{Prototype}} = (Q_{11})_{\text{Model}} = \left(\frac{Q}{D^2 \sqrt{H_e}} \right)_{\text{Model}} \quad (2.8)$$

While Q_{ED} and n_{ED} are dimensionless quantities, n_{11} and Q_{11} are not. In this report n_{11} has been calculated with n in *rpm*, so the dimensions of n_{11} results in *rpm* \sqrt{m} . Q_{11} has been calculated with Q in *l/s* with the dimension resulting in *l/sm*^{5/2}. Hydroenergi uses a different definition of Q_{11} where the volume flow is measured in *m*³/*s* and divided by the number of nozzles, Z , as shown below.

$$(Q_{11Z})_{\text{Prototype}} = (Q_{11Z})_{\text{Model}} = \left(\frac{Q/Z}{D^2 \sqrt{H_e}} \right)_{\text{Model}} \quad (2.9)$$

By using nozzle discharge factor, Q_{11Z} , rather than Q_{11} or Q_{ED} , it is easier to compare the efficiency of a specific bucket geometry. It eliminates the effect of the number of nozzles on the distributor the turbine has been tested with.

2.3 Hydraulic Efficiency

The hydraulic efficiency η , is defined by the IEC Standard [4] as:

$$\eta_h = \frac{P_m}{P_h} = \frac{P + P_{Lm}}{E \cdot Q \rho} = \frac{P + P_{Lm}}{\rho g Q H_e} \quad (2.10)$$

P is defined as the power delivered by the turbine shaft, which is equal to product of the torque and rotational speed, $P = T \cdot \omega$. P_{Lm} is the power dissipated in the bearings and shaft seals, Q is the volumetric flow. $\bar{\rho}$ is the mean density of the water between the high and low pressure side of the machine. E , the specific hydraulic energy, and H_e , the effective head, is defined in Equation (2.11) and Equation (2.12). The specific hydraulic energy is the energy available in the water between the high and low pressure sides of the machine shown in Figure 2.3.

$$E = \frac{p_{M_1} - p_{amb}}{\bar{\rho}} + g\Delta h + \frac{c_1^2}{2} = \frac{\Delta p}{\bar{\rho}} + g\Delta h + \frac{c_1^2}{2} \quad (2.11)$$

p_{M_1} is the absolute pressure at the turbine inlet and p_{amb} is the atmospheric pressure. Δh is the height difference between the pressure transducer and the center of the turbine inlet. During the experiments conducted in this thesis the pressure was measured as differential pressure at the turbine inlet, $\Delta p = p_{M_1} - p_{amb}$.

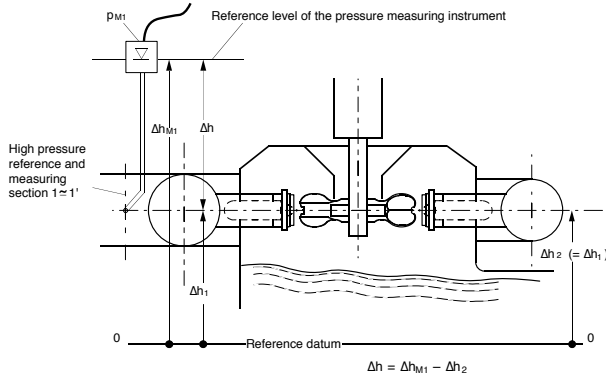


Figure 2.3: Schematic figure of a Pelton machine [4]

The effective head is the total pressure measured in *meter water column* and is defined as shown below. It consists of the static head, H_{stat} , and the dynamic head, H_{dyn} , which is the static and dynamic pressure measured in meter water column.

$$H_e = \underbrace{\frac{\Delta p}{\rho g} + Z}_{\text{Static head } (H_{stat})} + \underbrace{\frac{v^2}{2g}}_{\text{Dynamic head } (H_{dyn})} \quad (2.12)$$

2.4 Distributor Optimization

The water flowing through the distributor interacts with the pipe wall in addition to bends, changes in area and inlets to the nozzles. All these interactions lead to loss of hydraulic energy. If the head-loss through the distributor of a Pelton turbine is significant, it will lead to a change in velocity out of the nozzles, c , due to the variation of H_e in Equation (2.3).

Equation (2.6) shows that the optimal rotational speed, ω , is dependent on the velocity out of the nozzles. When the nozzle outlet velocity vary

between nozzles the rotational speed of the turbine will only be optimal for some of the nozzles. This will reduce the local efficiency for the nozzles with a lower velocity. In addition, the distribution of H_e over the cross section at the inlet of each individual nozzle should be uniform. This is due to the fact that a non uniformity will result in the jet being non uniform in both velocity and geometry. This will affect the turbine efficiency by varying the velocity out of the nozzle.

Friction also contributes to the head loss as the water loses energy due to the friction on the wall. The friction head is a function of the friction factor, f , which is found in the Moody char. The input of the Moody chart is the Reynolds number, Re , and the wall roughness diameter ratio, $\frac{\epsilon}{d}$. The Reynolds number and the equation for the friction head loss is shown below.

$$Re = \frac{cD}{\nu} \quad (2.13)$$

$$\Delta H_f = f \frac{L}{D} \frac{c^2}{2g} \quad (2.14)$$

In the literature standardized coefficients for losses in pipe flow through different geometries are defined. These loss coefficients, K , are used to calculate a corresponding head loss, ΔH_K . Equation (2.15) shows head loss expressed with the standardized loss coefficient [15]. The loss coefficients for the bends and throats in the distributor vary around $0,185 \leq K \leq 0,195$.

$$\Delta H_K = \frac{V^2}{2g} K \quad (2.15)$$

The nozzle exit velocity is controlled by the pressure differential, area reduction in the distributor and friction losses. If the discharge through a nozzle is smaller than that due to the area reduction, throat, at the inlet to the nozzle in the main pipe the water in the distributor will accelerate. This is to compensate for the increase in volume flow as shown in Equation (2.16) where dQ is the discharge through the nozzle and dA is the throat over the nozzle inlet.

$$c + dc = \frac{Q + dQ}{A + dA} \quad (2.16)$$

Chapter 3

Background

3.1 Summary of Previous Efficiency Experiments

The turbine investigated in this thesis has been tested on two previous occasions, in 2005 and 2008. The design best point of operation is located at $n_{11} = 41.5$.

3.1.1 Efficiency Test with 5 Nozzles

In 2005 the turbine underwent an efficiency test with 5 nozzles at different openings and with different nozzle combinations. The test was conducted at a static head of $H_{\text{stat}} = 50$ m. The modified speed factor, n_{11} , was constant at the calculated point of best efficiency and the modified discharge factor, Q_{11} , was varied. At the highest nozzle openings with 4 nozzles and all openings with 5 nozzles the static head was reduced to $H_{\text{stat}} = 40$ m. This was done because the torque was too large for the generator. With all nozzles fully opened the static head was reduced to $H_{\text{stat}} = 30$ m for the same reason. The efficiency was found to be the same at both 80% and 100% opening of 5 nozzles. In addition to the efficiency test the effect of the following points on the hydraulic efficiency were investigated,

- Number of stay bars connected to the needle in the nozzle.

- The effect on water flow within the turbine housing caused by deflectors in their disengaged position.
- Air inlet through valves mounted underneath each nozzle.

The results from the efficiency test, without deflectors and air intake, at n_{11} constant at the point of best operation are shown in Figure 3.1. The effect of the deflector and the air inlet was found to be negligible. The investigation of the effect of the number of stay bars was inconclusive. This was due to the fact that the nozzles that differed in the number of stay bars were at different positions in the distributor and hence the effect could not be compared.

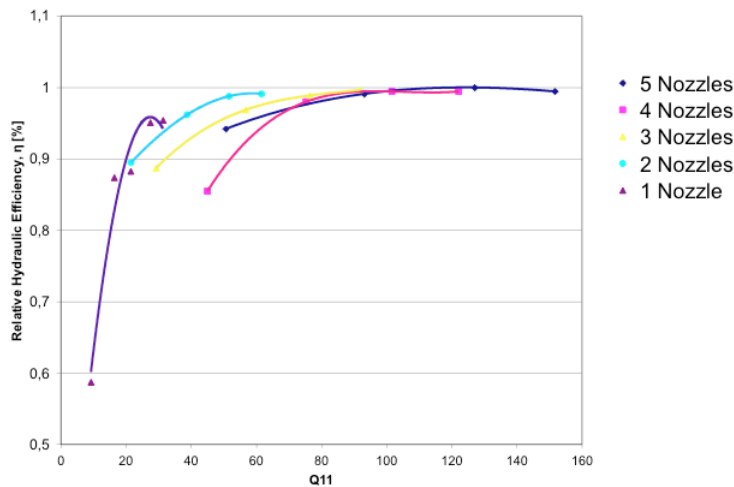


Figure 3.1: Hydraulic Efficiency at near constant $n_{11} = 41.5$

3.1.2 Efficiency Test of Different Bucket Sizes with 1 Nozzle

The second test was conducted after Hydroenergi had some changes done to the design of their Pelton turbine with the aim to reduce cavitation. The objective of the test was to investigate if the new design had any effect on

the hydraulic efficiency of the turbine. In addition the test also investigated the difference in hydraulic efficiency between buckets of the same design but with different diameter to bucket width ratio, D/B . Pelton turbine theory claims that the hydraulic efficiency will increase with decreasing diameter to bucket width ratio, and the test found this to be true for the turbine. The Hill diagram for the different bucket sizes is shown in Figure 3.3. More information on the procedure and results of these experiments may be found in [11]. This test concluded that the hydraulic efficiency of the turbine with the modified buckets were lower than state of the art Pelton turbines. The tests were conducted at a $H_{\text{stat}} = 30$ and 50 m and the relation between the hydraulic efficiency and the effective head was conducted and the results are shown in Figure 3.2.

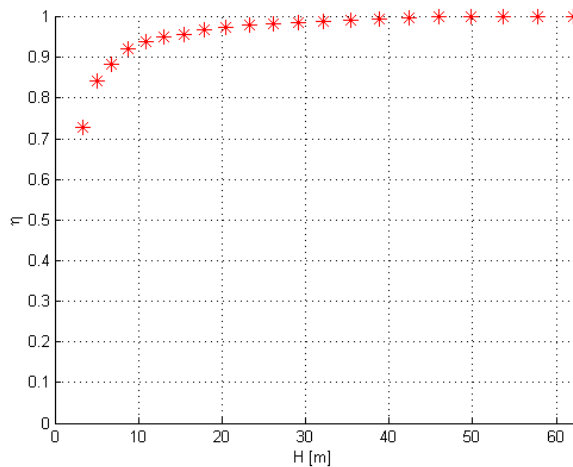


Figure 3.2: Relation between hydraulic efficiency and efficient head [11]

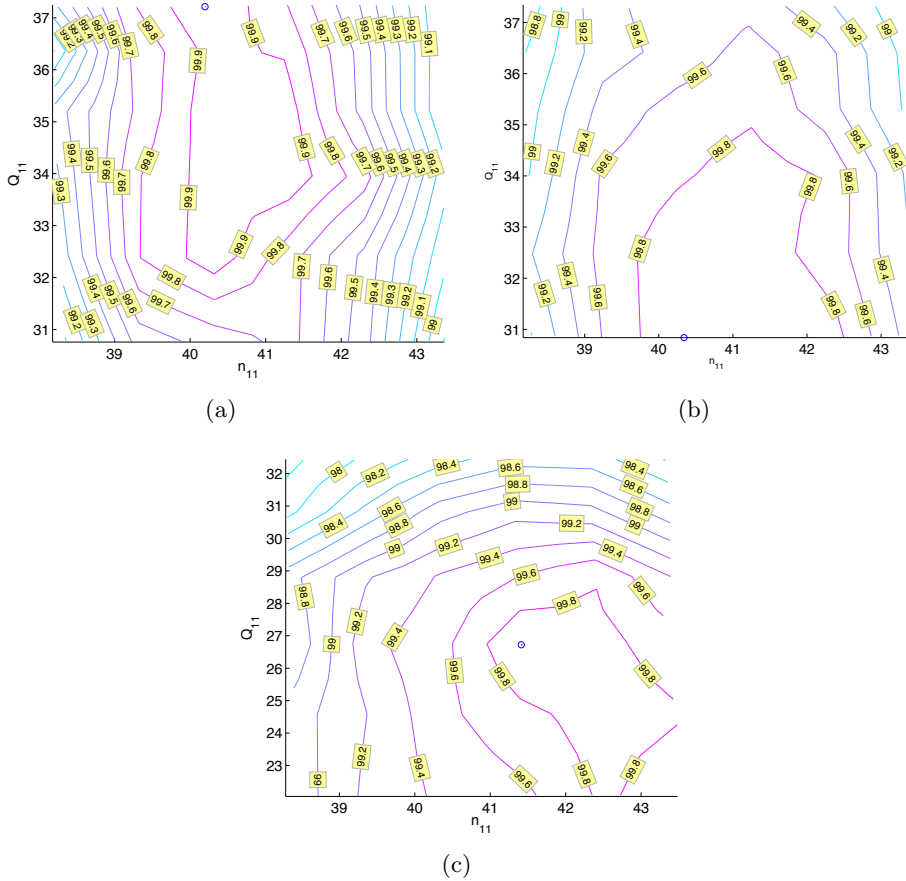


Figure 3.3: Hydraulic Efficiency for the large (a), medium (b) and small (c) bucket [11]

3.2 Summary of Previous Head Loss Experiments

Experiments investigating the head loss in the distributor were conducted in the project[12]. The loss in efficient head, H_e , is listed in the table below

with the corresponding absolute uncertainty in brackets. The reference for the loss is a position approximately 3 m upstream of the turbine. This is also upstream of the volume flow meter and the throat and nozzle connected to it. More information on the procedure used and the results may be found in [12].

Position	Nozzle opening			
	40%	60%	80%	100%
Pre Nozzle 1	-0,048 (±0,060)	-0,080 (±0,059)	-0,143 (±0,060)	-0,195 (±0,060)
Pre Nozzle 2	-0,062 (±0,061)	-0,097 (±0,060)	-0,152 (±0,061)	-0,201 (±0,061)
Pre Nozzle 3	-0,068 (±0,064)	-0,116 (±0,063)	-0,192 (±0,064)	-0,203 (±0,064)
Pre Nozzle 4	-0,085 (±0,072)	-0,153 (±0,071)	-0,225 (±0,072)	-0,290 (±0,072)
Pre Nozzle 5	-0,074 (±0,083)	-0,133 (±0,082)	-0,209 (±0,083)	-0,281 (±0,083)

Table 3.1: Loss in efficient head, H_e , through the turbine with reference pressure upstream of the volume flow meter as seen in Figure 4.3

The distributor is made up of standard pipe sections and contractions to keep the total cost of production down. This has resulted in the throat over the outlets to the nozzles not corresponding with the volume flow out of the nozzle. This gives non optimal flow conditions by acceleration and deceleration of the flow through the distributor or by a difference in discharge between the nozzles. The distributor also includes sharp bends in the main pipe that also leads to losses. Figure 3.4 shows the distributor with the main pipe and outlets indicated.

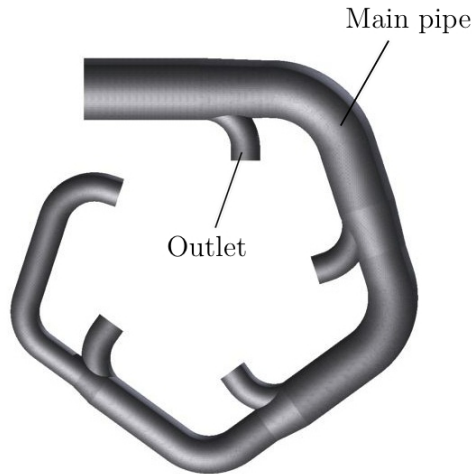


Figure 3.4: The distributor with the main pipe and the outlet to nozzle 1 indicated

3.3 Summary of Previous Simulations

In the project[12] a number of simulations were conducted on the distributor using Computational Fluid Dynamics (CFD) that were verified with the experiments conducted. Figure 3.5 shows the head loss through the distributor found during the experiments and from the simulations. In the figure it is shown that the head loss from the simulations are well within the uncertainty of that measured, and they have approximately the same shape. The deviation in shape is greatest at the position in Pre Nozzle 4 which may be explained by the assumptions used to calculate the effective head from the measured data. In the project the mass flow through each nozzle was assumed to be equal but due to a variation on throat over each nozzle outlet this assumption must be not valid. Even with this faulty assumption the result may be assumed valid due to the fact that the velocity contributes little to the effective head compared with the static pressure. The inequality between equal discharge and the discharge due to the throat at the nozzle

outlets is shown in Figure 3.6. Figure 3.7 shows the absolute velocity through the distributor at 80% nozzle opening.

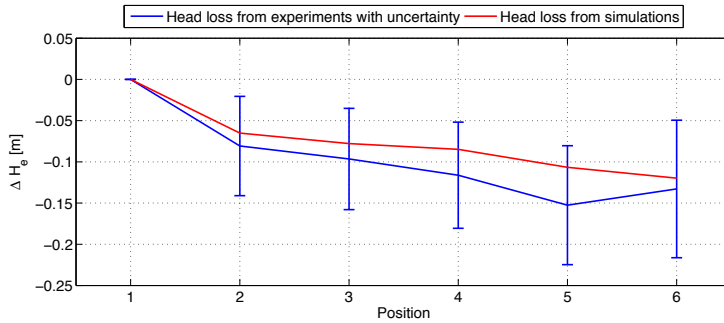


Figure 3.5: Head loss from previous experiments with uncertainty and head loss from simulations at 60% nozzle opening. Corrected version of [12] where the uncertainty shown is relative but should be absolute.

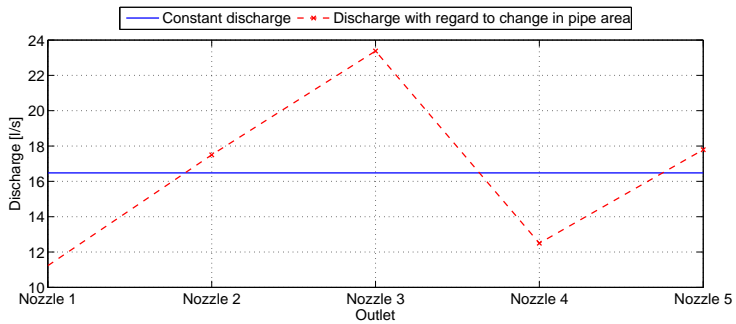


Figure 3.6: Discharge due to throat over nozzle outlet and equal discharge at 60% nozzle opening, [12]

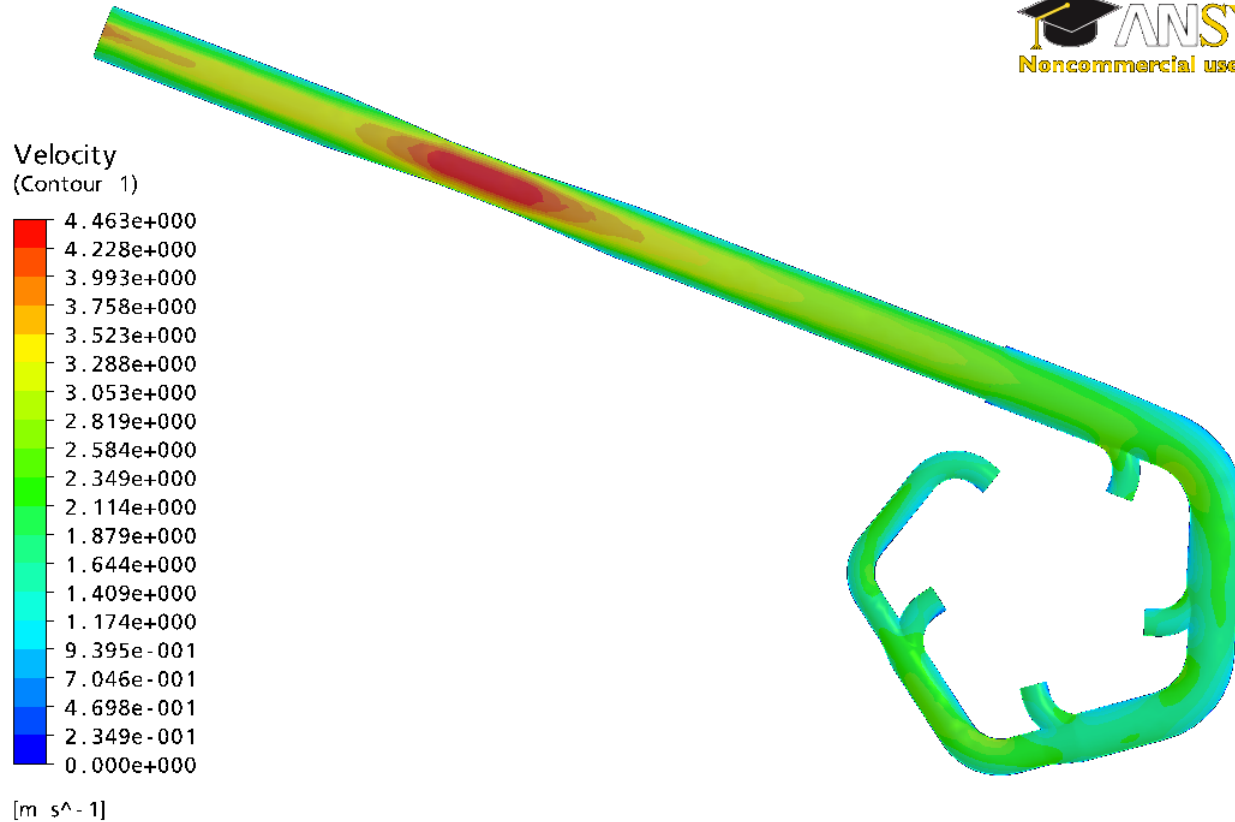


Figure 3.7: Absolute Velocity through the Distributor

Chapter 4

Experimental Setup and Methode

The hydro power laboratory at NTNU has a large system of pipes installed for use during different experiments that require different flow conditions and properties. Figure 4.1 shows the experimental setup in the laboratory. The laboratory is equipped with a water reservoir that holds 450 m^3 of water. Two pumps, where the one used in these experiments have a maximum head of $H_{max} = 100 \text{ mWc}$, and a pressure tank that has a maximum internal pressure $P_{max} = 10 \text{ bar}$.

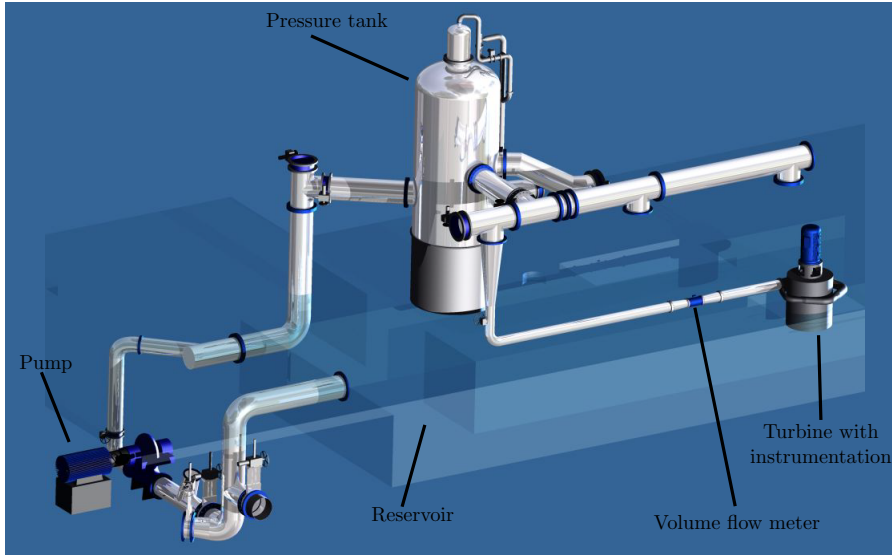


Figure 4.1: Experimental Setup

4.1 Instrumentation

The turbine that has been tested in this thesis was connected to a 55 kW asynchronous generator. The test rig included a differential pressure transmitter, a volume flow meter, a torque flange, a thermometer and a rotational speed indicator. All the instruments were connected through a National Instruments logging card to a computer with a specialized LabView logging program. This LabView program is found on the CD included with this thesis and is named *Loggingprogram.vi*. The outputs of the instruments included both current, voltage and frequency signals. The frequency and current signals were converted to voltage signals to ease the data logging. Figure 4.2 shows a schematic overview of how the instruments signals were converted and connected to the computer. Figure 4.3 shows the placement of the instruments on the test rig.

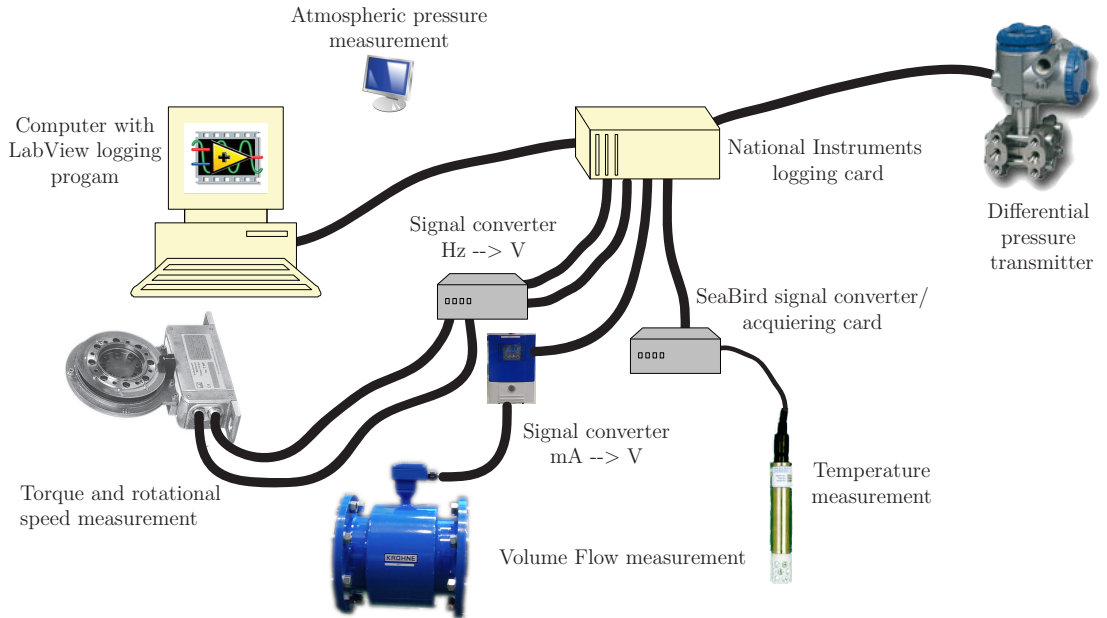


Figure 4.2: Schematic overview of the instrument setup

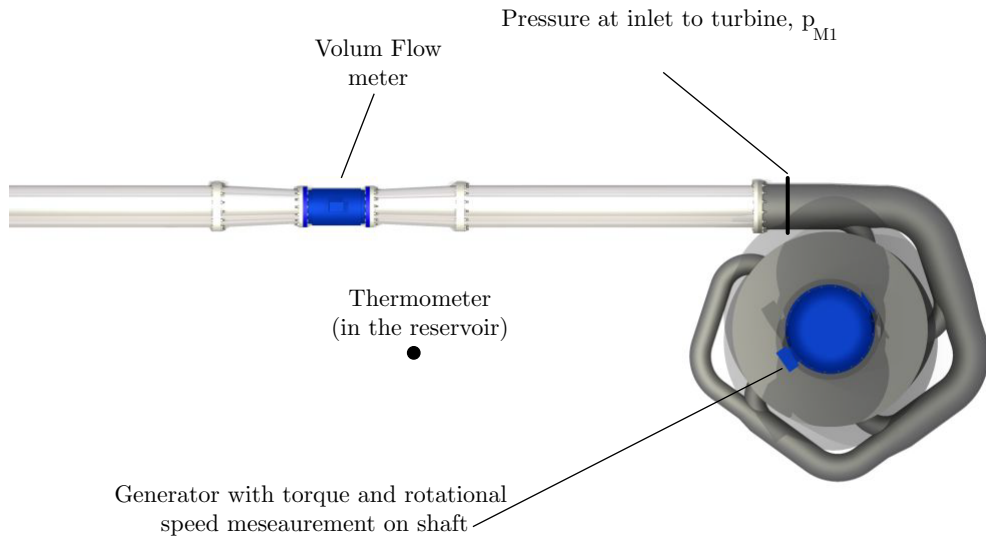


Figure 4.3: Instrument location on test rig

4.1.1 Volume Flow Measurement

The volume flow measurements were conducted with an electromagnetic flow meter, Aquaflux F manufactured by Krohne. The flow meter was connected to the logging rack via a Krohne IFW 300 W Signal converter that converted the signals from 4 – 20 mA to 2 – 10 V. The signal converter also functioned as a controller and indicator for the flow meter. During the experiments the range was set to 0 – 150 l/s. This type of volume flow meter is very sensitive to gas in the flow and extra effort was put into venting the pipe system thoroughly before tests were conducted.

4.1.2 Torque and Rotational Speed Measurement

The torque from the turbine was measured with a rotating torque flange mounted on the shaft between the turbine and the generator. The torque flange used was a T10F manufactures by HBM. Included in the torque flange was an optical rotational speed measuring system. More information about the torque flange and its rotational speed measuring system may be found in Appendix A.1 and A.2.

4.1.3 Pressure Measurement

Differential Pressure Measurement

The static pressure p_{M1} of the water flowing in to the distributor was measured using Fuji Electric FKKW37V1 differential pressure transmitter. The transmitter had a range from 0 – 10 bar and is shown in Figure 4.4(a). The range was changed to 0 – 7 bar with a Fuji Electric Hand Held Communicator before the calibration. The transmitter was connected to a ring manifold consisting of four inter connected pressure outtakes around the pipe as shown in Figure 4.4(b). The pressure outtakes and the pressure transmitter were all connected via 8 mm plastic pipe. During the experiments the plastic pipes were filled with water by venting out the air in the tubes. This was done by opening the valve on the other side of the pressure transmitter so that the air was vented out. The height difference

between the pressure transmitter and the pipe center, $\Delta h_{\text{test}} = 0.241$ m, was taken into account by adding the pressure difference $\Delta p = \rho g \Delta h_{\text{test}}$ to the measured differential pressure. The height difference, Δh_{test} , was measured with a ruler and Leica Rugby 200 rotating laser Level.

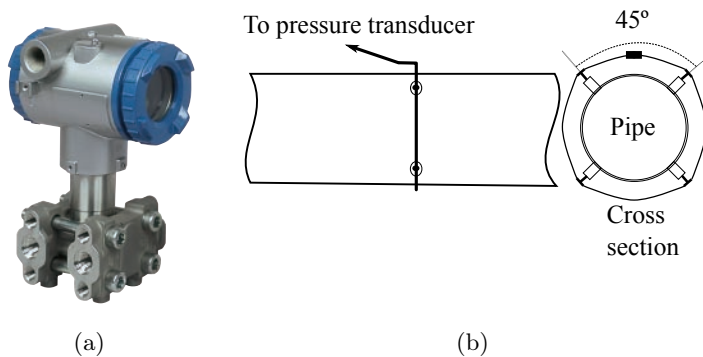


Figure 4.4: Fuji FKKW37V differential pressure transducer (a) and the ring manifold pressure outtake (b)

Atmospheric Pressure Measurement

The atmospheric pressure was measured with a digital pressure transducer located in the lab. The atmospheric pressure was displayed on a monitor visible from the logging rack and it was manually fed into the logging program.

4.1.4 Temperature Measurement

The thermometer that was used to measure the water temperature was located in the reservoir underneath the turbine and therefore measures the temperature of the water downstream of the turbine. The thermometer was a SBE 38 Digital Oceanographic Thermometer manufactured by Sea-Bird.

4.2 Calibration

4.2.1 Volume Flow Meter

The volume flow meters digital display was assumed to be correct in the previous experiments. As the volume flow is a critical property in the calculation of the efficiency of the turbine it was fully calibrated by the weighing method. This is recommended as a primary calibration method in IEC [4]. ISO 4185 [5] states all the requirements concerning the measuring apparatus, procedure, calculation methods and the associated uncertainties.

The weights in the weighing tank system at the Water Power Laboratory had to be calibrated before the calibration of the volume flow meter. More information on the calibration setup, the procedure for calibrating the weight cells and the resulting correction equation is shown in Appendix B.2.

The calibration curve with data points is shown in Figure 4.5.

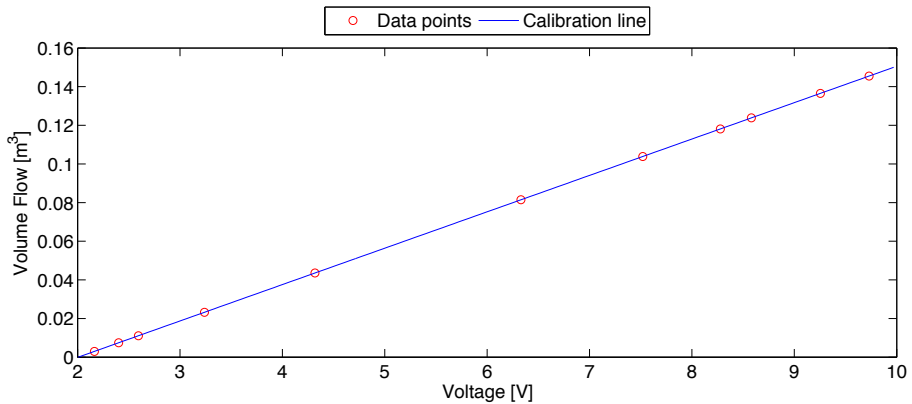


Figure 4.5: Calibration curve for volume flow meter

4.2.2 Torque Transducer

The torque transducer was calibrated by applying torque to the turbine side of the transducer. This was done by connecting a horizontal metal bar to the shaft connecting the turbine to the transducer. A metal bar with a pulley on the end was therefor welded to the turbine casing so that hanging weight could be utilized to apply a torque to the shaft. The weight rested in a bed and were connected to the shaft via a wire over the pulley as shown in Figure 4.6. A metal plate was connected to the generator shaft and held it in place by interacted with the shaft casing. The weights used were calibrated by Justervesenet and their deviation from their claimed weight is shown in B.1 and their calibration certificate is shown in Appendix H.3. The weight of the weight bed and vertical section of the wire was measured with a Kern FTB 15K0.5 scale in the lab.

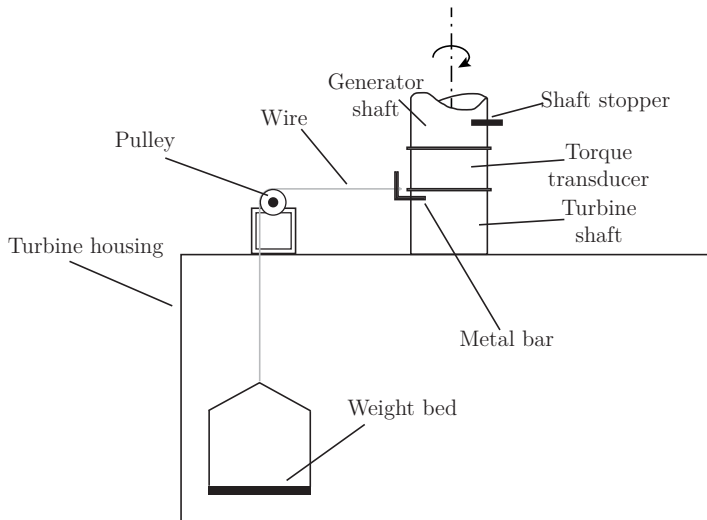


Figure 4.6: Setup for torque transducer calibration

Equation (4.1) was used to calculate the torque induced on the shaft by the

weights. The *arm* is the length from the shaft center to the wire connected to the metal bar. The force, $F = mg$, is the gravitational force on the weights, weight bed and the vertical section of the wire.

$$\tau = F \cdot arm = m \cdot g \cdot arm \quad (4.1)$$

The length of the arm was measured with a ruler from the center of the wire to the edge of the shaft. The radius of the shaft was added to this length and was found by use of a slide gauge. Figure 4.7 shows the calibration curve found for the torque transducer.

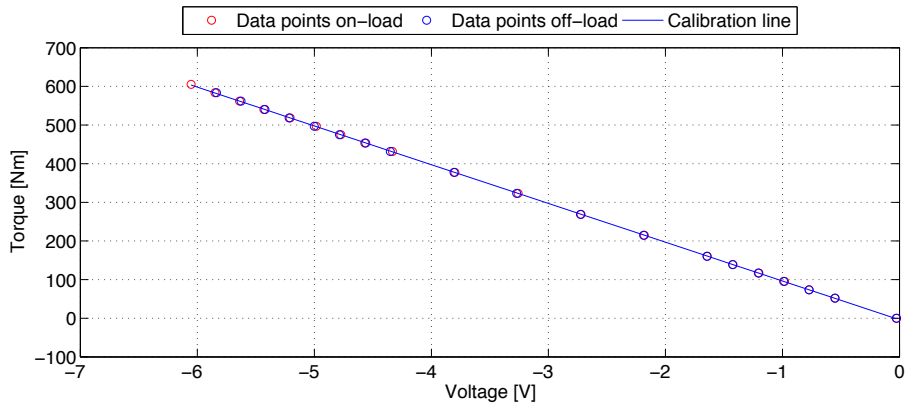


Figure 4.7: Calibration curve for torque transducer

The torque transducer was calibrated during both on- and off-load due to the fact that hysteresis is a common error found in torque and strain transducers. The error due to hysteresis is therefor assumed negligible.

4.2.3 Differential Pressure Transmitter

The differential pressure transmitter was calibrated with a GE Druck P3223-1 dead weight manometer. IEC 60913 [4] defines the dead weight manometer method as a primary calibration method for pressure measurements. The

transmitter was mounted on the wall near the test rig and the manometer was placed on a level table beside the transmitter. A plastic pipe connected the manometer to the pressure transmitter and this was filled with water, as this is the working fluid of the manometer. The pressure transmitter was located $\Delta h_{cal} = 0.02724$ m below the zero point of the manometer. The height difference was found with a ruler and a Leica Rugby 200 rotating laser level. Equation (4.2) was used to calculate the total pressure on the transmitter.

$$P_{total} = P_{manometer} + \rho g \Delta h_{cal} \quad (4.2)$$

The calibration curve for the transmitter is shown in Figure 4.2.3

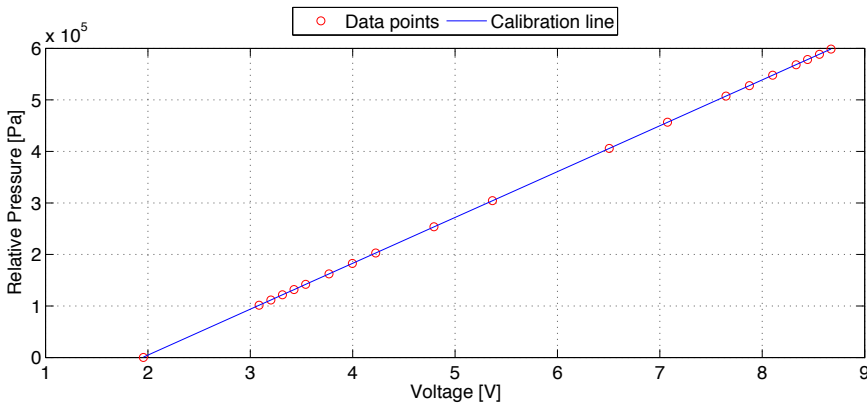


Figure 4.8: Calibration curve for the differential pressure transmitter

4.3 Problems Encountered dring the Experiments

As with most experiments the ones conducted in this thesis included problems of different extent. During the instrumentation of the test rig all the instruments failed to give a signal on the first test, but these problems were caused by faulty wiring and/or human error. During the experiments two failures led to long down times. First a failure in the frequency converter

for the generator occurred. After some time two of the nozzle houses failed and sent two bronze discs flying through the buckets. This resulted in 14 broken buckets and also required a full improvement of all five nozzle houses.

Replacements for the damaged buckets were ordered by Hydroenergi, but at delivery it was made clear that they were produced for a smaller model. This rendered them useless with the distributor and boss used in the tests. After a discussion with Hydroenergi it was decided that the experiments would continue with buckets of the same geometry but with a 2° greater pitch angle. The effect of this increase in pitch angle is discussed in Chapter 9.1.

The two failures and their solutions are described in Appendix E.

4.4 Designing the Test Matrix

One of the main results of this thesis was a complete Hill diagram for one of the bucket designs. This includes a variation in volume flow (Q_{11}/Q_{11z}) and rotational speed (n_{11}) within the operational area of the turbine. The variation in volume flow was achieved by changing the nozzle opening from 20% to 100% with steps of 20%. This was first done for 1 nozzle, then 2 nozzles in parallel and so on until all the nozzles were 100% open. The variation in rotational speed was achieved by changing the rotational speed of the turbine while it ran at a constant volume flow. Table 4.1 shows the test matrix used during the experiments.

As seen in the test matrix the span of the n_{11} variation was changed after the first three runs with only nozzle 1 open. This was done after a meeting with Hydroenergi where they expressed a wish for a wider span. The results from the tests done with a narrower span were used since the wide span in rotational speed is more important at higher volume flows.

4.5. ADJUSTMENT OF STATIC HEAD DURING THE EXPERIMENTS 31

Nozzle opening		n_{11}				
Nozzle 1	20%	38.5,	39,	...	,43.5,	44
	40%	38.5,	39,	...	,43.5,	44
	60%	38.5,	39,	...	,43.5,	44
	80%	37,	37.5,	...	,44.5,	45
	100%	37,	37.5,	...	,44.5,	45
Nozzle 1 & 2	20%	37,	37.5,	...	,44.5,	45
	40%	37,	37.5,	...	,44.5,	45
	60%	37,	37.5,	...	,44.5,	45
	80%	37,	37.5,	...	,44.5,	45
	100%	37,	37.5,	...	,44.5,	45
⋮	⋮	⋮				
Nozzle 1,2,3,4 & 5	20%	37,	37.5,	...	,44.5,	45
	40%	37,	37.5,	...	,44.5,	45
	60%	37,	37.5,	...	,44.5,	45
	80%	37,	37.5,	...	,44.5,	45
	100%	37,	37.5,	...	,44.5,	45

Table 4.1: Test Matrix

4.5 Adjustment of Static Head during the Experiments

The experiments conducted in the project[12] were all done at a static head of 45 m. The first part of the experiments done in this thesis were conducted with the same static head. Due to vibration caused by the pump that caused the nozzle housing to fail it was lowered to 35 m. During the test at all nozzles 100% open the static head was further reduced to 30 m. This was done after the generator failed to hold the torque at this nozzle configuration during the test conducted in 2005. A discussion about the effect of the lowering of static head on the hydraulic efficiency may be found in Chapter 9.3.

4.6 Post Processing of Data from the Experiments

The data from the experiments were imported into MatLab and rearranged the following post processing steps were conducted.

- Step 1: For each number of nozzles, a surface was spline fitted to the efficiency data.
- Step 2: The best efficiency for each point in the n_{11} and Q_{11} span was extracted. A new surface was spline fitted to the extracted data.
- Step 3: Step 1 and 2 was repeated for the efficiency data with Q_{11Z} .

The MatLab scripts for importation and surface fittings is shown in Appendix G. These are also found in the folder *MatLab* on the CD following this thesis. In addition the data file with normalized data from MatLab, *DATA.mat*, is also included along with the following executable scripts:

- | | | |
|--------------------------|---|---|
| RUNME.m | - | General script including all plotting functions |
| dyse_norm_cont_plotter.m | - | Plot Hill diagrams for individual nozzles |
| norm_cont_plotter.m | - | Plot complete Hill diagram |
| q11_plotter.m | - | Plot the efficiency lines for constant n_{11} |

They all require the input of what definition of reduced volume flow they should be plotted against in addition to choices to include uncertainty intervals, best point of efficiency indication, transition lines and fitted lines.

Chapter 5

Optimization of the Distributor

During the project[12] the head loss in the distributor was measured and simulations of the distributor were conducted. The measurements were used to verify the simulations. The results of the measurements and simulations are found in Chapter 3.2 and 3.3 respectively. The measurements showed a significant head loss through the distributor. One of the goals of this thesis was to minimize the head loss through the distributor.

Figure 5.1 shows the original distributor with the throat, dA , throat length, x , upstream velocities and volume flow indicated. As seen in the figure the original distributor contains many sharp bends, especially those directly upstream of the outlet to the nozzles. These will lead to large losses in the main pipe of the distributor as well as well as a swirling secondary flow at the outlet to the nozzles. In Figure 3.6 it is also evident that the throat over each nozzles does not correspond with an equal volume flow out of each nozzle. After a discussion with Hydroenergi it was decided that the optimization would be based on the original distributor and would not include a complete redesign. This decision was also based on the time and resources available during this thesis. Based on this, three different strategies were tested and the changes done are presented in this chapter.

The results of the optimization strategies is shown in Chapter 8 and are discussed in Chapter 9.

The original distributor is constructed from standard ISO-pipes while the pipes in the laboratory are Metric-pipes. This produced a sudden increase in pipe area at the inlet to the distributor which was included in the previous simulations. During the optimization the diameter of the inlet increased which led to a larger increase in area at the inlet. To ensure equal inlet conditions in all simulations the diameter of the inlet pipe was adjusted so that the diameter ratio remained the same. The remodeling of the throat optimized distributor was conducted by Hydroenergi. The implementation of the remaining optimization strategies in the model were conducted as a part of this thesis.

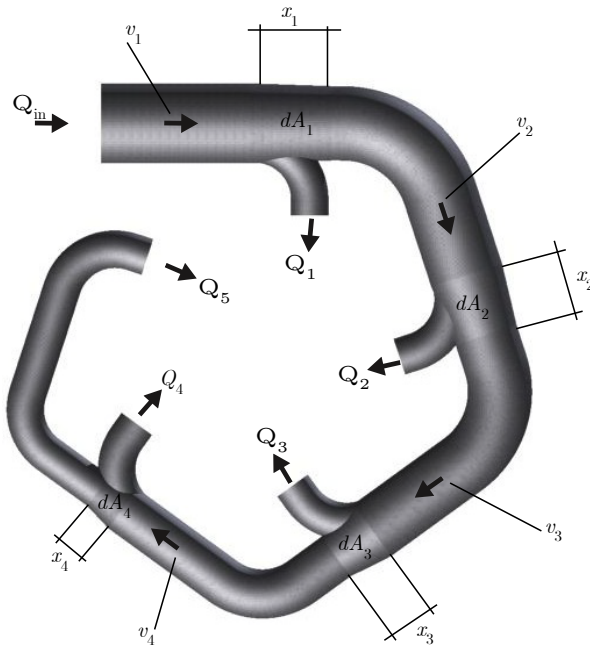


Figure 5.1: Schematic drawing of the distributor

5.1 Optimization of the Throat

As seen in Figure 3.6 the throat over the nozzle outlets does not correspond to the optimal discharge through the nozzle. This problem has been solved by calculating the optimal throat backwards from the last nozzle with Equation (5.1). The diameter of the last pipe section was kept the same as in the original while the diameter in the other parts were calculated by setting the discharge through each nozzle equal to a fifth of the total volume flow, $Q_i = \frac{Q_{in}}{5}$. The distributor after this optimization strategy was implemented is shown in Figure C.1.

$$dA_i = \frac{Q_i}{v_i^*} \quad (5.1)$$

The results of the simulations may be seen in Chapter 8 and . The table beneath shows the variation in area in the locations of v_i in Figure 5.1.

i	Change in area
1	7.37%
2	0%
3	1.29%
4	13.64%
5	0%

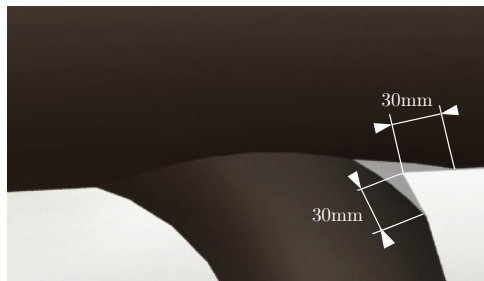
Table 5.1: Change in area after throat optimization

The remaining optimization strategies were implemented on the throat optimized distributor to ease the modeling work.

5.2 Additional Primitive Guide Vanes

On the original distributor the only thing leading the flow into the nozzle outlets is the throat. The throat optimized distributor was remodeled so that it included primitive guide vanes at the downstream corner of the nozzle outlets. Figure 5.2 shows the outlet to the first nozzle with and without the

primitive guide vane. It was modeled by cutting an equal part out at all the outlets that extended an absolute distance of 30 mm into the main pipe and the outlet pipe. The curvature of the lower surface of the cut was set equal to half the curvature of the outlet pipe bend. The throat optimized distributor after the primitive guide vanes were implemented is shown in Figure C.2.



(a)

Figure 5.2: The nozzle outlet with the cut producing the primitive guide vane indicated.

5.3 Change of the Throat Length and Position

The position and length of the throat over the nozzle outlets differ significantly between the nozzles. This was believed to have an effect on the head loss through the distributor. The belief was based on the pressure contours from the CFD simulations done on the original distributor. The contour for nozzle 3 is shown in Figure 5.5. From the pressure contours it is evident that a stagnation point exists on the pipe wall in the outlet to nozzle 2 & 3. At the outlet to nozzle 1 & 4 it is located at the intersection between the nozzle outlet and the main pipe. The cause of the difference in the location of stagnation point was believed to be secondary swirl flow in the pipe. These swirls are caused by the bends in the pipe [15] and were thought to be affected by length and position of the throat at the

nozzle outlets. The hypotheses was tested by changing the throat length and position to mimic that of the throat over nozzle 1 and 4.

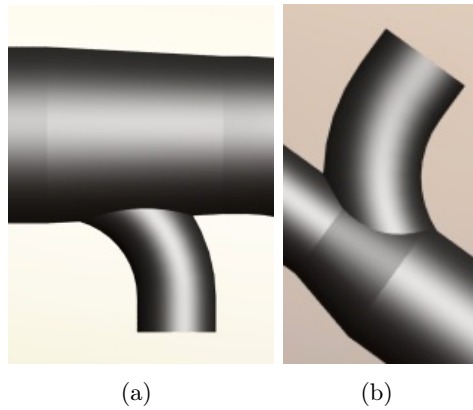


Figure 5.3: Nozzle 1 (a) and nozzle 4 (b)

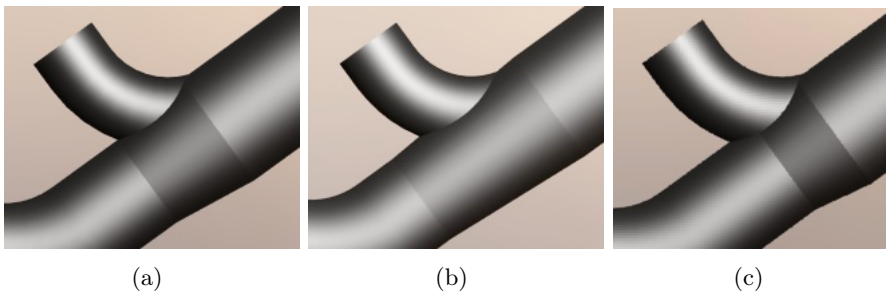


Figure 5.4: Outlet to nozzle 3 as on the throat optimized distributor (a), when it was changed to mimic that at nozzle 1 (b) and nozzle 4 (c)

The outlet to nozzle 3 as it was on the original distributor and as it was after the mimicking may be seen in Figure 5.4. Figure C.3(a) and C.3(b) shows the distributor after the throat was made to mimic that at nozzle 1 and 4 respectively.

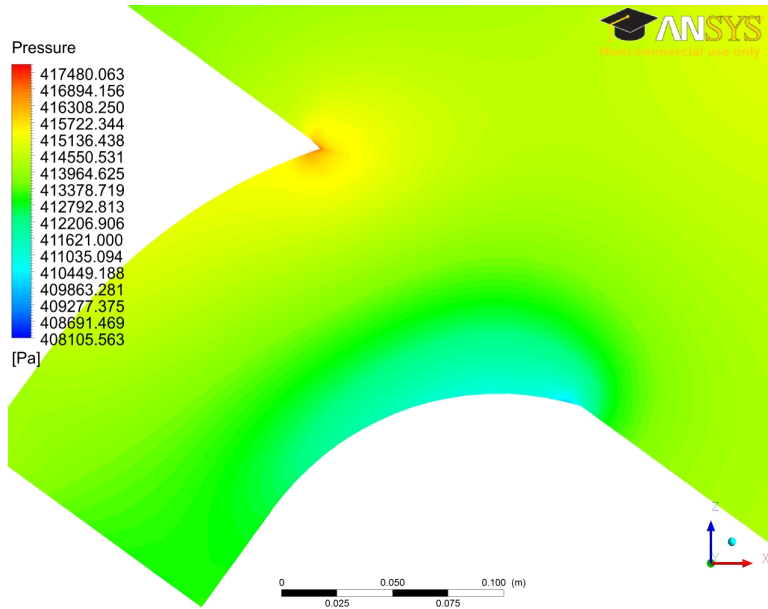


Figure 5.5: Pressure contour at nozzle 3

Chapter 6

Simulation

In addition to the experiments a number of simulation of the distributor was conducted using Computational Fluid Dynamics (CFD). The simulation were done with ANSYS Workbench and CFX and the settings used for the simulation are presented in this chapter. The Computer Aided Design (CAD) software AutoDesk Inventor and SolidWorks were used to modify a model of the distributor acquired from Hydroenergi. The CAD-models were meshed with ANSYS Workbench CFX-Mesh and pre-processed in ANSYS CFX-Pre. After the simulations were solved with CFX-Solver they were post-processed in CFX-Post.

6.1 CAD-Modeling

Figure 6.1(a) show the CAD-models of the original distributor made in SolidWorks. It is generally a good tactic to model the volume occupied by fluid rather than that occupied by the pipe wall when the aim is CFD-simulations. The CAD-model acquired from Hydroenergi was therefore inverted so the models solid represented the volume occupied by water instead of the metal of the pipe. Figure 6.1(b) shows the resulting model of the water filled volume.

The water filled volume of the pipe system leading up to the location of the inlet pressure measurement was also added to the CAD-model. The final model that underwent CFD-simulation is shown in Figure 6.2.

Due to a faulty feature in the CFD post processing application the pressure outtakes on the distributor used in the head loss measurements had to be modeled on the new models. These were used as a reference to the location where both the measurements and the results from the previous simulations were located. The pressure measurement outlets upstream of nozzle 1 is shown in Figure 6.4.

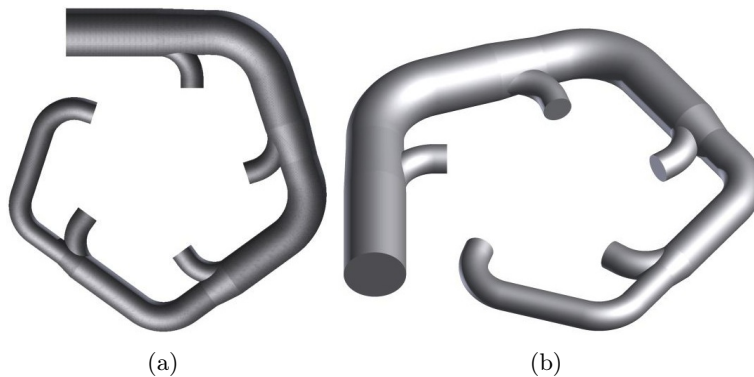


Figure 6.1: CAD-model of distributor (a) and CAD-model of water filled volume (b)

6.2 Meshing

The mesh was refined multiple times to achieve satisfactory mesh fineness in the areas where complex flow was expected to occur. This refinement was done on the outlets of the nozzles as the flow here is turbulent and a fine mesh is needed to simulate the complexity. Figure 6.3 shows the final mesh used in the CFD-simulations. As seen at the inlet and outlets of the

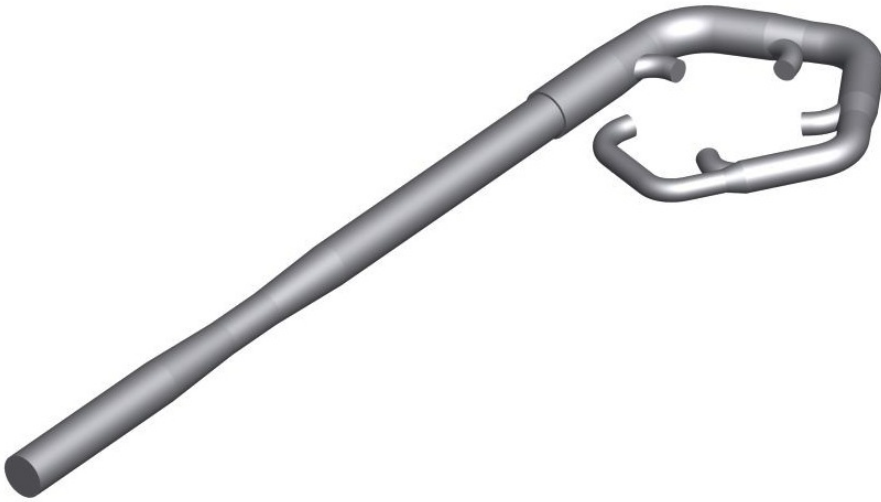


Figure 6.2: Final CAD-model

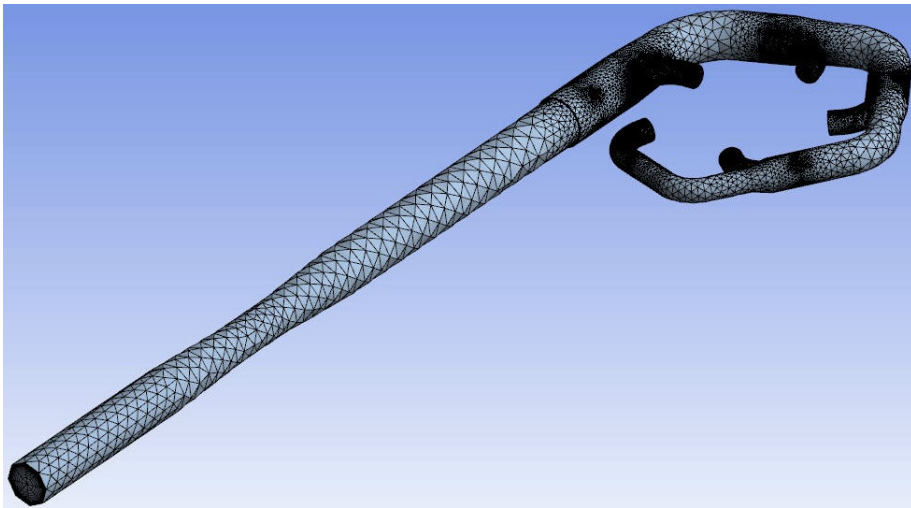


Figure 6.3: Final mesh of CAD-model

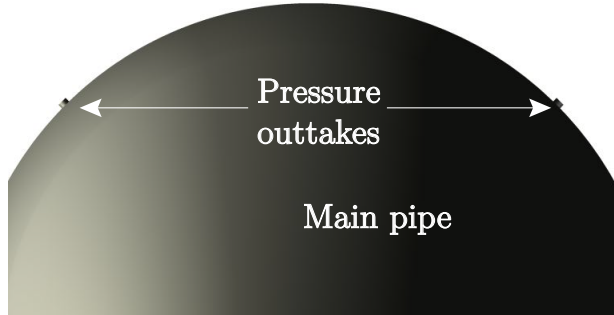


Figure 6.4: Pressure outtakes on the main pipe.

distributor the mesh close to the wall is finer than the mesh in the center of the pipe. This was done to better simulate the boundary layer close to the wall and the turbulence that occurs there.

6.3 Simulation and Boundary Conditions

Table 6.1 shows the boundary conditions used for the CFD-simulation. The choice of boundary conditions and simulation parameters are discussed further in this section.

Domain	Boundary condition
Inlet	Static pressure and high turbulence intensity (10%)
Outlets	Mass Flow Rate
Wall	No slip, rough wall with roughness height $\epsilon = 0.045$ mm
Fluid	Water at 16 °C

Table 6.1: Boundary conditions used during the simulation

Inlet boundary conditions are set on the basis of the pressure measured at the inlet during the experiments conducted in the project[12]. The turbulence is assumed to be of high intensity as the piping upstream of

this location in the rig is complex with outlets, area reductions and sharp, narrow bends.

Outlet mass flow rate is calculated from the volume flow, the outlet area and the density of water found in the experiments. The mass flow rate for all outlets was set to a fifth of the total mass flow rate calculated from the density and volume flow obtained from the experiments. This was done to simulate optimal operation.

Wall roughness height is set based on standard wall roughness height for commercial steel pipes as stated in [15].

Fluid temperature is set as the temperature measured during one of the experiments. The dependency of the fluid temperature was investigated and it was found to have no significant influence on the results.

The conditions during the simulation were steady state since all the measurements during the experiments were taken at near constant operation.

The turbulence models used were the $k - \epsilon$ and *Share Stress Transport* (SST) model. The $k - \epsilon$ model is by itself only valid for infinitely high Reynolds numbers since it does not include the molecular viscosity which is dominant in the near wall region [7]. It is therefor combined with a wall function which is scalable. This is a model developed by ANSYS to avoid the usage of the $k - \epsilon$ model in the very near wall region. The SST model does not need the scalable wall function as it uses one turbulence model, $k - \omega$, in the near wall region. In the free stream it switches to the $k - \epsilon$ model due to the fact that the $k - \omega$ model is over sensitive to turbulence properties of the inlet free stream. The SST model was only used after multiple simulations of the models with the different optimizations implemented showed unnatural flow in some areas.

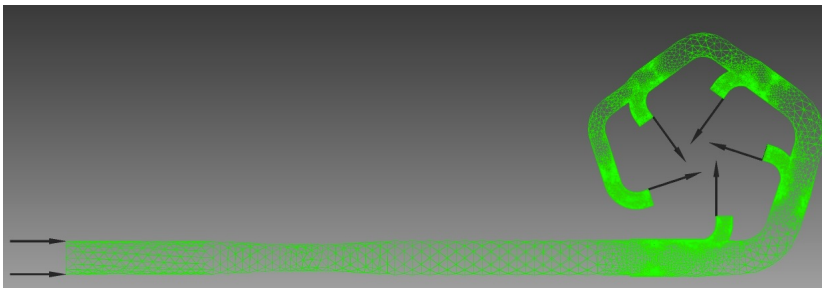


Figure 6.5: Mesh, outlets and inlets in CFX-Pre

Chapter 7

Uncertainty Analysis

7.1 Uncertainty in Experiments

All measurements done during an experiment include some level of uncertainties which have their origin in causes such as inaccuracy within the instrument used to measure the physical quantity and random variations of the measured value. More information on the different types of uncertainties is found in Appendix D.

7.2 Propagation of Uncertainties

7.3 Uncertainties in the Calibration

During calibration of an instrument, different sources of error contribute to the uncertainty. The different errors are shown in Table 7.1 and are defined by IEC [4, Chapter 3.9 and Annex J]. X indicates the property measured by the instrument. The uncertainties are combined to find the total uncertainty with the *Root-sum-square* (RSS) method described in Appendix D.4.

<i>Error</i>	<i>Description</i>
$\pm f_{X_a}$	Systematic error of the primary calibration method
$\pm f_{X_b}$	Random error of the primary calibration method
$\pm f_{X_c}$	Systematic error (repeatability) of the secondary instrument
$\pm f_{X_d}$	Random error of the secondary instrument
$\pm f_{X_e}$	Physical phenomena and external influences
$\pm f_{X_f}$	Error in physical properties

Table 7.1: Component errors in the calibration of an instrument

Uncertainty in the Calibration of Differential Pressure Transmitter

f_{p_a} and f_{p_b} consist of the total error in the calibration method. The dead weight manometer comes with documentation that states that the total error in the instrument $f_{p_{ab}}$ does not exceed $\pm 0.008\%$. This is found by combining f_a and f_b with the RSS method. The documentation can be found in Appendix H.1.

f_{p_c} is the systematic error in the instrument, here being the differential pressure transmitter. During the calibration one looks to minimize this uncertainty by calibrating the signal given by the instrument against a physical quantity stated by the dead weight manometer. During the calibration one does not calibrate for all possible pressures. This produces a systematic uncertainty linked to the instruments response to the pressures not included in the calibration. This relative uncertainty has been denoted $f_{p_{regression}}$ and is found by methods described in Appendix D.3.

f_{p_d} , the random error in the instrument is due to the scatter of the signal. While calibrating the instrument one logs the signal over time and use the mean of the logged values as the instruments response to a given pressure. The uncertainty due to the scatter in the signal at a constant pressure is also included in $f_{p_{regression}}$.

f_{p_e} , the error due to physical phenomena and external influences for the calibration of the differential pressure transmitter. This may originate from changes in the temperature within the instrument. Before calibration the

pressure transducers had been installed in the rig for several weeks. The assumption that it had reached thermal equilibrium with the surroundings was assumed to be valid and f_{pe} was therefor neglected.

f_{pf} , the errors in the physical properties obtained by either calculation or the usage of international standard data. This uncertainty includes the uncertainty in the measurement of the height difference, Z_{cal} , between the dead weight manometer and the measuring point of the differential pressure transmitter. The uncertainty of the laser level is assumed to be negligible while the assumed uncertainty of the ruler measurement is ± 0.1 mm. With the height difference found to be $Z_{cal} = 0.02724$ m the uncertainty $f_{pf} = \pm 0.367\%$

Combining the uncertainties given above with the RSS-method the maximum total relative uncertainty of the calibration of the differential pressure transmitter at 4.5 bar becomes

$$\max(f_{p_{cal}}) = \pm \sqrt{(f_{p_{ab}})^2 + (\max(f_{p_{regression}}))^2 + (f_{pf})^2} = \pm 0.368\% \quad (7.1)$$

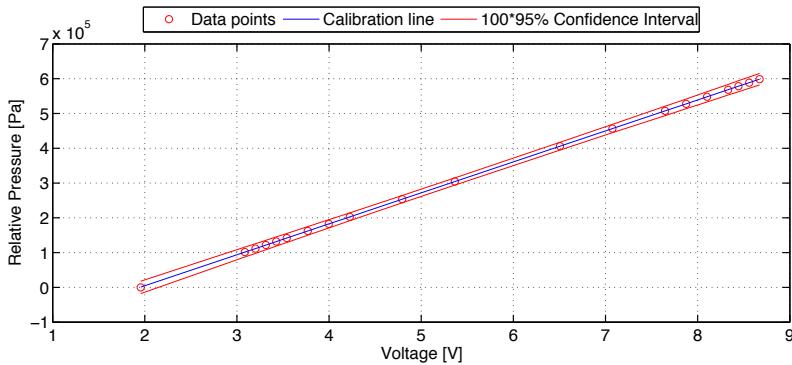


Figure 7.1: Calibration curve and 95% confidence interval scaled by 100 for the differential pressure transmitter

Uncertainty in the Calibration of the Volume Flow Meter

The errors contributing to the uncertainty in the calibration of the volume flow meter are listed in Table 7.2. A more detailed description of the errors is shown in Appendix D.5.1. The calibration curve with the 95% confidence interval is shown in Figure 7.2.

Uncertainty	Description	Magnitude
f_{Q_a}	Systematic error in weighing tank system	$\pm 0.0889\%$ [8]
f_{Q_b}	Random error in weighing tank system	$\pm 0.0503\%$ [8]
$f_{Q_{regression}}$	Systematic and random error in the instrument	$max(\pm 0.3026\%)$

Table 7.2: Errors in the uncertainty in the calibration of the volume flow meter

Combining these errors with the RSS-method the maximum total relative uncertainty for the calibration of the volume flow meter within its range is found to be

$$max(f_{Q_{cal}}) = \pm \sqrt{f_{Q_a}^2 + f_{Q_b}^2 + max(f_{Q_{regression}})^2} = \pm 0.102\% \quad (7.2)$$

Uncertainty in the Calibration of the Torque Transducer

The errors contributing to the calibration uncertainty of the torque transducer, $f_{\tau_{cal}}$, are listed in Table 7.3. A more detailed description of the errors is shown in Appendix D.5.2. The calibration curve with the 95% confidence interval is shown in Figure 7.3.

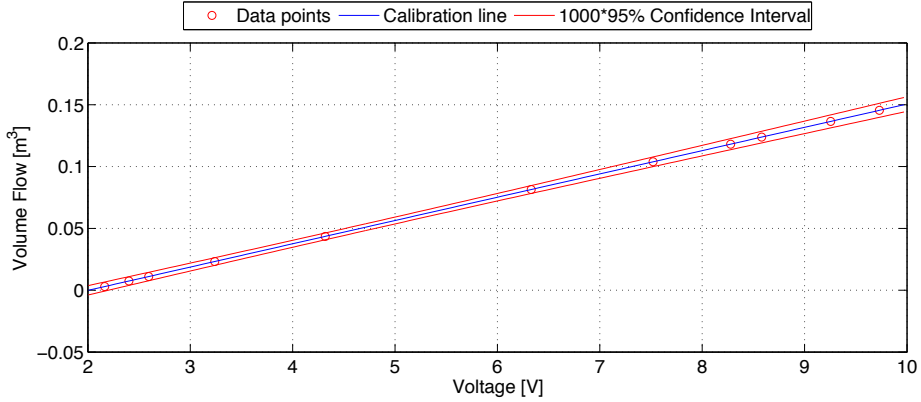


Figure 7.2: Calibration curve and 95% confidence interval scaled by 1000 for the volume flow meter

Uncertainty	Description	Magnitude
f_{τ_W}	Systematic error in weighs and weight bed	$\pm 0.01\%$
$f_{\tau_{arm}}$	Systematic error in the length of the arm	$\pm 0.013\%$
$f_{\tau_{regression}}$	Systematic and random error in the instrument	$max(\pm 0.830566\%)$

Table 7.3: Errors in the uncertainty in the calibration of the torque transducer

Combining these errors with the RSS-method the maximum total relative uncertainty for the calibration of the torque transducer is found to be

$$max(f_{\tau_{cal}}) = \pm \sqrt{max(f_{\tau_{regression}})^2 + f_{\tau_{arm}}^2 + f_{\tau_W}^2} = \pm 0.8307\% \quad (7.3)$$

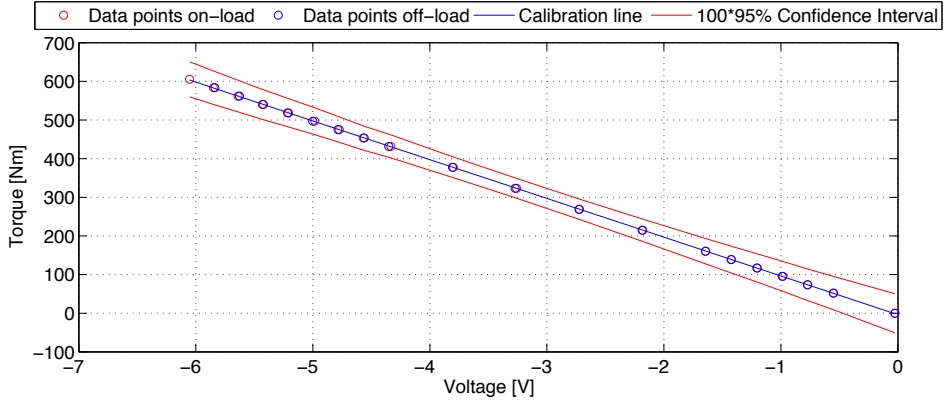


Figure 7.3: Calibration curve and 95% confidence interval scaled by 100 for the torque transducer

Errors in the Calibration of the Thermometer

The thermometer came pre-calibrated from the manufacturer and came with a calibration certificate that is found in Appendix H.2. The absolute uncertainty of ± 0.001 °C, this results in a maximum uncertainty $max(f_{T_{cal}}) = \pm 0.01\%$ for the range of operation which was $T = 10 - 17$ °C.

7.4 Uncertainty of the Tests

After the tests were completed the total uncertainty was found. This is a combination of the calibration uncertainty and other errors from the test itself.

7.4.1 Total Uncertainty of each Component

The uncertainties of the test itself may be separated into the errors given in Table 7.4 [4]. X indicates the property measured by the instrument.

<i>Error</i>	<i>Description</i>
$\pm f_{X_{cal}}$	Systematic error in calibration
$\pm f_{X_h}$	Additional systematic error in the instrument
$\pm f_{X_j}$	Error in physical properties
$\pm f_{X_{k_s}}$	Systematic errors due to physical phenomena and external influences
$\pm f_{X_{k_r}}$	Random errors due to physical phenomena and external influences
$\pm f_{X_l}$	Random error in repeatability of secondary instrument

Table 7.4: Component errors in the test

7.4.2 Uncertainty in the Differential Pressure Measurements

$f_{p_{cal}}$ is a combination of random and systematic uncertainties from the calibration. It is not a constant but varies with the operational point of the turbine. During the tests the tube from the pipe to the differential pressure transmitter was filled with water, hence the water column in the pipe must be added to the pressure measured. Equation (7.4) shows the equation for the pressure in the pipe. This error will be discussed under f_{p_h} .

$$p = p_M + \rho g Z_{test} \quad (7.4)$$

f_{p_h} is caused by the drift of the output signal over time. This phenomenon may be reduced by calibrating often or checking the calibration after the test is completed. The calibration was checked after the tests were completed and showed little signs of drift, and the error is therefor ignored.

f_{p_j} will have a component from the uncertainty of the measurement of Z_{test} . The measurement was done with a rotating laser level and the a ruler with a level on top to ensure that the ruler is vertical. The rotating laser level was set to the pipe center and the distance from the laser line produced by the level to the measuring point of the differential pressure transmitter was measured. The uncertainty in the rotating laser level is assumed to be negligible while the uncertainty in the rules as assumed to be ± 0.1 mm. Combining the errors in length measurement listed above

and the error in calculation of ρ from Chapter 7.4.6 makes the additional systematic uncertainty in the secondary instrument $f_{p_j} = \pm 0.218\%$.

$f_{p_{k_s}}$ and $f_{p_{k_r}}$ are the same as f_{p_e} discussed in Chapter 7.3. These errors may be ignored as long as the procedure and conditions are the same during the test as they were during the calibration.

f_{p_l} is found by using the student-t confidence interval for the logged data from the tests. The method is described in Appendix D and in more detail in Appendix D.2. The maximum random uncertainty during the test were $f_{p_l} = \pm 4.48 \cdot 10^{-4}\%$.

The total uncertainty for the pressure measurements during the tests are found with Equation 7.5.

$$\max(f_p) = \pm \sqrt{(\max(f_{p_{cat}}))^2 + (\max(f_{p_l}))^2} = \pm 0.4277\% \quad (7.5)$$

It is evident that the uncertainty in the pressure measurements is dominated by the uncertainty in the vertical distance Z in both the calibration and in the test setup.

7.4.3 Uncertainty in the Volume Flow Measurements

The uncertainty in the volume flow measurements are calculated with the same component uncertainties as for f_p . Significant errors in the volume flow measurements are shown in Table 7.5. A more detailed description of the significant and negligible errors is shown in Appendix D.6.1.

Uncertainty	Description	Magnitude
$f_{Q_{cat}}$	Systematic error in the calibration	$\max(\pm 0.102\%)$
f_{Q_t}	Random error in the measurements	$\max(\pm 0.1345\%)$

Table 7.5: Errors in the uncertainty in the volume flow measurements

These uncertainties combined leads to the maximum total uncertainty in the volume flow measurements

$$\max(f_Q) = \pm\sqrt{(\max(f_{Q_{cal}}))^2 + (\max(f_{Q_l}))^2} = \pm 0.169\%$$

7.4.4 Uncertainty in the Torque Measurements

The uncertainty in the torque measurements are calculated with the same component uncertainties as for f_p . Significant errors in the torque measurements are shown in Table 7.6. A more detailed description of the significant and negligible errors is shown in Appendix D.6.2.

Uncertainty	Description	Magnitude
$f_{\tau_{cal}}$	Systematic error in the calibration	$\max(\pm 0.8307\%)$
f_{τ_l}	Random error in the measurements	$\max(\pm 2.97 \cdot 10^{-5}\%)$

Table 7.6: Errors in the uncertainty in the torque measurements

The uncertainties combined leads to a maximum total uncertainty in the torque measurements

$$\max(f_\tau) = \pm\sqrt{(\max(f_{\tau_{cal}}))^2 + (\max(f_{\tau_l}))^2} = \pm 0.8307\%$$

7.4.5 Uncertainty in the Temperature Measurements

The uncertainty in the temperature measurements are calculated with the same component uncertainties as for f_p . Significant errors in the torque measurements are shown in Table 7.7. A more detailed description of the significant and negligible errors is shown in Appendix D.6.3.

Uncertainty	Description	Magnitude
$f_{T_{cal}}$	Systematic error in the calibration	$max(\pm 0.01\%)$
f_{T_i}	Random error in the measurements	$max(\pm 6.8 \cdot 10^{-5}\%)$

Table 7.7: Errors in the uncertainty in the temperature measurements

These uncertainties combined to the maximum total uncertainty in the volume flow measurements

$$max(f_T) = \pm \sqrt{(max(f_{T_{cal}}))^2 + (max(f_{T_i}))^2} = \pm 0.01\%$$

7.4.6 Uncertainty in Calculating Density of Water

The density of water is calculated as a function of pressure and temperature and the uncertainty in calculating the density of water is $f_\rho = \pm 0.01\%$ [8]. This uncertainty will not be significant in the total uncertainty of the hydraulic efficiency and is therefore neglected.

7.4.7 Uncertainty in the Rotational Speed Measurement

The rotational speed measurement system was checked as recommended by IEC [4] with an optical rotation counter and a piece of reflective tape that was taped to the shaft. This gave confirmation that the rotational speed measurement system was approximately correct. The systematic uncertainty is used $f_n = f_{n,s} = \pm 0.025\%$ as stated in [4]. The maximum random uncertainty for the rotational speed measurements during the tests was found to be $f_{n_i} = 1.27 \cdot 10^{-5}$. This gave a total uncertainty

$$f_n = \pm \sqrt{(f_{n,s})^2 + (f_{n_i})^2} = \pm 0.025\%$$

7.4.8 Total Uncertainty for the Hydraulic Efficiency

The uncertainty of η can be found from Equation (7.6) which is derived from Equation (2.10) with methods described in [14] and [4].

$$f_{\eta_h} = \pm \frac{(e_{\eta_h})}{\eta_h} = \pm \sqrt{(f_Q)^2 + (f_E)^2 + (f_P)^2} \quad (7.6)$$

$$f_E = \pm \frac{(e_E)}{E} = \pm \left\{ \frac{\sqrt{\left(\frac{e_{\Delta p}}{\bar{\rho}}\right)^2 + (ge_{Z_{test}})^2 + \left(\frac{e_{v_1^2}}{2}\right)^2}}{\frac{\Delta p}{\bar{\rho}} + gZ_{test} + \frac{v_1^2}{2}} + f_{\Delta E} \right\} \quad (7.7)$$

$$f_P = \pm \sqrt{(f_\tau)^2 + (f_\omega)^2} \quad (7.8)$$

In Equation (7.7) the uncertainties are expressed as absolute (e) while the uncertainties found in this section are relative (f). The following equations are used to express the absolute uncertainty by the calculated relative uncertainty.

$$\frac{e_{\Delta p}}{\bar{\rho}} = \left(\frac{\Delta p}{\bar{\rho}}\right) f_{\Delta p} \quad (7.9)$$

$$\frac{e_{v_1^2}}{2} = v_1^2 f_{v_1} \quad (7.10)$$

$$f_\omega = f_n \quad (7.11)$$

v_1 in the expression for total uncertainty is calculated with $v_1 = Q/(\pi r^2)$. Therefor the uncertainty f_{v_1} is a combination of the uncertainties in the volume flow measurement and the radius of the pipe. The expression for the uncertainty in the velocity measurement is shown in Equation (7.12).

$$f_{v_i} = \sqrt{f_Q^2 + 2\left(\frac{e_r}{r}\right)^2} \quad (7.12)$$

The uncertainty for the velocity is calculated with Equation (7.12) with f_Q as found in Chapter 7.4.3. The diameter is given by the producer and its uncertainty is assumed to be $e_r = \pm 0.1$ mm. The maximum total uncertainties in the velocity at the inlet to the distributor $max(f_{v_1}) =$

0.1345%.

The maximum total uncertainty in the efficiency measurements $\max(f_\eta) = 1.548\%$. This uncertainty is dominated by the uncertainty in the torque measurements at low torque.

All the uncertainties stated in this chapter are the maximum uncertainties. These maximum uncertainties rarely coincide at points in the complete Hill diagram with exception for very low volume flow where the torque is low. The total uncertainty in the best point of efficiency was found to be 0.3837%.

Chapter 8

Results

In this chapter, results from both experiments and simulations are presented. They are discussed in Chapter 9. All the efficiencies have been normalized so that the maximum efficiency is 1, due to confidentiality.

8.1 Results from the Experiments

In this section, the Hill diagrams found by the post processing procedure described in Chapter 4.6 are presented. The diagrams created from the experiments with 1 and 2 nozzles open are shown in Figure 8.1 and 8.2 respectively. The Hill diagrams for 3, 4 and 5 nozzles are found in Appendix F.1. The complete Hill diagram for the turbine plotted against Q_{11} and Q_{11z} are shown in figure 8.3 and 8.4 respectively.

In this thesis the test series were conducted with a constant and fairly large variation in volume flow. This resulted in a Hill diagram that only gives an indication on the location of the best point of operation. In the complete Hill diagrams the iso-curves for the highest efficiency indicate that there exists two candidates for the best point of operation. These are indicated in the complete Hill diagrams and are located at $n_{11} = 40.5$ and $n_{11} = 41.5$

at the same Q_{11} and Q_{11Z} individually.

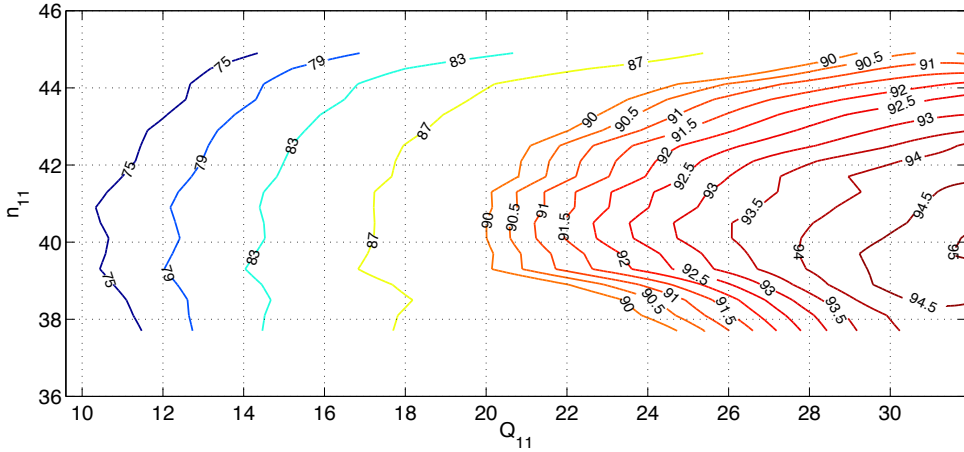


Figure 8.1: Hill diagram for 1 nozzle plotted against Q_{11}

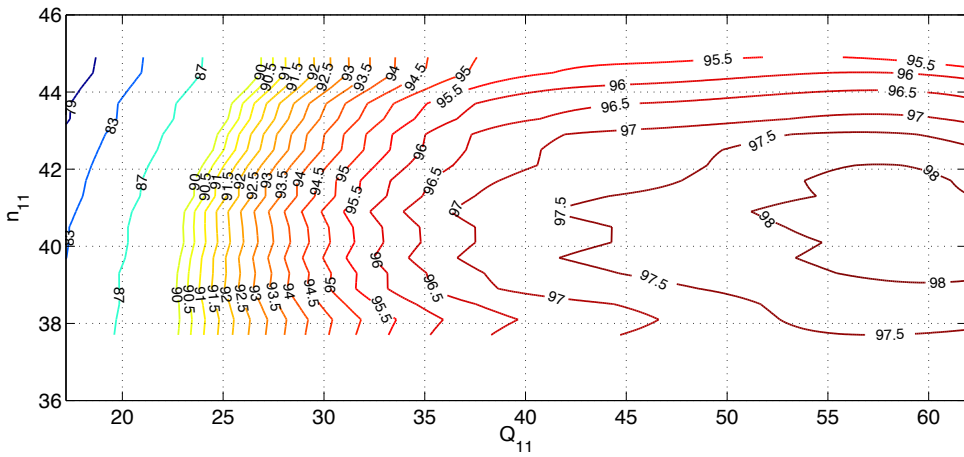


Figure 8.2: Hill diagram for 2 nozzles plotted against Q_{11}

With an increasing number of nozzles open, the Hill diagram stretches

further up the Q_{11} range and has a local peak in efficiency at the end of the Q_{11} range. The height of this peak increases with the number of nozzles open. A difference in where the “ridge” in the two Hill diagram with regard to n_{11} is noticeable. This difference is discussed in Chapter 9.2.

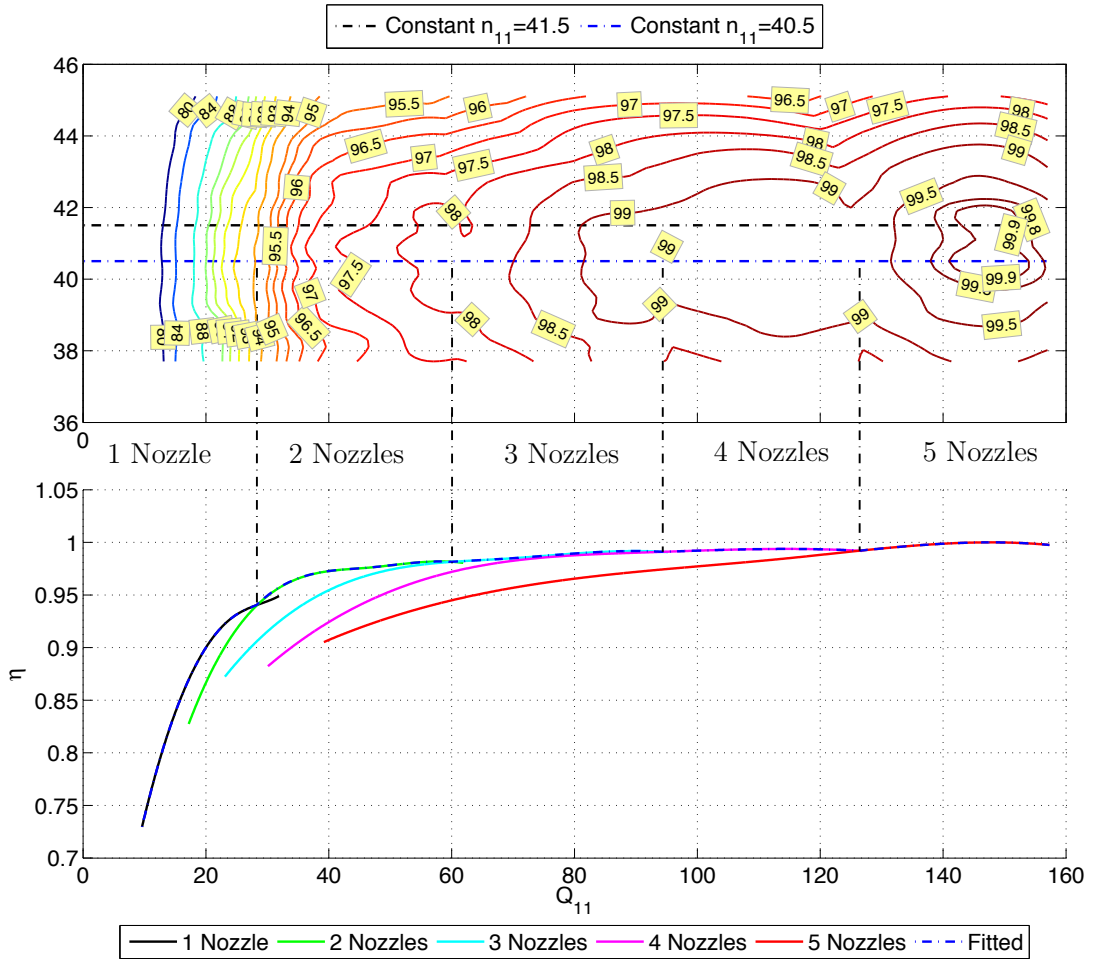


Figure 8.3: Complete Hill diagram plotted against Q_{11} with $n_{11} = 40.5$ and $n_{11} = 41.5$ indicated and the efficiency lines for different number of nozzles and the fitted line with $n_{11} = 40.5$ plotted against Q_{11} .

The upper part of figure 8.3 shows the complete Hill diagram of the turbine plotted against Q_{11} with $n_{11} = 40.5$ and $n_{11} = 41.5$ indicated. One should notice the indents in the constant efficiency curves for the higher efficiencies in the complete Hill diagram. This is discussed in Chapter 9.1.

The lines shown in the lower part of the figure indicate the turbine efficiency at different Q_{11} values with constant $n_{11} = 40.5$. These are the same lines as shown in Figure 3.1. These lines are extracted from the surfaces fitted to the results with the procedure described in Chapter 4.6. In addition, the fitted line is plotted which is extracted from the surface fitted to the best efficiency for points in the $n_{11} - Q_{11}$ domain.

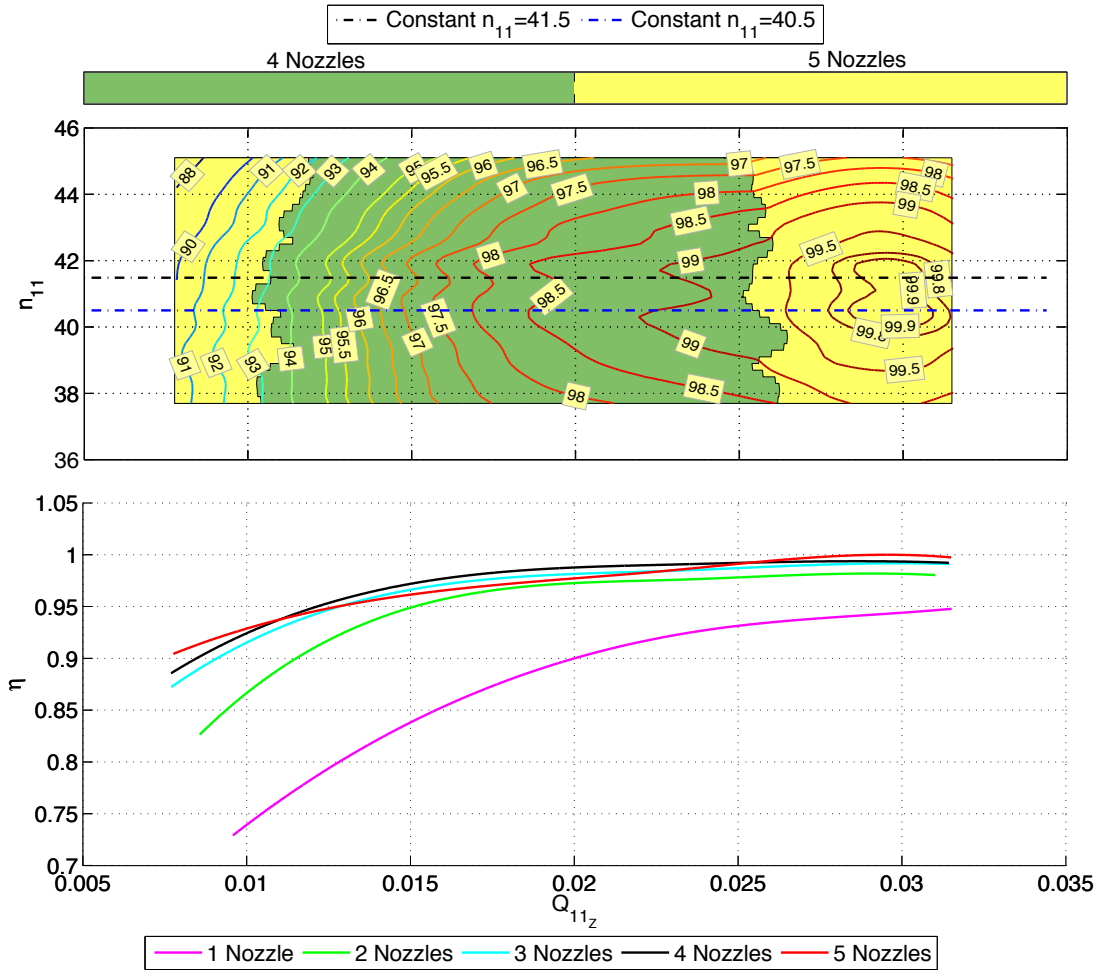


Figure 8.4: Complete hill diagram plotted against Q_{11z} with $n_{11} = 40.5$ and $n_{11} = 41.5$ indicated in the upper part of the figure. The lower part of the figure shows the efficiency lines for different number of nozzles with constant $n_{11} = 40.5$ plotted against Q_{11z} .

The upper part of Figure 8.4 shows the complete Hill diagram of the turbine plotted against Q_{11z} with $n_{11} = 40.5$ and $n_{11} = 41.5$ indicated. The figure shows that 1, 2 and 3 nozzles open are not used in the complete Hill diagram. This is due to the fact that the results from these runs are always exceeded by 4, 5 nozzles or both with regard to efficiency as seen in the lower part of the figure. In addition, a change between 4 and 5 nozzles open in the middle of the complete Hill diagram is seen. This is discussed in Chapter 9.1.

The lines in the lower part of the figure indicate the efficiency of the turbine for different Q_{11z} values and constant $n_{11} = 40.5$. These are extracted from the surfaces fitted to the test with different number of nozzles open.

8.2 Results from the Simulations

In this chapter the results from the optimization of the distributor are presented. Figure 8.5 shows the head loss through the distributor for the original and after the different optimization strategies were implemented. As seen in the figure, the head loss through the distributor is lowest for the throat optimized distributor. The reduction in total head loss after the throat was optimized was found to be 66.67%. The flow within the throat optimized distributor is not optimal, but the other optimization strategies led to equal or worse flow. This can be seen in the velocity contours found in Appendix F.2, which also include the total pressure contours. Based on this the throat optimized distributor was chosen as the simulation to compare with the original. The total pressure contour plots of the distributors with the other optimizations implemented are found in the same appendix. The two distributors are compared by comparing the velocity and total pressure contours as well as the velocity vectors through the outlet to nozzle 1. These figures are presented in this chapter and discussed in Chapter 9.

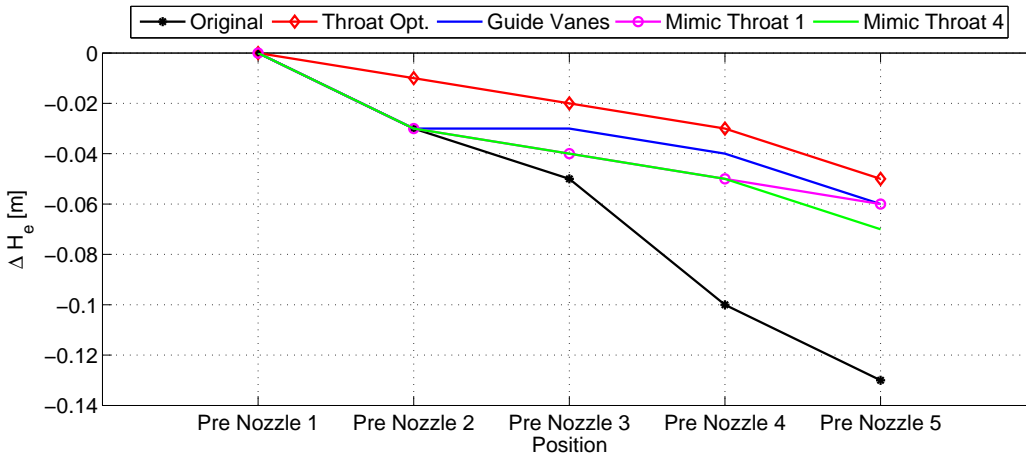
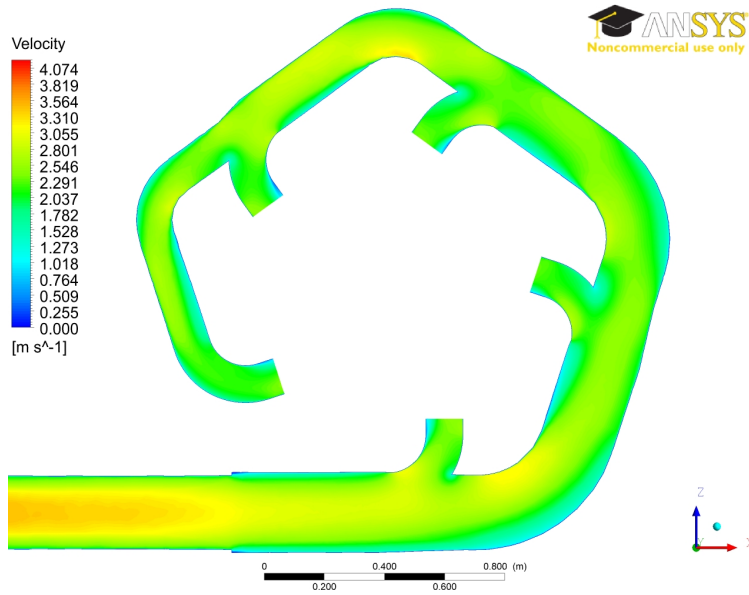
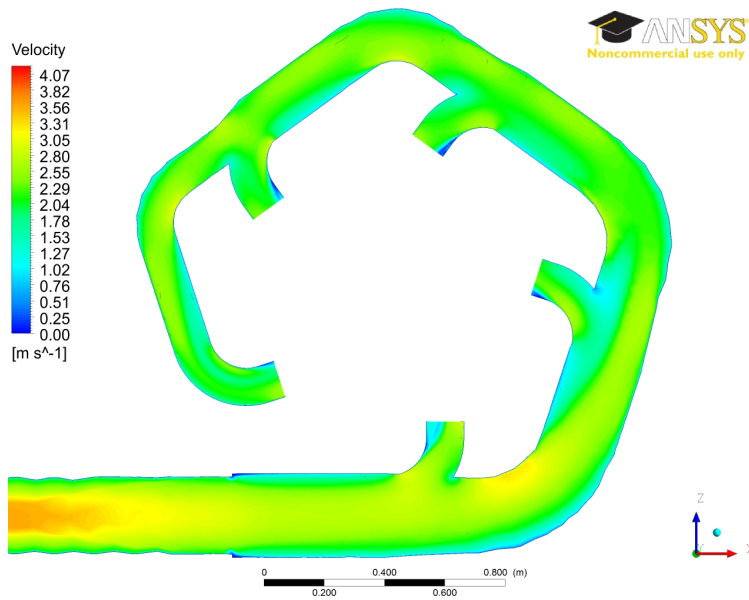


Figure 8.5: The head loss through the distributor for the original and different optimization strategies.



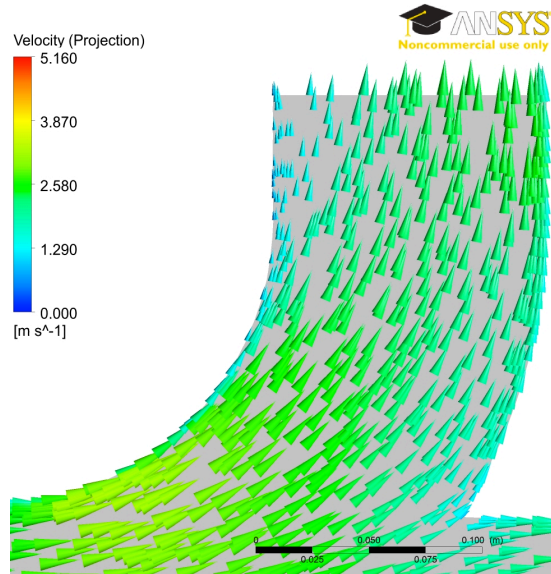
(a) Original distributor



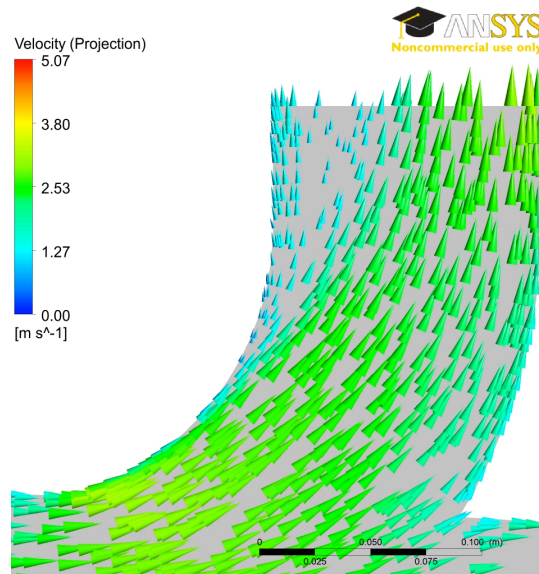
(b) Throat optimized distributor

Figure 8.6: Velocity contours on the original (a) and throat optimized (b) distributor.

From Figure 8.6 it is evident that the velocity distribution in the nozzle outlets in the throat optimized distributor are not optimal. In addition, one should notice that the velocity along a stream line in the pipe center vary significantly in the original compared with the throat optimized. The reasons for this are discussed in Chapter 9.4. The edges of the inlet pipe and main pipe in the distributor appear to differ in the simulations done this semester compared to those done previously. This is due to the mesh but will have a negligible effect on the solution.



(a) Original distributor



(b) Throat optimized distributor

Figure 8.7: Vector plot of the velocity in the outlet to nozzle 1 in the original (a) and throat optimized (b) distributor.

In Figure 8.7 the effect of the change in transition to the outlet is visible. The bend is smoother and longer in the original distributor compared to the throat optimized. This gives the flow a a more uniform outflow, but it is not optimal in the original distributor. The total pressure distribution and tangential velocity at the outlet to nozzle 1 is shown in Figure 8.8, a difference in total pressure and swirl strength is evident.

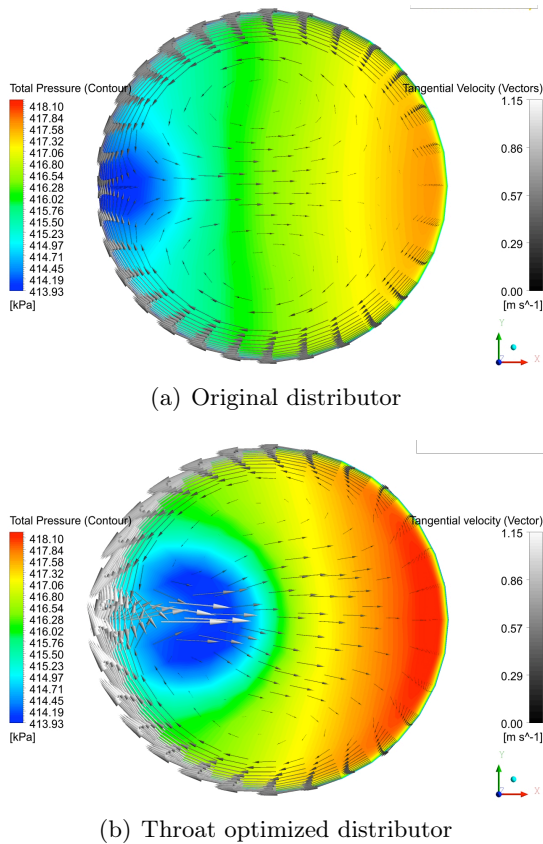


Figure 8.8: Total pressure contours and velocity vectors at to outlet to nozzle 1 on the original (a) and throat optimized (b) distributor.

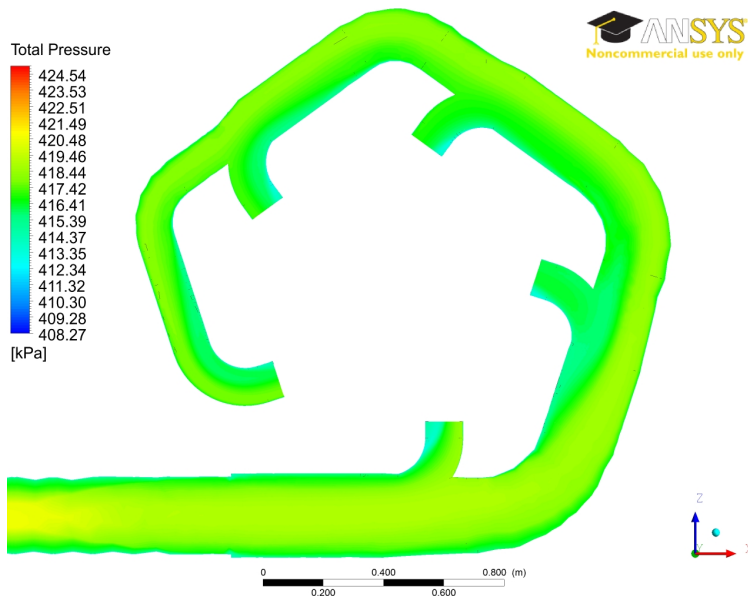
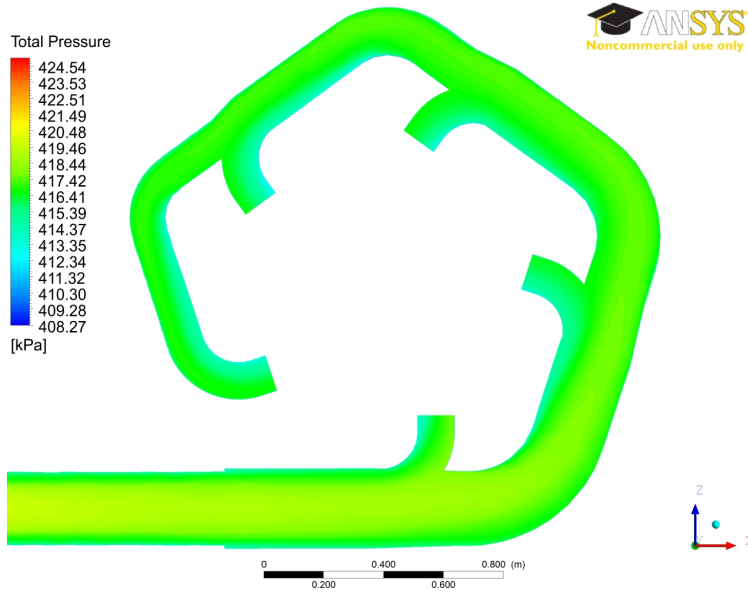


Figure 8.9: Total pressure contours on the original (a) and throat optimized (b) distributor.

From Figure 8.9 it is evident that the total pressure through the distributor is greater in the throat optimized distributor than the original. This is also evident in Figure 8.5 and is discussed in Chapter 9.4.

Chapter 9

Discussion

9.1 Hill Diagram

In the complete Hill diagram in the upper part of Figure 8.3 one notices that the constant efficiency lines for the high efficiencies contain indents. These are not present in the Hill diagrams presented in the literature [2] and [6]. Figure 9.1 shows the transitions between the number of nozzles used to achieve the highest efficiency. From the figure it is evident that the indents coincide with these transitions and are believed to be caused by location of the measurement points. A complete Hill diagram with the measurement points indicated may be seen in Figure F.1.

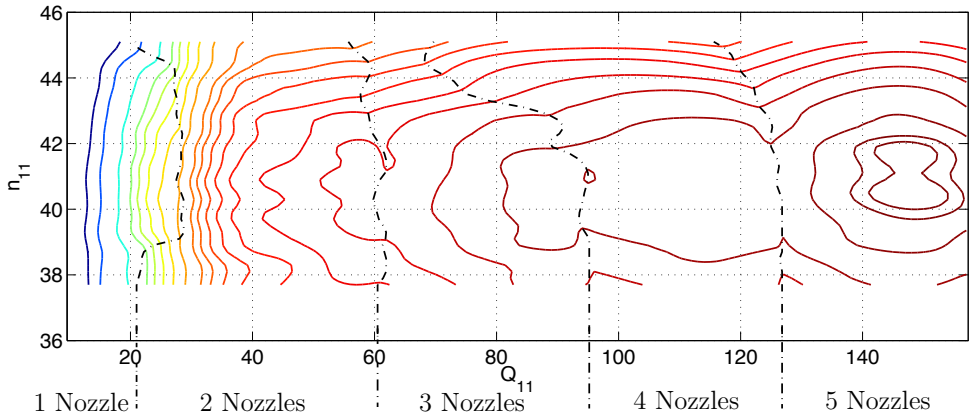


Figure 9.1: Hill diagram with the transition between the number of nozzles open indicated

The figure also shows that the change from 3 to 4 nozzles for high values of n_{11} tends to happen at a lower Q_{11} . This is believed to be caused by the amount of water hitting the next bucket, the back wash, increasing at higher rotational speed. This is caused by a decrease in the time it takes for the next bucket to enter the water domain. By distributing the same volume flow water out of more nozzles the amount of water in each bucket, hence the amount of back wash also decreases. The water hitting the next bucket may give a negative torque on the shaft and hence lower the power output and efficiency. It may also cause cavitation on the back of the bucket. A similar phenomena is seen for the transition between 1 and 2 nozzles. The Q_{11} value for the transition changes rapidly at $n_{11} \approx 39$ and $n_{11} \approx 44.5$. This is caused by the shape of the Hill diagram for 1 nozzle seen in Figure 8.1. The “ridge” of high efficiency for 1 nozzle moves the transition to 2 nozzles to a higher Q_{11} . This is believed to be caused by the fact that the test with 1 nozzle was done with the buckets with a lower pitch angle. This is discussed further in Chapter 9.2.

The complete Hill diagram plotted against Q_{11z} in Figure 8.4 only consist of values acquired from the tests with 4 and 5 nozzles open. This is due to the fact that the tests with 1, 2 and 3 nozzles open is always exceeded in efficiency by at least one of the tests with 4 and 5 nozzles. This is also evident in the lower part of the figure. The fact that 4 nozzles are used in the middle of the Q_{11z} range is believed to be due to the large losses in the distributor between nozzle 3 and 4. The pressure distribution through the original distributor shown in Figure 8.9(a) also show these losses. When investigating the lower part of the figure it is evident that the general shape of the efficiency line when using 4 nozzles differ slightly from the shape of the lines for 1, 2 and 3 nozzles. The efficiency line for 5 nozzles appear to differ significantly in shape compared to the rest. These differences are thought to be caused by the losses in the distributor. When all the nozzles are open these losses increase due to the increase in the local velocity(2.15). The discharge through nozzles 4 and 5 will decrease, decreasing the local efficiency of these nozzles and the turbine. When only 4 nozzles are used the effect is smaller due to lower velocity, but still thought to be significant. The increase in loss can also be identified in Figure 8.5 as a an increase in the tilt of the head loss in the original distributor.

As stated in 3.1 the complete Hill diagram indicate two candidates for the best point of efficiency. The difference between the two is 0.0431% which is well inside the uncertainty of the measurements. To locate the best point of efficiency more accurately tests should be conducted with a finer test matrix around the indicated location.

The maximum efficiency measured in this thesis is 0.7557% lower than that measured during the tests done on the buckets with the small pitch angle in 2005. The uncertainty of the measurement is $\pm 0.3837\%$ and if it is assumed positive the efficiency measured in this thesis is 0.3720% lower than that measured in 2005. The uncertainty of the tests conducted in 2005 is not known but it is assumed to be higher than in these experiments. This results in the confidence interval of the measured efficiencies overlapping.

9.2 Effect of Increased Pitch Angle

The increase of the pitch angle will have multiple effects on the flow within the turbine housing and thereby the turbine efficiency. As the bucket enters the jet the water will have a relative velocity towards the tip of the bucket. The impact of the water may cause cavitation on the tip of the bucket [10]. In addition, the water may hit the back of the bucket thereby produce a negative torque. This will lower the torque delivered to the generator and hence the turbine efficiency. The angle between the back of the bucket and the relative velocity should be less than 10° to prevent both problems [3]. The figure below shows the effect of a higher pitch angle on the relative velocity of the water when the bucket enters the jet.

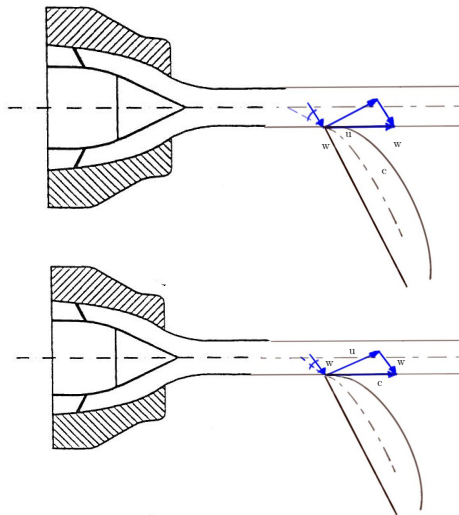


Figure 9.2: The relative velocity of the water as the bucket first enters the jet at a two pitch angles where the lower is the largest. The nozzle in this figure is copied from Figur 1.8 in [1].

A change in pitch angle will also change the angle of attack, β , between the bucket and the jet when it hits the bucket fully as seen in Figure 9.3. This will change both the flow entering, within and exiting the bucket which will also change the transfer of energy from the water to the bucket.

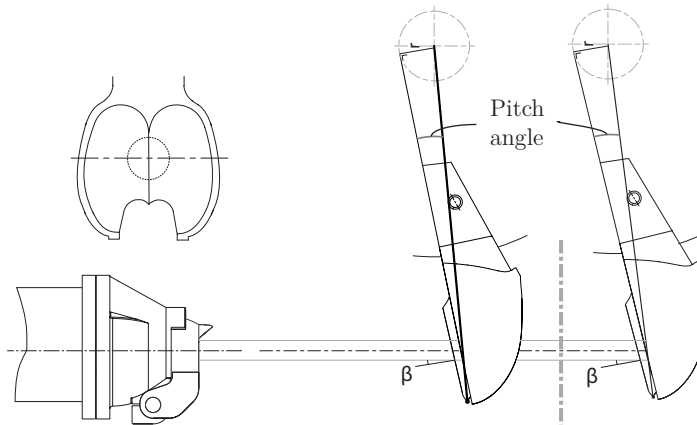


Figure 9.3: Effect of change in pitch angle on the angle of attack for the jet on the bucket, β . This figure is made from parts of Figure 4.5, 7.1 and 14.6 in [10]

The roof of the turbine housing is made with an angle near the shaft as seen in the Figure 9.4. This is done so that the water exiting the bucket will be reflected away from the turbine. With an increase in pitch angle the radial component of the absolute velocity exiting the bucket will increase. As seen in the figure, an increase in the radial velocity component may result in parts of the flow hitting the horizontal part of roof in the turbine housing. Water hitting the horizontal area may be reflected directly down onto the turbine. This may produce a counter force to the rotation of the turbine as well as cavitation. An increase in water droplets in the vicinity of the rotating turbine may also increase ventilation losses from the turbine acting

as a fan in the water saturated air inside the turbine housing.

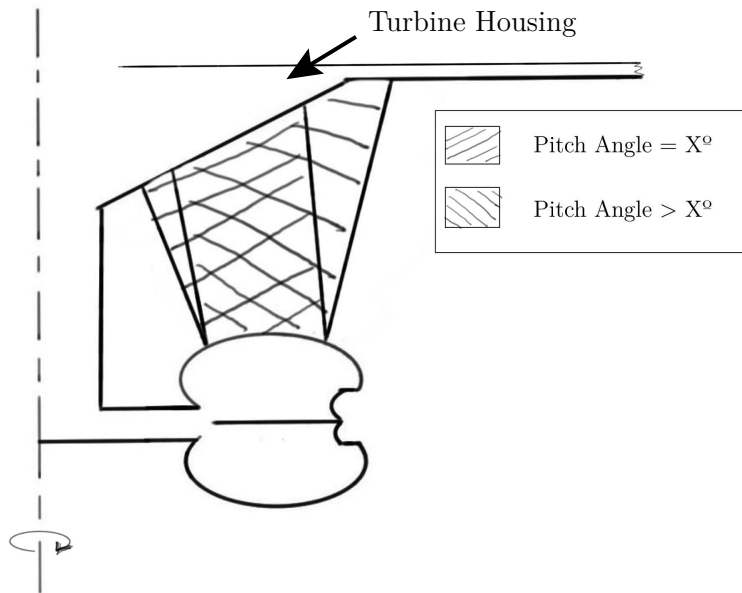


Figure 9.4: A bucket located in the jet seen from behind with the outflow at two different pitch angles

In Figure 8.1 and 8.2 a difference of the location the “ridge” in the Hill diagrams for 1 and 2 nozzles is evident. This may be caused by the difference in pitch angle of the buckets used during the test with 1 nozzle and 2 nozzles. The increase in pitch angle seems to move the location of the “ridge” to a lower n_{11} value. This may indicate that the buckets with a higher pitch angle changes the out flow of the bucket so that back wash occur at a lower rotational speed.

9.3 Effect of Lowered Effective Head

Seim[11] found that the effect of a lower specific head on the hydraulic efficiency was not significant at heads higher than 30 m. This study was done on distributor with only 1 nozzle and is therefore not valid for the setup used in these experiments but it indicates that the effect may be small. From Figure 8.5 it is found that the total head loss through the distributor amount to 0.2889% of the static head. As the static head is reduced the velocity of the water exiting through the nozzle is reduced as Equation (2.3) shows. This reduction will reduce the velocity in the pipes and the distributor and hence the dynamic head, the Reynolds number and hence the friction factor. The reduction in velocity will lead to a lowered geometry head loss as shown in Equation (2.15). The reduction of Reynolds number will lead to an increase in the friction factor but the total friction head loss will be reduced due to the dominance of the velocity in (2.14). This will lead to a small reduction in the losses through the distributor and thereby reduce a difference in the discharge velocity of the nozzles. The magnitude is difficult to quantify and is assumed to be small. But it may still have a significant effect on the hydraulic efficiency.

9.4 Optimal Distributor Design

The optimization strategy that gave the best results with regard to pure head loss was found to be the throat optimization. The reduction in total head loss through the throat optimized distributor was found to be 66.67% compared to the original. This result is not verified by experiments and is therefore only an indication of the effect of the optimization may give.

The flow through the bends making out the outlets to the nozzles was found to be non optimal as seen in Figure 8.7. The flow in the same area in the original distributor is not optimal either, but the area of low velocities in the inner area of the bends are smaller. This is thought to be caused by the sharp bends in the outlets and the subsequent secondary swirl flow. When the distributor was throat optimized the pipe area of the sections

in the main pipe were changed as seen in Table 5.1. The location of the pipes making out the outlets to the nozzles were kept constant while the diameter of the main pipe was increased. Hence, the transition between the main pipe and the outlet pipes changed as is evident by comparing the two figures below. The difference in the transition is believed to be one of the possible causes of the non optimal flow in the outlets. The effect of the change in transition is also evident in the increase in strength of the swirl at the outlet to nozzle 1 seen in Figure 8.8(b) and 8.8(a) respectively. A visual check of the condition of the jet from nozzle 1 was performed during the tests with only this nozzle open. There was no indication of a disturbance in the jet

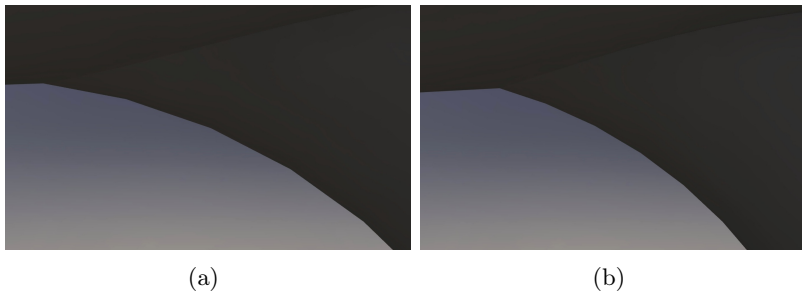


Figure 9.5: Entrance to nozzle 1 outlet on the original (a) and throat optimized (b) distributor

This change in transition is only present where the change in pipe area is large, i.e. the inlet to nozzle 1 and 4. The time did not permit an elimination of this phenomena and the subsequent simulations of the new models.

As noted in Chapter 6.1 the models made during this thesis included the outtakes for the pressure measurement which were not included in the original distributor. These may have a effect on the flow but this is not likely due to their small size compared to the diameter.

Chapter 10

Conclusion and Further Work

The effects of the different changes done with regard to bucket pitch angle and effective head are difficult to quantify. The losses through the distributor is thought to affect the efficiency of turbine when using 4 and 5 nozzles. This is believed to be caused by the high losses between nozzle 3 and 4 in the distributor. The Hill diagrams for 1 and 2 nozzles indicate a difference in the location of the best efficiency with regard to the rotational speed. This may be an effect of the higher pitch angle and the change in flow in the bucket and turbine housing it produces.

The results from the simulations done on the redesigned distributors during this thesis include some unreliabilities due to differences in the models. The results from the simulations gave a 66.67% reduction in head loss for the throat optimized distributor. This result should only be used as an indication but it shows that small changes in the original distributor may give a large reduction in head loss. The remaining problem with the original distributor is the sharp bends in the main pipe and at the outlets to the nozzles. Which lead to a secondary swirl flow at the outlet to the nozzles that will reduce the jet condition if they are significant. The simulations showed an increase of the strength of these swirls in the optimized distributor. This is believed to be partly due to the differences

in the models.

The maximum efficiency of the turbine found in this thesis and in previous tests correspond well within their uncertainty. The efficiency found is lower than that of state of the art Pelton turbines. One of the reasons for this is believed to be the losses in the distributor in addition to the unknown effect of the higher pitch angle.

Future work:

- Conduct more test to achieve better resolution around the indicated best point of operation in the complete Hill diagram.
- Establish a complete Hill diagram for the original design to quantify the effect of the increased pitch angle.
- Test with only one nozzle opened for all the nozzles to investigate the conditioning of the jets and effect of head loss.
- Optimize distributor further with the use of state of the art design with short pipe sections and test the effect of the modeling differences.

Bibliography

- [1] Hermod Brekke. *Grunnkurs i hydrauliske strømningsmaskiner*. 2000.
- [2] Hermod Brekke. *Pumper og Turbiner*. 2003.
- [3] Hermod Brekke. Discussion, 3rd of June 2010.
- [4] International Electrotechnical Commission. *IEC 60193: Hydraulic turbines, storage pumps and pump-turbines - Model acceptance testes*. 1999.
- [5] ISO. *NS-ISO 4185: Måling av væskestrøm i lukkede rør, veiemetode*. 1993.
- [6] Arne Kjølle. *Vannkraftmaskiner*. Universitetsforlaget, 1980.
- [7] Per-Åge Krogstad. The dark art of turbulence modelling, 2009.
- [8] Pål Tore Selbo Storli. Modelltest av francis turbin i vannkraftlaboratoriet ved ntnu, 2006.
- [9] Emil Mosonyi. High-head power plants. volume 2. 1991.
- [10] Alexandre Perrig. Hydrodynamics of the free surface flow in pelton turbine buckets.
- [11] Bjarte Grytil Seim. Flow condition in a pelton runner. Master's thesis, 2008.

- [12] Bjørn Winther Solemslie. Pelton turbin. Technical report, NTNU, 2009.
- [13] Ronald E Walpole, Raymond H Meyers, Sharon L Myres, and Kaying Ye. *Probability and Statistics for Engineers and Scientists*. 2007.
- [14] Anthony J Wheeler and Ahmad R Ganji. *Introduction to Engineering Experimentation, Second Edition*. 2004.
- [15] Frank M White. *Fluide Mechanics*. 2003.
- [16] Z Zhang and M Casey. Experimental studies of the jet of a pelton turbine. *Proceedings of the Institution of Mechanical Engineers ...*, Jan 2007.

Appendix A

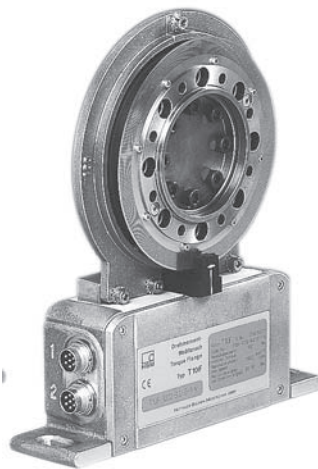
Instrumentation

A.1 Torque measurement

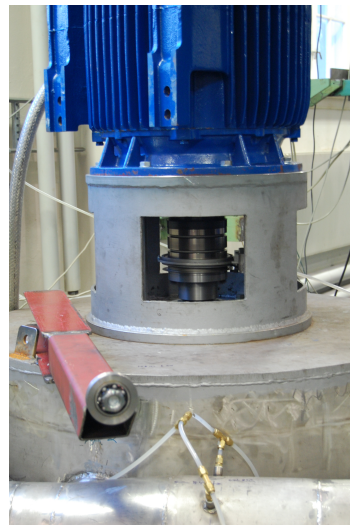
The torque measurement were conducted with torque flange which consist of a rotor and a stator that are not in contact with each other. The rotor is placed between the turbine shaft and the generator shaft. The rotor measures and delivers the torque from on shaft to the other while it transmits the data wirelessly to the stator that surrounds it. The transducer also has an integrated optical rotational speed measuring system, see Appendix A.2 for more information. The torque cell is shown in Figure A.1(a) and it was mounted as shown in Figure A.1(b)

A.2 Rotational Speed measurement

The HBM T10F Torque Flange's optical rotational speed measuring system consists of three main parts; a metallic slotted plate that rotates with the shaft, an infrared light source and a photo detector. As the plate spins the light from the light source shines through the slits in the plate so that the photo detector receives the infrared light in pulses which again produces a frequency signal. The principal of this method for rotational speed measurement is illustrated in Figure A.2.



(a)



(b)

Figure A.1: The HBM T10F Torque Flange (a) and a picture of how it was mounted on the test rig (b)

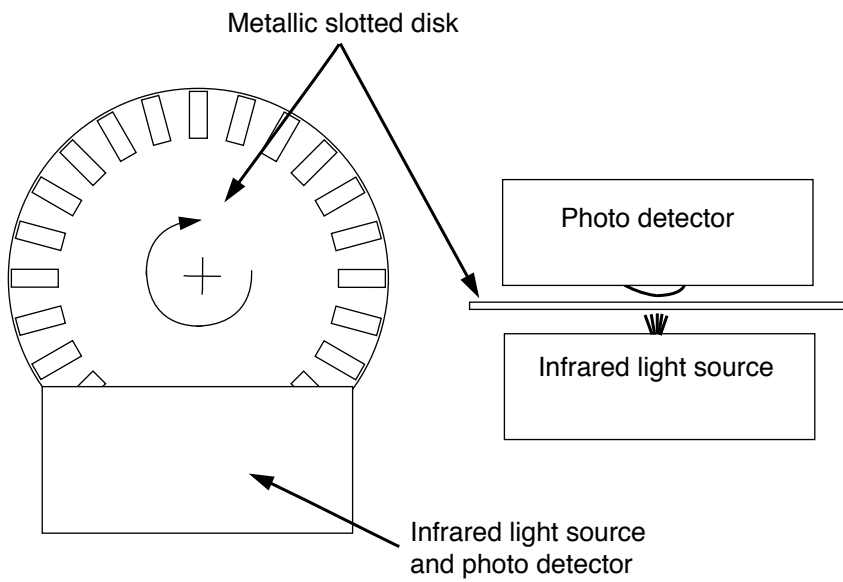


Figure A.2: Principal of optical rotational speed measuring

A.3 Volumetric Flow measurement

The Krohne Aqualux F is shown in Figure A.3. The instrument gave out a signal from 4 – 10 mA which was converted to a 2 to 10 V signal by a Krohne IFW 300 W signal converter. The signal converter which is shown in Figure A.4 also functioned as a display and controller for the flow meter. With the signal converter the range of the flow meter was set to 0 l/s to 150 l/s.



Figure A.3: Krohne Aquaflux F Electromagnetic Flow Meter



Figure A.4: Krohne IFW 300 W Signal Converter

Appendix B

Calibration

B.1 Torque Calibration

Weight-Weight number	Claimed Weight	Difference	Actual Weight
2kg - 21	2	-0.836 g	1.999164 kg
2kg - 22	2	-0.222 g	1.999778 kg
2kg - 23	2	-0.221 g	1.999779 kg
2kg - 24	2	-2.488 g	1.997512 kg
5kg - 28	5	-1.78 g	4.99822 kg
5kg - 29	5	-0.91 g	4.99909 kg
5kg - 30	5	-0.71 g	4.99929 kg
5kg - 31	5	-0.02 g	4.99998 kg
5kg - 32	5	-1.4 g	4.9986 kg
2kg - 51	2	-0.825 g	1.999175 kg
2kg - 52	2	-1.008 g	1.998992 kg
2kg - 53	2	-0.561 g	1.999439 kg
2kg - 54	2	-0.222 g	1.999778 kg
2kg - 55	2	-0.103 g	1.999897 kg
2kg - 56	2	-0.745 g	1.999255 kg
2kg - 57	2	-0.416 g	1.999584 kg
2kg - 58	2	-0.202 g	1.999798 kg
2kg - 59	2	-1.055 g	1.998945 kg

Table B.1: Calibration of weight used in Torque cell calibration

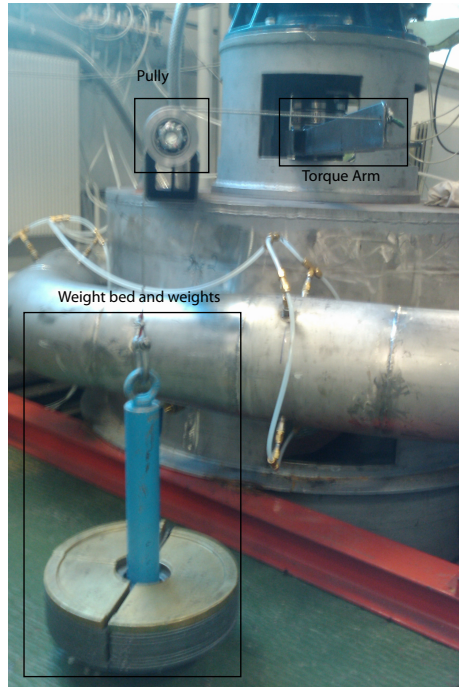
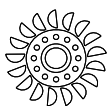


Figure B.1: Torque Calibration Setup

B.2 Calibration of the Volume Flow Meter

During the calibration of the volume flow meter the water was guided into the weighing tank for a set time while the voltage signal from the instrument were recorded. This was done for a number of flow rates to obtain the calibration curve for the range of the volume flow meter. During the calibration the water was flowing from the attic to obtain a constant pressure from the free water surface and therefor a constant volume flow. Volume flow was changed with the electronic valve in front of the weighing tank.

B.2.1 Substitution Calibration Procedure



Doc No: LC-4331-5/6/7	Rev: 0	Date: 2006-03-22	
Prepared by: Jørgen Ramdal	Approved by: Ole G. Dahlhaug	Classification: Open	Page: 1 of 5

Substitution calibration of weighing tank

1 General

This procedure describes how the weighing tank system is calibrated in the Waterpower Laboratory.

1.1 Definitions and abbreviations

W	Mass of weights	[kg]
c	Amplifier reading	[kg]
Δc	Difference in amplifier reading before and after upload of calibrated weights	[kg]
a_0, a_1, a_2, a_3, a_4	Parameters in correction equation	

2 The system

2.1 Description

The Waterpower Laboratory makes use of a weighing tank system for calibration of flow meters. The weighing tank is resting on three load cells (type Hottinger RTNC) connected to an amplifier with display (type Hottinger MGC Plus AB22A). The water is guided into or outside the tank through a pneumatically driven guiding system. The weight displayed on the amplifier has to be corrected, and to find the correction equation, a substitution calibration is performed. A number of calibrated weights are used to find the slope in the range of the tank capacity, from which a calibration equation is found. The weights have been calibrated by Justervesenet (Norwegian Metrology Service).

2.2 Equipment used in calibration

- The laboratory piping- and pump system
- Weighing tank system
 - Hottinger RTNC load cells (Reg.nr. 4331-5/6/7)
 - Hottinger MGC Plus AB22A amplifier (Reg.nr. 2755-9)
 - Capacity appr. 86 metric ton \rightarrow 73 m³ water plus weight of tank and calibrated weights.
- Calibrated weights
 - 5126.075 kg (Calibration document: *LS-Sertifikat for lodder og vekter ved VKL*)

3 Calibration

3.1 Preparations

1. Set up the laboratory piping and pump system so that water is directed to the weighing tank system. It is preferred to use the free water surface reservoir.
2. Make sure nothing disturbs the weighing tank or induces unwanted movements. Remove all shafts connected to the tank, and remove all objects not related to the tank. Inspect the tank pit with a flash light, to make sure it is free of water, and that no object is jammed between the tank and the pit wall.
3. Prepare the laboratory crane for operation.

3.2 Calibration

1. Adjust the pump and valves so that the wanted flow is obtained.
2. Record the time and the weight of the tank.
3. Use the laboratory crane to put the calibrated weights on top of the tank, record the amplifier reading [c] and lift off the calibrated weights again.
4. Set the time on the tilting screen controller computer to a time that gives approximately 5 ton per filling. Tilt the screen to start filling the tank.
5. When the filling has stopped, let the tank stabilize and record the weight of the tank.
6. Repeat steps 3, 4 and 5 until full tank capacity is reached.

4 Computations

The amplifier reading is not correct, and an equation has to be found in order to make sure the correct mass is used in flow calibrations.

A function $W = f(c)$ represents the connection between the amplifier reading [c] and the applied weight on the force transducers. This function is assumed to be a fifth order polynomial.

$$W = f(c) = a_0 \cdot \frac{c^5}{5} + a_1 \cdot \frac{c^4}{4} + a_2 \cdot \frac{c^3}{3} + a_3 \cdot \frac{c^2}{2} + a_4 \cdot c \quad (1)$$

The derivate of this function is found by subtracting the amplifier reading after upload from the amplifier reading before, and divide the weight of the calibrated weights by the product of the subtraction.

$$f'(c) = \frac{W}{\Delta c}$$

This relationship is found for every 5 tons in the whole range of the weighing tank and the data is put into a graph with $f'(c)$ along the y axis and c along the x axis. A fourth order polynomial is found by interpolation through the recorded points, giving the parameters a_0 , a_1 , a_2 , a_3 and a_4 . The final correction equation is found by integrating the fourth order polynomial.

5 Figures

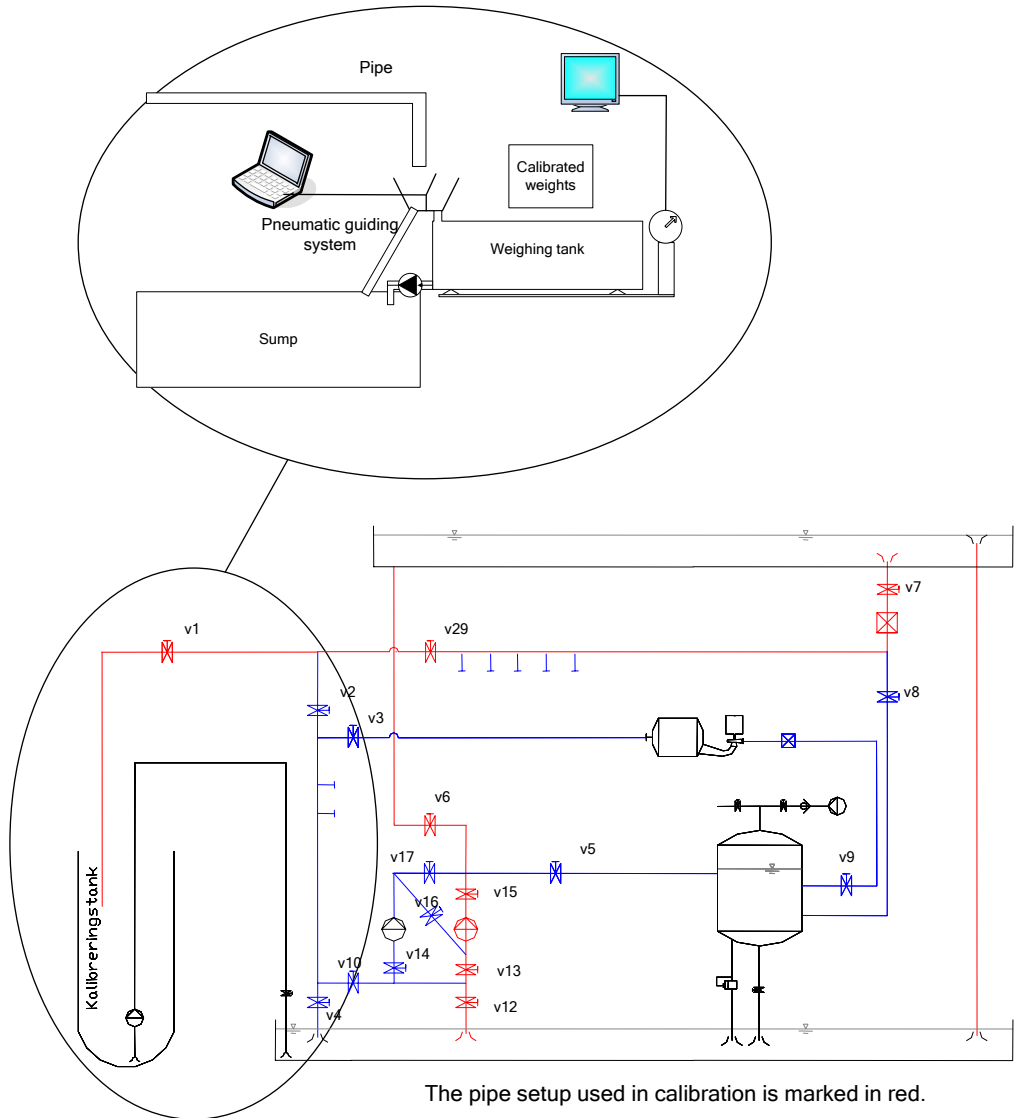


Figure 1: Lab-setup

6 References

- Calibration document for weights at the Waterpower Laboratory issued by Justervesenet (LS-Sertifikat for lodder og vekter ved VKL)
- ISO 4185:1980 Measuring of liquid flow in closed conduits
- Documentation for load cells (Doc IA 4331-5/6/7)
- Documentation for measuring amplifier (Doc IA 2755-9)



WATERPOWER LABORATORY NTNU

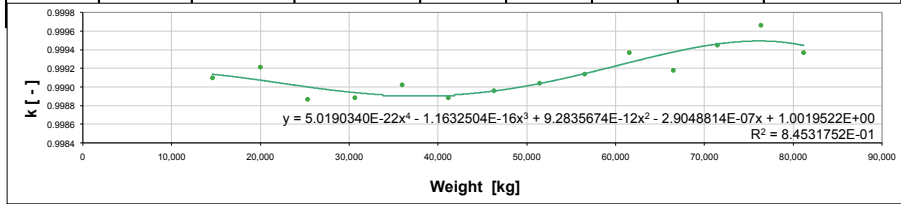
Calibration Sheet

Calibration of weighing tank load cells

Date: 04.02.2010
 Operator: Bjørn W. Solemslie & Lars Erik Klemetsen
 Approved:

Calibrator: 10x500kg weights+hanging fixture/frame. Weight 5126.05 kg. Unit: Weighing tank load cells, reg. nr. 4331-5/6/7

Time	Manual Observation	Manual Observation	Displayed load increase	$k = \frac{W_L}{\Delta W}$	Weight midpoint	Estimated correction factor	Difference in real k and estimated k	
	Weights off [kg]	Weights on [kg]					ΔW [kg]	k [-]
	12017.7	17148.4	5130.7	0.9991	14583.1	0.99935	0.00025	0.025
	17406.2	22536.3	5130.1	0.9992	19971.3	0.99901	-0.00021	0.021
	22758.3	27890.2	5131.9	0.9989	25324.3	0.99887	0.00000	0.000
	28075.7	33207.5	5131.8	0.9989	30641.6	0.99886	-0.00002	0.002
	33362.6	38493.7	5131.1	0.9990	35928.2	0.99894	-0.00008	0.008
	38565.8	43697.6	5131.8	0.9989	41131.7	0.99905	0.00017	0.017
	43732.3	48863.7	5131.4	0.9990	46298.0	0.99916	0.00020	0.020
	48867.8	53998.8	5131	0.9990	51433.3	0.99926	0.00021	0.022
	53943	59073.5	5130.5	0.9991	56508.3	0.99931	0.00017	0.017
	58974.2	64103.5	5129.3	0.9994	61538.9	0.99932	-0.00005	0.005
	63942.2	69072.5	5130.3	0.9992	66507.4	0.99930	0.00012	0.012
	68867.6	73996.5	5128.9	0.9994	71432.1	0.99924	-0.00021	0.021
	73764.8	78892.6	5127.8	0.9997	76328.7	0.99917	-0.00049	0.049
	78595.8	83725.1	5129.3	0.9994	81160.5	0.99912	-0.00026	0.026



Calibration constants	Order	Value
a_5	5	1.00E-22
a_4	4	-2.91E-17
a_3	3	3.09E-12
a_2	2	-1.45E-07
a_1	1	1.00E+00

Appendix C

Distributors After Opptimization

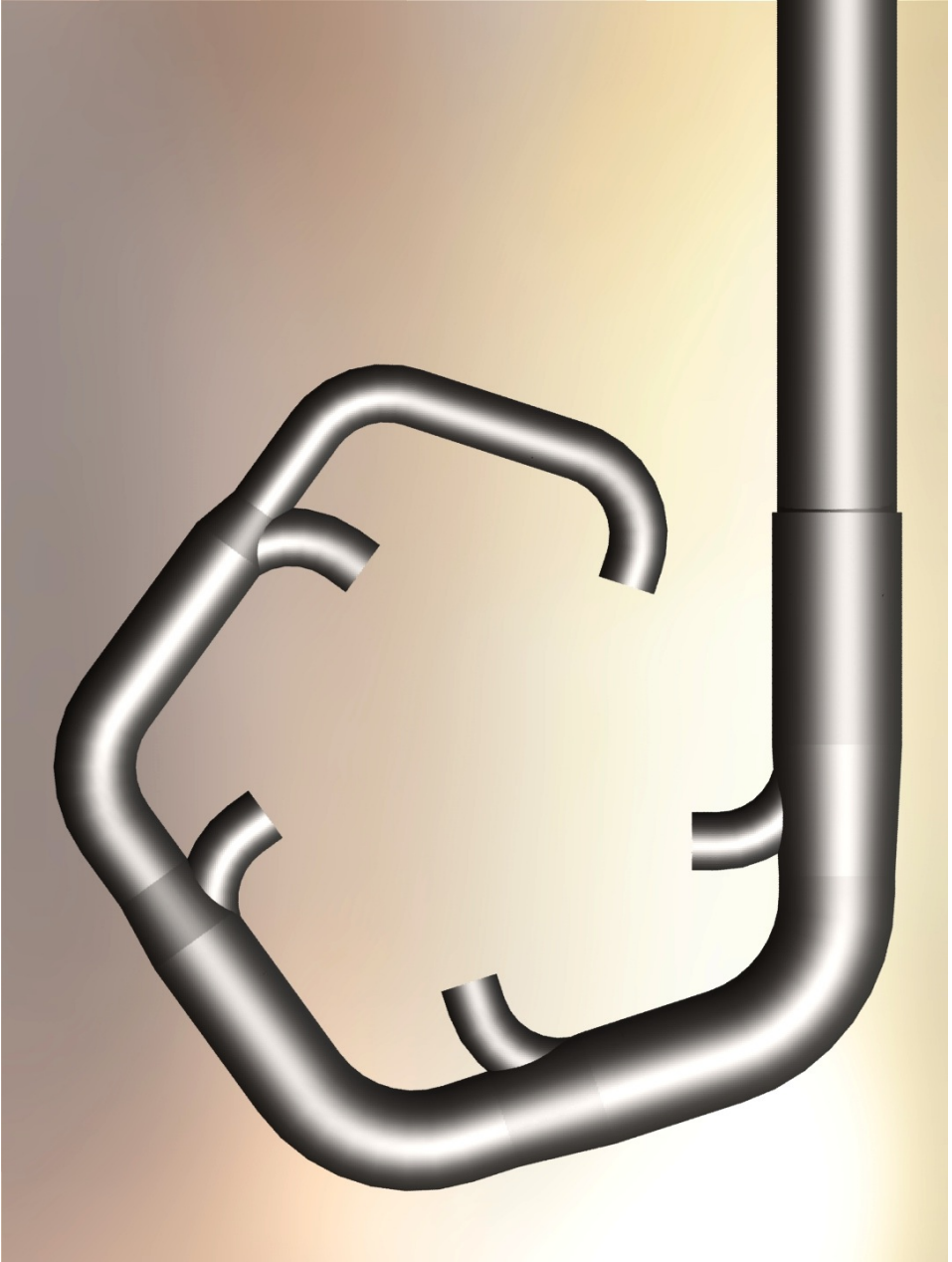


Figure C.1: The throat optimized distributor

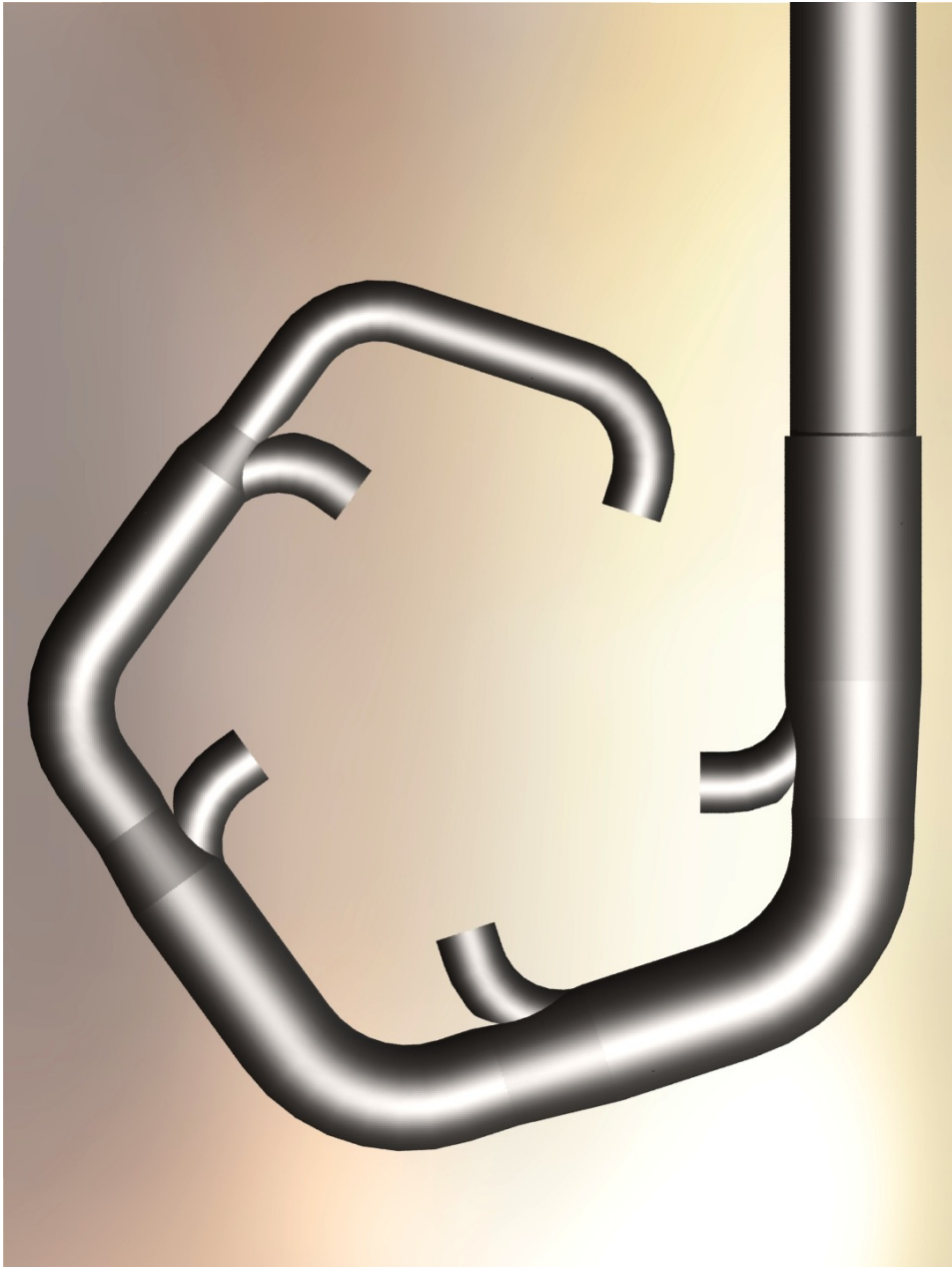


Figure C.2: The throat optimized distributor with primitive guide vanes



(a)



(b)

Figure C.3: The throat optimized distributor with the throat mimicking that at nozzle 1 (a) and nozzle 4 (b)

Appendix D

Uncertainty Analysis

The error in a measurement is defined by the difference between the measured value and the actual value of the physical property in question. This error is generally not known, but it can be estimated by the use of statistical methods discussed in Appendix D. From the statistical methods it is possible to find a confidence interval where the actual value of the physical property will lie within a certain probability. This probability is chosen, but the industry uses 95% as the standard probability of the confidence interval.

In this report three types of errors will be considered

- Spurious errors
- Systematic errors
- Random errors

Spurious Errors may be caused by human error or failure in the measuring instrument. These errors should usually be recognized when measurements are analyzed and the whole series of measurements may have to be disregarded. Sometimes these errors only occur in some of the measurements and is observed as out of line with the rest of the measurement series. These points are so called *outliers* and one can for

example reject the ones that are out of line with the rest by more than two or three standard deviations. A number of statistical methods for rejecting such outlying measurements are available, but the one normally used is a modified Thompson τ technique [14, Chapter 6.5]

Systematic Errors may have their origin in poorly calibrated instruments, hysteresis or lack of linearity in the instrument. These phenomenas and others are described in Appendix D.1. To find the systematic errors one must analyze the processes leading to the measured value, including the calibration method and the random errors during the calibration, among others. If the error limits of the instrument is known from the producer one may use the interval between them as the systematic uncertainty with a confidence level of 95% [4, Chapter 3.9]. However, this uncertainty will usually be much larger than the systematic error one would find through a thorough calibration.

Random Errors are caused by small independent influences which prevent the instrument from delivering the same output when measuring the same value of the physical property. This is directly connected to the repeatability of the instrument as discussed in Appendix D.2. In addition, the random errors are dependent on the variations in the system that the physical quantity is measured in. The deviation of the measurement from the mean follows stochastic variability and therefore one may assume that they approach a normal (gaussian) distribution when the number of measurements increase [4, Chapter 3.9]. This indicates that the random error will decrease with the number of measurements for a specific measurement point when using their mean value during the experiment. If the number of measurements were infinite the distribution could be described by a *Normal Distribution*, but when the number of samples are lower one may describe the distribution by a *Student-t distribution* [14, Chapter 7.3]. This method of describing the distribution around the mean takes into account the increase of the standard deviation when the number of measurements decrease.

The confidence interval around the mean of the measurements, \bar{X} is shown in Equation (D.1)

$$\bar{X} \pm \frac{t_{\alpha/2} \cdot S_X}{\sqrt{N}} \quad (\text{D.1})$$

where N is the number of samples and $t_{\alpha/2}$ for a t-value for the Student-t distribution with the confidence level $1 - \alpha$. The Student-t distribution will approach a normal distribution when using the mean value of an increasing number of measurements.

D.1 Systematic errors

As stated above systematic errors include the uncertainties from the calibration and some specific uncertainties of the instrument. During a calibration it is important to get enough measurement points along the calibration curve to ensure that the different uncertainties of the instrument are accounted for. The main sources of uncertainty for an instrument are

- Hysteresis
- Linearity
- Accuracy
- Zero offset
- Drift

Hysteresis is the phenomenon where the instrument give different output for the same input value, load, when it prior to the measurement have been exposed to a higher or lower load. Hysteresis can be taken into account when calibrating by increasing the load to the maximum value and then decreasing the load back to zero through the same input values. This phenomenon is shown in Figure D.1.

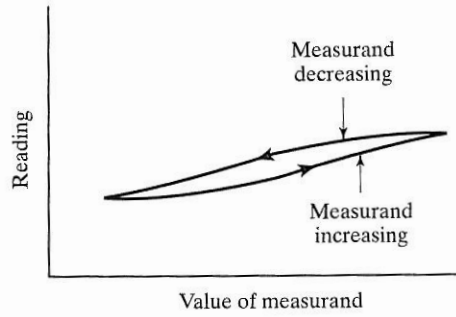


Figure D.1: Effect of hysteresis on instrument reading [14, Figure 2.5]

Linearity is an indicator of if the instruments ability to linearly change the output with the input. Linearity can be taken into account while calibrating by having enough measuring points so that a lack of linearity is evident when when a linear approximation is produced. Figure D.2 shows how this phenomenon may occur.

Zero offset is the phenomenon where the output of the instrument when it is exposed no load is not equal to zero. The manufacturer's specifications usually assume that the zero point has been adjusted properly, but may also specify a maximum expected error called *zero balance*. The zero offset of an instrument should be checked prior to the calibration or use of the instrument as this can be used as an indication of instrument malfunction. Figure D.2 shows how the zero offset affects the output curve of an instrument.

D.2 Random errors

The random errors of a measurement mainly originate from the repeatability of the instrument. This is the phenomenon where the instrument gives different output for a constant input, the fluctuation of the output is caused by small, independent variations within the instrument. However, a part of

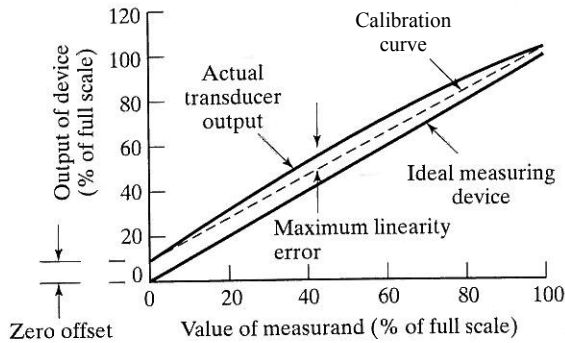


Figure D.2: Example of nonlinearity and zero offset[14, Figure 2.6]

the random error is also caused by small, independent variations in external properties such as temperature and atmospheric pressure.

Random errors may be described with a statistical distribution when the number of measurements is large. When investigating the error in the measurement of a single, constant physical property one may describe the distribution of the measurements around the mean as a Student-t distribution. This distribution becomes a normal distribution when the number of measurement points increases towards infinity. The student-t distribution is similar to the normal distribution in shape, but the ends are spread more when the number of samples are low. Figure D.3(a) shows how the distribution changes with the number of degrees of freedom, ν , increases. The number of degrees of freedom is $N - 2$, where N is the number of measurements in the measurement point.

Graphs such as the ones shown in Figure D.3 are called *Probability density graphs* and the area under an interval is the same as the probability of a random variable being located in the interval. The confidence interval is shown in Figure D.3(b) and the area, and therefore the probability, under

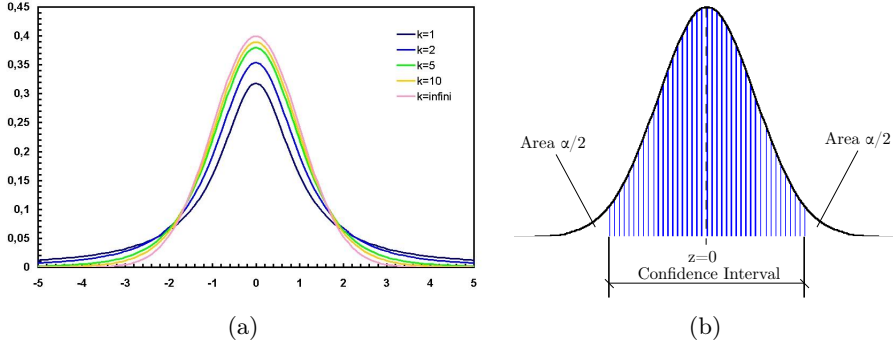


Figure D.3: A Student-t distribution with different number of measurement points (a) and a Normal distribution with confidence interval (b)

the graph outside the confidence interval is the same as α . The expression for the confidence interval of the mean of a measurement with a $1 - \alpha$ confidence is shown in Equation (D.2).

$$P\left(\bar{X} - t_{\alpha/2} \cdot \frac{S_X}{\sqrt{N}} \leq \mu \leq \bar{X} + t_{\alpha/2} \cdot \frac{S_X}{\sqrt{N}}\right) = 1 - \alpha \quad (\text{D.2})$$

$$S_X = \sqrt{\frac{1}{N-1} \sum_{i=1}^N (x_i - \bar{X})^2}$$

D.3 Method for Finding Regression Errors

When a linear approximation is produced as a calibration curve it includes an error due to the assumption that all the measurements should be on the curve. The error originates from the variation of the measurements in each measurement point as well as the spread of the measurement points in vertical and horizontal direction. Some important indicators for the variation around the regression line are listed below.

$$\begin{aligned}
 S_{XX} &= \sum_{i=1}^N (x_i - \bar{X})^2 \\
 S_{YY} &= \sum_{i=1}^N (y_i - \bar{Y})^2 \\
 S_{XY} &= \sum_{i=1}^N (x_i - \bar{X})(y_i - \bar{Y})
 \end{aligned}$$

S_{xx} and S_{yy} reflect the variation of x and y individually around the regression line. S_{xy} reflect the combined variation of x and y around the regression line. Equation (D.3) show the expression for the *sum of squares of the errors about the regression line* and is denoted SSE. Equation (D.4) shows an unbiased estimate of the variance of the regression line produced with the SSE [13, Chapter 11.3 and 11.4].

$$SSE = S_{yy} - bS_{xy} \quad (\text{D.3})$$

$$s^2 = \frac{SSE}{N - 2} \quad (\text{D.4})$$

The regression curve can be viewed as an estimate of the mean response, Y_0 , of an input x_0 . The expression for the confidence interval of the mean response of a given input around the regression line is shown in Equation (D.5) [13, Chapter 1.6].

$$\hat{Y}_o - t_{\alpha/2} \cdot s \sqrt{\frac{1}{n} + \frac{(x_0 - \bar{X})^2}{S_{xx}}} \leq \mu_{Y|x_0} \leq \hat{Y}_o + t_{\alpha/2} \cdot s \sqrt{\frac{1}{n} + \frac{(x_0 - \bar{X})^2}{S_{xx}}} \quad (\text{D.5})$$

From Equation (D.5) it is evident that the statistical bounds around the linear approximation is as shown below.

$$f_{Y|x_0} = \pm t_{\alpha/2} \cdot s \sqrt{\frac{1}{n} + \frac{(x_0 - \bar{X})^2}{S_{xx}}} \quad (\text{D.6})$$

To produce the confidence interval along the whole linear approximation one must calculate this uncertainty for each y-value with the corresponding x-value.

D.4 Propagation of uncertainties

If a function, Y , is defined as a function of x_1, x_2, \dots, x_n independent measured variables and each measured variable has a absolute deviation from the actual physical properties $\Delta x_1, \Delta x_2, \dots, \Delta x_n$. All the deviations in the physical properties will result in a absolute deviation in the function $Y = Y \pm \Delta F$ so that the expression for the total value of Y as shown in (D.7).

$$Y = Y \pm \Delta Y = y(x_1 \pm \Delta x_1, x_2 \pm \Delta x_2, \dots, x_n \pm \Delta x_n) \quad (\text{D.7})$$

The expression for the total value of Y can be expanded as a *Taylor expansion* as shown in Equation (D.8) where the contribution from the terms of a higher order than *one* is neglected.

$$y(x_1 \pm \Delta x_1, x_2 \pm \Delta x_2, \dots, x_n \pm \Delta x_n) = y(x_1, x_2, \dots, x_n) \pm \frac{\delta y}{\delta x_1} \Delta x_1 \pm \frac{\delta y}{\delta x_2} \Delta x_2 \pm \dots \pm \frac{\delta y}{\delta x_n} \Delta x_n \quad (\text{D.8})$$

The assumption that the contribution from the terms of a higher order than *one* can be neglected can be checked by Equation (D.9)

$$\left(\frac{\delta y}{\delta x_i} \right) \Delta x_i \gg \frac{1}{2} \left(\frac{\partial^2 y}{\partial x_i^2} \right) (\Delta x_i)^2 \Rightarrow \frac{2 \left(\frac{\delta y}{\delta x_i} \right)}{\left(\frac{\partial^2 y}{\partial x_i^2} \right)} \gg \Delta x_i \quad (\text{D.9})$$

Equation (D.10) is derived by combining Equations (D.7) and (D.8).

$$Y \pm \Delta Y = y(x_1, x_2, \dots, x_n) \pm \frac{\delta y}{\delta x_1} \Delta x_1 \pm \frac{\delta y}{\delta x_2} \Delta x_2 \pm \dots \pm \frac{\delta y}{\delta x_n} \Delta x_n \quad (\text{D.10})$$

Equation (D.11) is derived by subtracting $Y = Y \pm \Delta Y$ from Equation (D.10) and express the maximum absolute error in Y from the individual errors in the measured variables.

$$|\Delta Y| = \left| \frac{\delta y}{\delta x_1} \Delta x_1 \right| + \left| \frac{\delta y}{\delta x_2} \Delta x_2 \right| + \dots + \left| \frac{\delta y}{\delta x_n} \Delta x_n \right| \quad (\text{D.11})$$

Until now all the individual errors are assumed to change Y in the same direction with maximum force. By treating the individual errors as statistical bounds for the individual variables the probable total change in Y caused by the individual errors can be expressed by the *Root-sum-square* method as shown in Equation (D.12).

$$\Delta Y = \pm \sqrt{\left(\frac{\delta y}{\delta x_1} \Delta x_1 \right)^2 + \left(\frac{\delta y}{\delta x_2} \Delta x_2 \right)^2 + \dots + \left(\frac{\delta y}{\delta x_n} \Delta x_n \right)^2} \quad (\text{D.12})$$

D.5 Errors in the Calibration

Here the errors in the calibration of the different instruments are described in more detail.

D.5.1 Errors in the Calibration of the Volume Flow Meter

- $f_{Q_{\Delta W}}$, the systematic uncertainty of the weight cells and their calibration has been found to be $\pm 0.05043\%$ by Pål-Tore Storli in [8].
- f_{Q_t} , the systematic uncertainty of time measurements may be ignored as the relative error is at most $\pm 0.0005\%$ for a period of 200 seconds.

- $f_{Q_{divider}}$, the systematic uncertainty of the divider was found to be $\pm 0.072611\%$ at 50 l/s by Pål-Tore Storli in [8] and is assumed to be a good estimate for other flow rates.
- f_{Q_ρ} , the systematic uncertainty in finding the density of water may be assumed to be in the order of 0.01% by IEC [4].

The combination of the above listed uncertainties with the RSS-method result in

$$f_{Q_a} = \pm \sqrt{(f_{Q_{\Delta W}})^2 + (f_{Q_t})^2 + (f_{Q_{divider}})^2 + (f_{Q_\rho})^2} = \pm 0.0889\%$$

f_{Q_b} , the random error in the weighing tank system may be divided into the following:

- $(f_{Q_{\Delta W}})_r$, the random uncertainty of the weight cells and their calibration was found to be $\pm 0.00072\%$ by Pål-Tore Storli in [8].
- $(f_{Q_{divider}})_r$, the random error of the divider may be found using the procedure in [4, 6.2.2.2 p.13]. Pål-Tore Storli found it to be $\pm 0.050339\%$ for 50 l/s in [8] and this was assumed to be valid for the calibration done for these experiments.
- $(f_{Q_\rho})_r$, the random error in finding the density of water may be neglected compared to the other uncertainties.

Combining the above listed uncertainties the total relative random uncertainty in the weighing tank system is found to be

$$f_{Q_b} = \pm \sqrt{(f_{Q_{\Delta Q}})^2 + (f_{Q_{divider}})^2 + (f_{Q_\rho})^2} = \pm 0.0503\%$$

f_{Q_c} and f_{Q_d} , the random and systematic uncertainties in the instrument are included in the regression error $f_{Q_{regression}}$.

f_{Q_e} , physical phenomena and external influences for the calibration are assumed to be negligible since the calibration and the tests are done under

the same conditions. This is also due to the fact that the data sheet of the volume flow meter states that the instrument is unaffected by the density, viscosity, temperature and pressure of the fluid being measured.

f_{Q_f} consist of uncertainties in calculating properties or using international standard data, i.e such as the error in calculating ρ_{water} from standard formulas or finding g in tables. These errors are assumed to be negligible.

D.5.2 Errors in the Calibration of the Torque Transducer

- f_{τ_W} , the systematic uncertainty in the weights used for the calibration are taken into account by using the calibrated weight instead of the claimed weight of the weights. The weight bed has an uncertainty of ± 0.5 g which gives a relative uncertainty of $f_{\tau_W} = 0.01\%$. Information on weight and a picture of the calibration setup is found in Appendix B.1.
- $f_{\tau_{arm}}$, the systematic uncertainty in the length of the arm. The length was measured to 1.10515 m and the uncertainty of both the ruler and the sliding gauge assumed to be 0.0001 m. By combining the uncertainties one obtains $f_{\tau_{arm}} = \pm 0.013\%$
- f_{τ_c} and f_{τ_d} , the systematic and random uncertainty in the instrument are included in $f_{\tau_{regression}}$ as for the volume flow meter and the differential pressure transmitter. The maximum uncertainty in the regression line was $max(f_{\tau_{regression}}) = \pm 0.830566\%$ for a torque of 51.9 Nm.

D.6 Errors in the measurements

In this chapter the errors in the measurements of the different physical quantities are presented.

D.6.1 Errors in the Volume Flow Measurements

- $max(f_{Q_{cal}}) = \pm 0.102\%$
- f_{Q_h} is caused by drifting of the output signal over time. This can be reduced by calibrating often, or check the calibration after tests. Due to little time and the work required to check the calibration this was not done. It is still assumed to be negligible based on historical data for calibration of similar volume flow meters. These indicate that this type of volume flow meter is not prudent to have significant drifting.
- f_{Q_j} is the same type of uncertainty as f_{p_f} described in Chapter 7.3 and can be ignored.
- $f_{Q_{k_s}}$ and f_{Q_r} are the same as f_{p_e} described in Chapter 7.3. These uncertainties may be ignored if the conditions during the test were the same as during the calibration.
- $max(f_{Q_l}) = \pm 0.1345\%$

D.6.2 Errors in the Temperature Measurements

- $max(f_{\tau_{cal}}) = \pm 0.8307\%$
- f_{τ_h} is caused by drifting of the output signal over time. This can be reduced by calibrating often, or check the calibration after tests. Due to lack of time and the test rig being dismantled shortly after the tests were completed this was not done. The uncertainty is still assumed to be negligible based on the lack of drift between the calibration done in this thesis and that done in [12].
- f_{τ_j} is the same type of uncertainty as f_{p_f} described in Chapter 7.3 and can be ignored.
- $f_{\tau_{k_s}}$ and f_{τ_r} are the same as f_{p_e} described in Chapter 7.3. These uncertainties may be ignored if the conditions during the test were the same as during the calibration.

- $max(f_{\tau_l}) = \pm 2.97 \cdot 10^{-5}\%$

D.6.3 Errors in the Torque Measurements

- $max(f_{T_{cal}}) = \pm 0.01\%$
- f_{T_h} is caused by drifting of the output signal over time. This can be reduced by calibrating often, or check the calibration after tests. Due to the fact that the calibration from the manufacturer was assumed to be correct this uncertainty is ignored.
- f_{T_j} is the same type of uncertainty as f_{p_f} described in Chapter 7.3 and can be ignored.
- $f_{T_{k_s}}$ and f_{T_r} are the same as f_{p_e} described in Chapter 7.3. These uncertainties may be ignored if the conditions during the test were the same as during the calibration.
- $max(f_{T_l}) = \pm 6.8 \cdot 10^{-5}\%$

Appendix E

Frequency and Nozzle House Failure

E.1 Frequency Converter Failure

After some test series were conducted one experienced a failure in the frequency converter with unknown cause. After a technician changed some of the power electronic circuits the frequency converter was assumed to be functioning again. This assumption was disproved during the first start up when the fuse for the control voltage in the frequency converter blew and lead to a shut down. This caused the generator to drop and resulted in the turbines going towards runaway speed. The emergency shutdown button was activated quickly after the generator dropped and no damage was made to the generator. The technician returned and replaced the blown fuses and the frequency converter functioned without errors for the rest of the experiments. This failure led to a total total of 5 days of down time.

E.2 Nozzle Housing Failure and Repair

Several weeks after the frequency converter failed, one of the nozzles failed from what is believed to be fatigue. This affected the threads for the screws

holding a metal ring on the front of the nozzle that may be seen in Figure E.1. The fatigue failure was believed to have been caused by vibrations in the piping system originating from the pump as a reaction to the low flow rate at low nozzle openings. It is believed that nozzle 3 was the first nozzle to fail and that the ring was blown through the buckets of the turbine, hitting nozzle 5 and causing the same failure to happen there. The ring from nozzle 5 followed a similar path through the buckets, hitting nozzle 1 but not causing the same failure. As the ring is the cover for the nozzle opening and both the failed nozzles were closed, the volume flow increased severely. This again led to the torque on the generator increasing significantly over a very short period of time. After the system was shut down it was found that the generator had not suffered any damages from the increased torque. Since the rings destroyed some of the buckets on the turbine it became unbalanced, this did not cause any damages on the generator, shaft or bearings. This concluded after measuring the shaft on the turbine side for eccentricity.

As shown in Figure E.1 the holes for the screws holding the ring in place were destroyed during this failure and repairs were needed on all the nozzles since it was assumed that the same failure could happen to the remaining 3 nozzles. All the nozzles and the turbine were taken off the distributor to be repaired. The number of screws holding the rings in place on the nozzles were doubled to better secure the ring as shown on Figure E.2. The thread in the screw holes on the nozzles that failed were nearly completely removed so all the holes were rethreaded. The rethreading was done with a thread profile with bigger diameter and deeper threads to increase the contact area of the screw. Adhesives were used on both the thread and on the contact surface between nozzle housing and ring, Figure E.2(b) shows a nozzle housing before and after the repair. The failure led to a total of 3 weeks of down time.



(a)



(b)

Figure E.1: Nozzle 3 (a) and nozzle 5 (b) after the failure

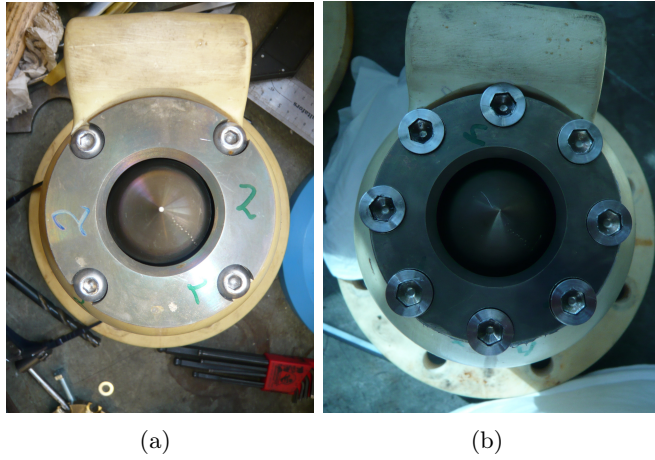


Figure E.2: The front of the nozzle housing before (a) and after (b) the improvements



Figure E.3: The ring before and after the improvements



Figure E.4: The 4 buckets that were broken off the turbine by the rings



Figure E.5: The turbine in place in the turbine housing after the failure



Figure E.6: The turbine after it was taken out

Appendix F

Results

F.1 Experimental results

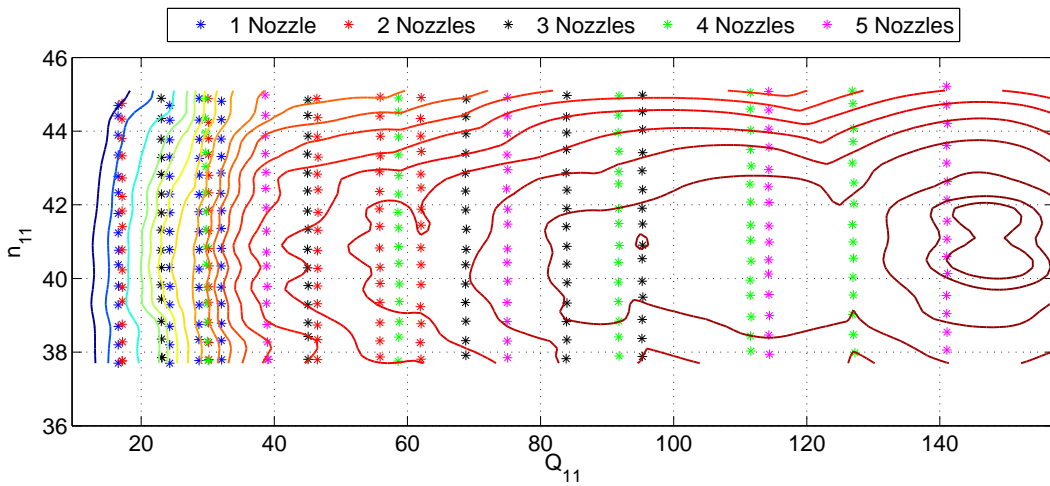


Figure F.1: Full Hill diagram with measurement points indicated

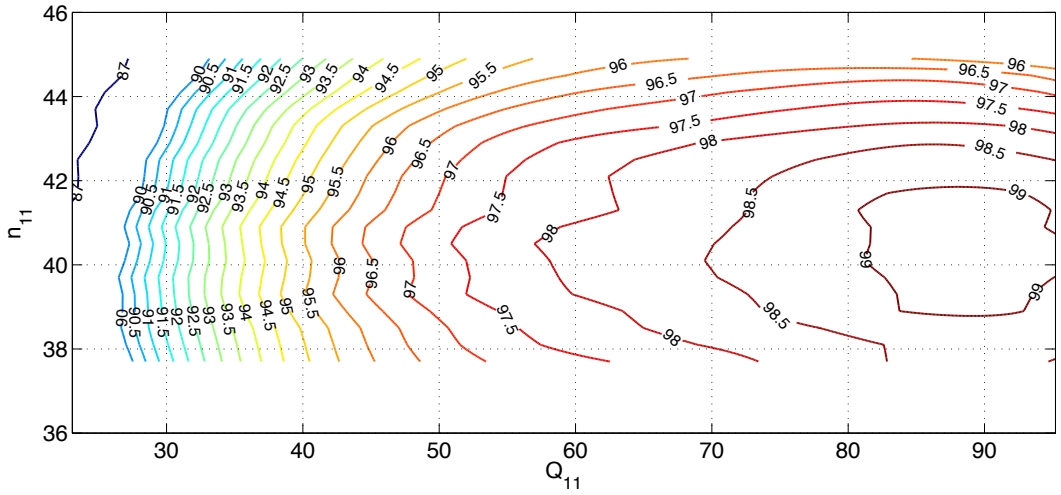


Figure F.2: Hill diagram for 3 nozzle

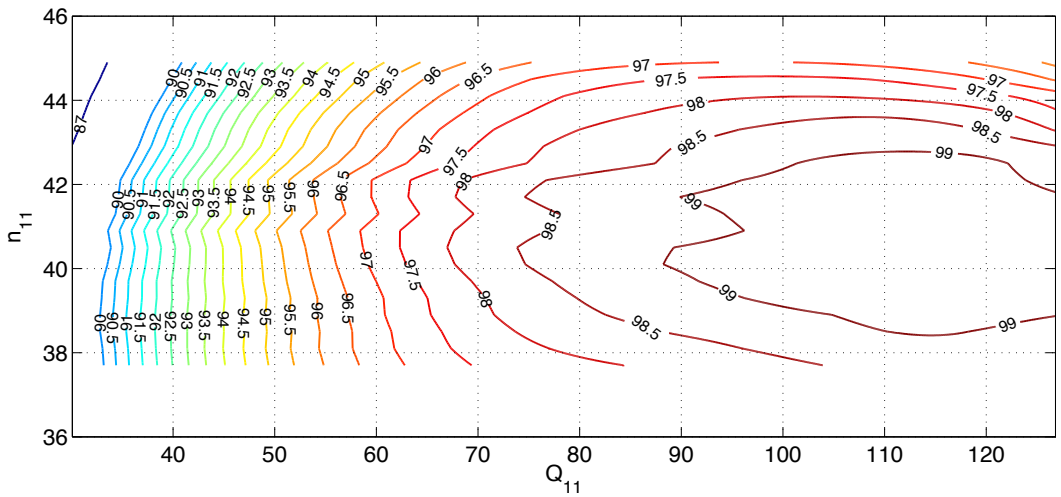


Figure F.3: Hill diagram for 4 nozzles

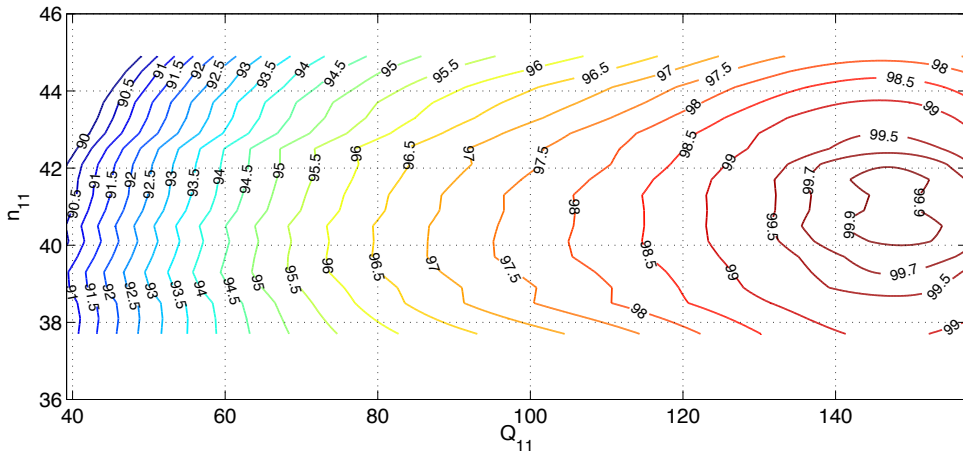
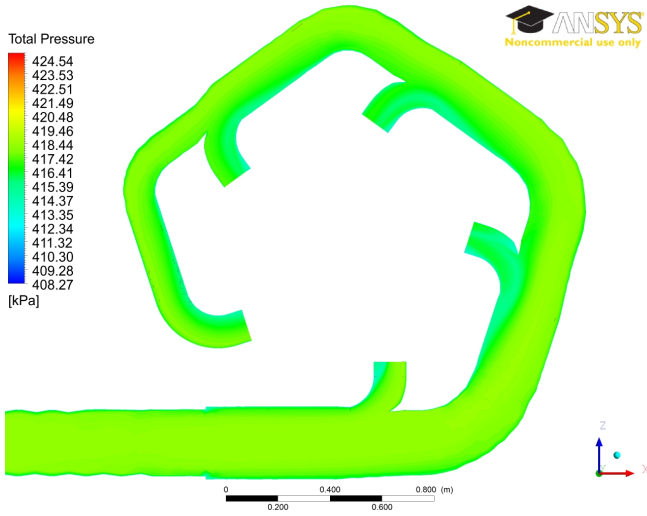
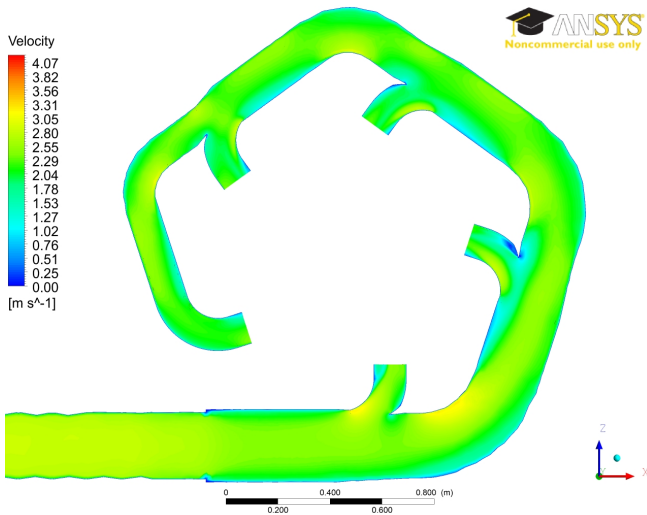


Figure F.4: Hill diagram for 5 nozzles

F.2 Simulation results



(a) Total pressure contour



(b) Velocity contour

Figure F.5: Total pressure (a) and velocity (b) contours on the throat optimized distributor with primitive guide vanes

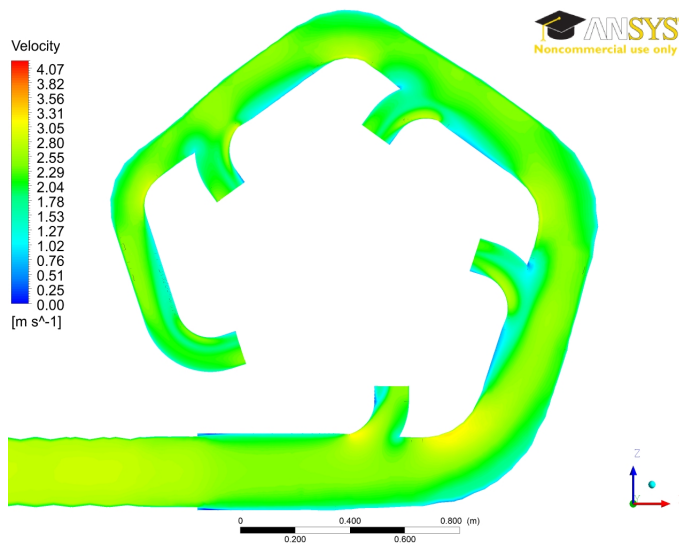
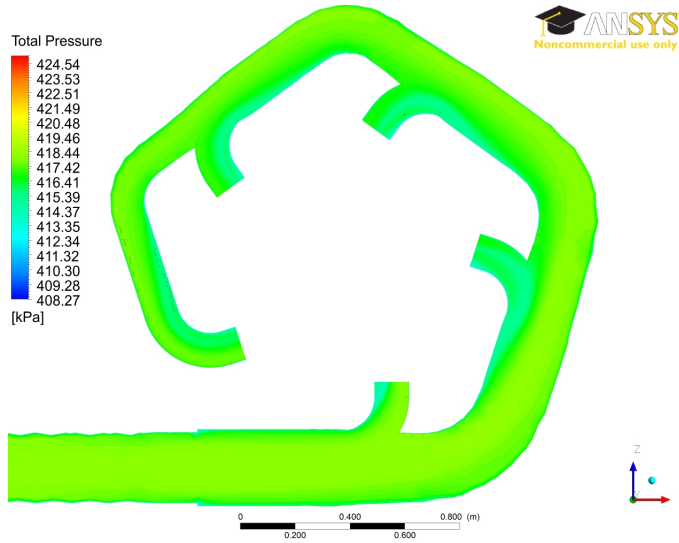
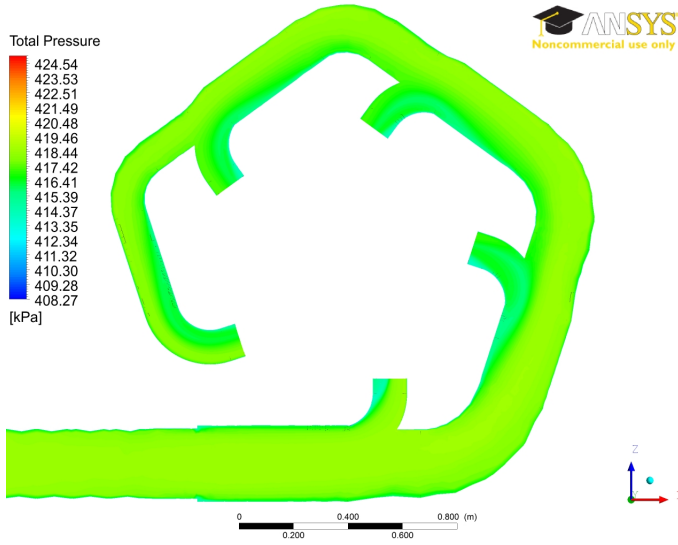
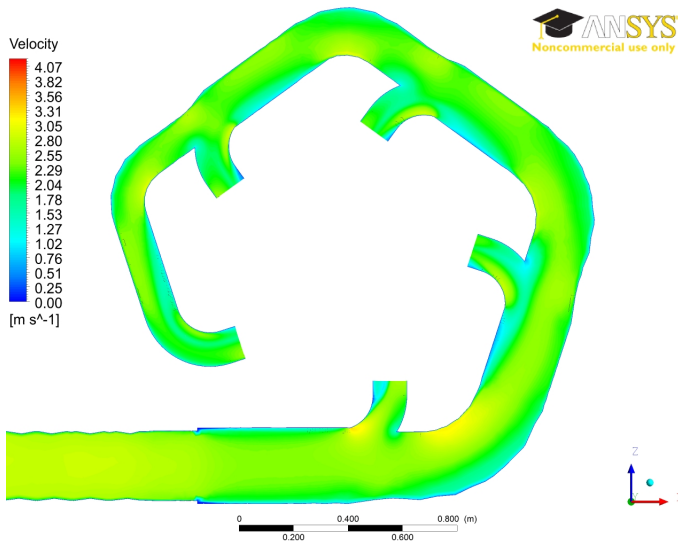


Figure F.6: Total pressure (a) and velocity (b) contours on the throat optimized distributor with the throat mimicking that at nozzle 1.



(a) Total pressure contour



(b) Velocity contour

Figure F.7: Total pressure (a) and velocity (b) contours on the throat optimized distributor with the throat mimicking that at nozzle 4.

Appendix G

Matlab Code

G.1 Matlab Code for Importing Data

134

```
%%----- Importing data from a output file ----- %  
%  
[pathname] = uigetdir('Choose folder with data'); % Input of Folder %  
dyse=input('How many nozzles? \n'); % Input numer of nozzles %  
aapning=input('Opening? \n'); % Input nozzle opening %  
f=3000; % Logging frequency %  
s=3000; % Number of samples %  
%  
%%----- Discriminates between the first 3 series due to short n_11 span ----- %  
if dyse==1 && aapning≤60 %  
    L1=5; %  
    L2=15; %  
    k=4; %  
else %  
    L1=1; %  
    L2=17; %  
    k=0; %  
end %  
%%----- Discriminates for series where Q is measured in l/s and m^3/s ----- %  
if dyse==1 && aapning≤80 %  
    QL=1000; %  
elseif dyse==1 && aapning==80 %  
    QL=1; %  
else %  
    QL=1000 %  
end %  
%%----- Loop through all measurement points ----- %  
for v=L1:L2 %
```

APPENDIX G. MATLAB CODE


```

%% ----- Calculates mean of raw data ----- %%
data.dp.gjn(r,q,v)=mean(temp3(:,1)); % Finds and saves mean dp %
data.Q.gjn(r,q,v)=mean(temp3(:,2)); % Finds and saves mean Q %
data.n.gjn(r,q,v)=mean(temp3(:,3)); % Finds and saves mean n %
data.M.gjn(r,q,v)=mean(temp3(:,4)); % Finds and saves mean Torque %
data.T.gjn(r,q,v)=mean(temp3(:,5)); % Finds and saves mean T %
data.p_a.gjn(r,q,v)=mean(temp3(:,6)); % Finds and saves mean p_a %
data.H.gjn(r,q,v)=mean(temp3(:,7)); % Finds and saves mean H %
data.He.gjn(r,q,v)=mean(temp3(:,8)); % Finds and saves mean He %
data.etta.gjn(r,q,v)=mean(temp3(:,9)); % Finds and saves mean etta %
data.rho.gjn(r,q,v)=mean(temp3(:,10)); % Finds and saves mean rho %
data.q11.gjn(r,q,v)=mean(temp3(:,11))*QL; % Finds and saves mean q_11 %
data.n11.gjn(r,q,v)=mean(temp3(:,12)); % Finds and saves mean n_11 %
data.N.gjn(r,q,v)=mean(temp3(:,13)); % Finds and saves mean N %
data.P.gjn(r,q,v)=mean(temp3(:,14)); % Finds and saves mean P %
%%
%% ----- Adds NaN to points without measurements from small n_11 span ----- %%
if L1==5 % %
    data.dp.gjn(r,q,1:4)=NaN; data.dp.gjn(r,q,16:17)=NaN; % %
    data.Q.gjn(r,q,1:4)=NaN; data.Q.gjn(r,q,16:17)=NaN; % %
    data.n.gjn(r,q,1:4)=NaN; data.n.gjn(r,q,16:17)=NaN; % %
    data.M.gjn(r,q,1:4)=NaN; data.M.gjn(r,q,16:17)=NaN; % %
    data.T.gjn(r,q,1:4)=NaN; data.T.gjn(r,q,16:17)=NaN; % %
    data.p_a.gjn(r,q,1:4)=NaN; data.p_a.gjn(r,q,16:17)=NaN; % %
    data.H.gjn(r,q,1:4)=NaN; data.H.gjn(r,q,16:17)=NaN; % %
    data.He.gjn(r,q,1:4)=NaN; data.He.gjn(r,q,16:17)=NaN; % %
    data.etta.gjn(r,q,1:4)=NaN; data.etta.gjn(r,q,16:17)=NaN; % %
    data.rho.gjn(r,q,1:4)=NaN; data.rho.gjn(r,q,16:17)=NaN; % %
    data.q11.gjn(r,q,1:4)=NaN; data.q11.gjn(r,q,16:17)=NaN; % %
    data.n11.gjn(r,q,1:4)=NaN; data.n11.gjn(r,q,16:17)=NaN; % %
    data.N.gjn(r,q,1:4)=NaN; data.N.gjn(r,q,16:17)=NaN; % %
    data.P.gjn(r,q,1:4)=NaN; data.P.gjn(r,q,16:17)=NaN; % %

```

```

end
%%-----
[X,S,e]=tilf_err(r,q,v,data,raa);           % Finds random uncertainty
a1=[{'dp'},{'Q'},{'n'},{'M'},{'T'},{'p_a'}]; % Name vector for uncertainty
%%----- Loop to save calculated random uncertainty -----
for i=1:6
    eval(char(strcat('data.',a1(i),...
        '.err.X(r,q,v)=X(i);')))           % Stores dp uncertainty

    eval(char(strcat('data.',a1(i),...
        '.err.S(r,q,v)=S(i);')))           % Stores dp uncertainty

    eval(char(strcat('data.',a1(i),...
        '.err.e_t(r,q,v)=e(i);')))         % Stores dp uncertainty

    eval(char(strcat('data.',a1(i),...
        '.err.f_t(r,q,v)=e(i)/data.',...
        a1(i),'.gjn(r,q,v);')))           % Stores dp uncertainty
end
%%-----

end
%%-----
clear o temp serie fil filename...
    pathname l v w a1 a2 temp2...
    temp3 s serie L l2 f b2 b...
    p_atm LE aapning dyse q r...
    raa X S e i L1 L2 QL                 % Clears temporary data
%-----

```

G.2 Matlab Code for Creating Hill-Diagram

138

```

%%----- SCRIPT FOR MAKEING HILL-DIAGRAM -----%%
L={1:5 6:10 11:14}; % POSITIONS FOR DIFFERENT OPENINGS %
%% ----- SURFACE FITTING HILL FOR DIFFERENT NOZZLE OPENINGS -----%%
for i=1:ceil(length(data.q11_1(:,1))/5) % VARYING OPENING FOR 1 TO 5 NOZZLES %
    Q=[max(ceil(data.q11_1(L{i}(1),:)*10)\10)...%| %
        mean(data.q11_1(L{i}(2:... %|ROUNDS VOLUME FLOW %
            length(L{i})-1),:)'min... %|FOR SPECIFIC NOZZLE CONF. %
            (floor(data.q11_1(L{i)... %| %
                (length(L{i})),:)*10)/10)]; %| %
    q_min=min(Q); % FINDS MINIMUM Q_11 %
    q_max=max(Q); % FINDS MAXIMUM Q_11 %
    q11=min(Q):0.1:max(Q); % Q_11 SPAN WITH HIGHER RESOLUTION %
    n11=37.1:0.1:45; % N_11 SPAN WITH NORMAL RESOLUTION %

    temp1=interp2(mean(data.q11_1(L{i},... %
        :)'',mean(data.n11_1(L{i},... %|SURFACE FITS THE HILL DIAGRAM %
        :))data.etta_1(L{i},:)'',... %|FOR THE %
        q11,n11','cubic',0); %|NOZZLE CONFIGURATION %

    data.surf{i}.n11=n11'; % STORES THE N_11 SPAN %
    data.surf{i}.q11=q11; % STORES THE Q_11 SPAN %
    data.surf{i}.etta=temp1; % STORES THE FITTED EFFICIENCY %
    data.surf{i}.q_min=q_min; % STORES MINIMUM Q_11 %
    data.surf{i}.q_max=q_max; % STORES MAXIMUM Q_11 %
end %

clear n11 q11 q_min q_max temp1 Q L % CLEAR TEMPORARY VARIABLES %

```

APPENDIX G. MATLAB CODE


```

%% ----- FILTERS FOR BEST EFFICIENCY AT ALL Q_11 ----- %
pos(1:3)=1; % SETS THE POSITION IN ALL FITS = 1 %
v=1; % SETS COUNTER = 1 %
L=data.surf{1}.q_min:0.1:data.surf{3}.q_max; % HIGH RESOLUTION Q_11 VECTOR %
S1=data.surf{1}; % IMPORTS SURFACE FIT FOR 1 NOZZLE %
S2=data.surf{2}; % IMPORTS SURFACE FIT FOR 2 NOZZLE %
S3=data.surf{3}; % IMPORTS SURFACE FIT FOR 3 NOZZLE %
data.hill.n11=S1.n11(:,1); % SETS N_11 SPAN FOR COMPLETE HILL %
n11=data.hill.n11; % STORES TEMPORARY N_11 VECTOR %
for i=1:count(L, '>0') % LOOP THROUGH ALL Q_11 POINTS %
    data.hill.q11(1,i)=L(i); %
    for j=1:length(n11) % LOOP THROUGH ALL N_11 POINTS %
%% ----- IF Q_11 IS ONLY FOR 1 NOZZLE ----- %
        if v<count(L, strcat('<', num2str... %
            (data.surf{2}.q_min)))... %
            data.hill.etta(j,v)=... %
            S1.etta(j, pos(1)); % SETS EFFICIENCY IN COMPLETE HILL %
        if j==length(n11) % IF THE Q_11 POINT IS FINISHED %
            pos(1)=pos(1)+1; % MOVES POSITION IN NOZZLE 1 SURFACE %
        end %
%% ----- IF Q_11 IS FOR 1 OR 2 NOZZLE ----- %
        elseif v>count(L, strcat('<', num2str(S2.q_min))) &&... %
            v<count(L, strcat('<', num2str(S3.q_min))) %
            if S2.etta(j, pos(2))>... %
                S1.etta(j, pos(1)) % IF 2 NOZZLES ARE BETTER THEN 1 %
                data.hill.etta(j,v)=... %
                S2.etta(j, pos(2)); % SETS EFFICIENCY IN COMPLETER HILL %
            else % IF 1 NOZZLE IS BETTER THEN 2 %
                data.hill.etta(j,v)=... %

```

```

        S1.etta(j,pos(1));          %|SETS EFFICIENCY IN COMPLETER HILL %
    end                             %
    if j==length(n11)              % IF THE Q_11 POINT IS FINISHED %
        pos(1)=pos(1)+1;          % MOVES POSITION IN NOZZLE SURFACE 1 %
        pos(2)=pos(2)+1;          % MOVES POSITION IN NOZZLE SURFACE 2 %
    end                             %
%%----- IF Q_11 IS FOR 1, 2 OR 3 NOZZLE -----%%
    elseif v>=count(L, strcat('<', num2str(S3.q_min))) &&... %
        v<=count(L, strcat('≤', num2str(S1.q_max))) &&... %
        v<=count(L, strcat('≤', num2str(S2.q_max))) %
        etta_m=S1.etta(j,pos(1)); % SETS NOZZLE 1 AS REFERENCE %
    if S2.etta(j,pos(2))>etta_m    % IF 2 NOZZLES ARE BETTER %
        data.hill.etta(j,v)=... %
        S2.etta(j,pos(2));        %|SETS EFFICIENCY OF COMPLETE HILL %
    elseif S3.etta(j,pos(3))>etta_m % IF 3 NOZZLES ARE BETTER %
        data.hill.etta(j,v)=... %
        S3.etta(j,pos(3));        %|SETS EFFICIENCY OF COMPLETE HILL %
    else                           % IF 1 NOZZLES ARE BETTER %
        data.hill.etta(j,v)=... %
        S1.etta(j,pos(1));        %|SETS EFFICIENCY IN COMPLETER HILL %
    end                             %
    if j==length(n11)              % IF THE Q_11 POINT IS FINISHED %
        pos(1)=pos(1)+1;          % MOVES POSITION IN NOZZLE SURFACE 1 %
        pos(2)=pos(2)+1;          % MOVES POSITION IN NOZZLE SURFACE 2 %
        pos(3)=pos(3)+1;          % MOVES POSITION IN NOZZLE SURFACE 3 %
    end                             %
%%----- IF Q_11 IS FOR 2 OR 3 NOZZLE -----%%

```

```

elseif v>count(L, strcat('<', num2str(S1.q_max))) &&...
    v<count(L, strcat('<=', num2str(S2.q_max)))
    etta_m=S2.etta(j, pos(2));          % SETS NOZZLE 2 AS REFERENCE
    if S3.etta(j, pos(3))>etta_m      % IF 3 NOZZLES ARE BETTER

        data.hill.etta(j, v)=...      %|
        S3.etta(j, pos(3));          %|SETS EFFICIENCY OF COMPLETE HILL

    else                                % IF 1 NOZZLES ARE BETTER

        data.hill.etta(j, v)=...      %|
        S2.etta(j, pos(2));          %|SETS EFFICIENCY IN COMPLETER HILL
    end
    if j==length(n11)                  % IF THE Q_11 POINT IS FINISHED
        pos(2)=pos(2)+1;              % MOVES POSITION IN NOZZLE SURFACE 2
        pos(3)=pos(3)+1;              % MOVES POSITION IN NOZZLE SURFACE 3
    end

%% ----- IF Q_11 IS FOR 3 OR 4 NOZZLE -----
elseif v>count(L, strcat('<', num2str(S2.q_max))) &&...
    v<count(L, strcat('<', num2str(S3.q_max)))
    data.hill.etta(j, v)=S3.etta(j, pos(3)); % SETS EFFICIENCY IN COMPLETE HILL
    if j==length(n11)                  % IF THE Q_11 POINT IS FINISHED
        pos(3)=pos(3)+1;              % MOVES POSITION IN NOZZLE SURFACE 3
    end
end
end
%% -----
end
v=v+1;                                % MOVES COUNTER
end
clear v pos i etta_m S1 S2 S3 N11 Q11 Q_t L % CLEARS TEMPORARY VARIABLES
%% -----

```


Appendix H

Calibration Certificates

H.1 GE Druck P3223-1

CERTIFICATE OF CALIBRATION

DATE OF ISSUE 21 Jan 2009 CERTIFICATE NUMBER 010966256



RUSKA INSTRUMENT CORPORATION
10311 WESTPARK DRIVE,
HOUSTON, TX, USA 77042
PHONE: (713) 975-0547
FAX: (713) 975-6338

APPROVED
SIGNATORIES

K. Kolb
K. Mosher
S. Speich

Page 1 of 6

Client Name : Tormatic AS, Skreppestad
Client Order :
Client Address : 3261
: Larvik, Norway

Instrument : P3223-1
Manufacturer : GE Sensing
Nominal Range : 1 to 350 bar
Certified Range : 1 to 350 bar
Serial Numbers
Base Unit : 66256
10mm Water PCU : X4014
3mm Water PCU : X3084
Weight Set : 66256
Date of Receipt : 12 Dec 2008
Date of Measurement : 12 Dec 2008 To 21 Jan 2009

(Document created using software SICAL2000 (V1.5) CALIBRATION SYSTEM)

Description:-

The items submitted for calibration were as follows:-
1 off Instrument Base.
2 off Piston Cylinder Unit(s) (PCU)
1 off Weight Set(s).

The measurement results are traceable through an unbroken chain of comparisons to reference standards developed and maintained by the National Institute of Standards and Technology, U.S.A., and the National Physical Laboratory, U.K. This certificate may not be reproduced other than in full, except with approval of the issuing laboratory. The reported expanded uncertainty is based on a standard uncertainty multiplied by a coverage factor $k=2$, providing a level of confidence of approximately 95%.

Certified by :

A handwritten signature in black ink, appearing to be 'S. Speich', written over a horizontal line.

CERTIFICATE OF CALIBRATION

CERTIFICATE NUMBER

010966256

Page 2 of 6

EFFECTIVE AREA CALCULATION

PCU S/No. X4014

Method of Calibration

The PCU was cleaned prior to any measurements being taken. During the calibration, the laboratory environment was controlled to 23 +/- 2 degC and 25 - 75 % Relative Humidity. Measurements were made on the the piston for determination of buoyancy volume, fluid head and surface tension effects. The PCU was mounted in an appropriate base and levelled by means of a spirit level mounted on the applied masses with the piston in its floating position. Using the cross float technique, over the calibrated range, comparisons were made of the PCU under test and the calibrated standard PCU. The calibrated standard weights were floated at approximately midway of their range of travel. Rotation was clockwise as viewed from above. The fluid used during cross float was that defined in page note N1. PCU temperature monitoring was by means of an appropriate thermometer in good thermal contact with the PCU assembly. Mass values of floating elements required for the calibration were determined using calibrated weighing machines.

Results of Calibration

In the calibrated range 0.655 - 3.64 MPa the effective area (A_p) sqmm of the PCU at the applied pressure (p) MPa and at a temperature of 20 degC was found to be expressible in the form:

$$A_p = A_o(1 + ap)$$

where:

area at zero pressure $A_o = 80.5779 \quad +/-0.0058 \text{ sqmm}$
and rate of area change $a = 0.0000092 \quad +/-0.0000000 \text{ /MPa}$

Mass value of floating elements : 0.0990536 +/-0.0000020 kg
Buoyancy and fluid head correction: upward force of 0.05013 N
Surface tension correction : downward force of 0.00229 N
PCU Thermal Coefficient : 16.6 ppm/degC

The Pressure Reference level was defined to be :
Top of test port seal.

Page Notes:

- N1. The fluid used was ST55.
- N2. Fluid used for buoyancy, fluid head, and surface tension correction is water.

CERTIFICATE OF CALIBRATION

CERTIFICATE NUMBER

010966256

Page3 of 6

EFFECTIVE AREA CALCULATION

PCU S/No. X3084

Method of Calibration

The PCU was cleaned prior to any measurements being taken. During the calibration, the laboratory environment was controlled to 23 +/- 2 degC and 25 - 75 % Relative Humidity. Measurements were made on the the piston for determination of buoyancy volume, fluid head and surface tension effects. The PCU was mounted in an appropriate base and levelled by means of a spirit level mounted on the applied masses with the piston in its floating position. Using the cross float technique, over the calibrated range, comparisons were made of the PCU under test and the calibrated standard PCU. The calibrated standard weights were floated at approximately midway of their range of travel. Rotation was clockwise as viewed from above. The fluid used during cross float was that defined in page note N1. PCU temperature monitoring was by means of an appropriate thermometer in good thermal contact with the PCU assembly. Mass values of floating elements required for the calibration were determined using calibrated weighing machines.

Results of Calibration

In the calibrated range 6.45 - 36.4 MPa the effective area (A_p) sqmm of the PCU at the applied pressure (p) MPa and at a temperature of 20 degC was found to be expressible in the form:

$$A_p = A_o(1 + ap)$$

where:

area at zero pressure $A_o = 8.05986 \quad +/-0.00058 \text{ sqmm}$
and rate of area change $a = 0.0000013 \quad +/-0.0000000 \text{ /MPa}$

Mass value of floating elements : 0.0242987 +/-0.0000005 kg
Buoyancy and fluid head correction: upward force of 0.00133 N
Surface tension correction : downward force of 0.00073 N
PCU Thermal Coefficient : 11.0 ppm/degC

The Pressure Reference level was defined to be :
Top of test port seal.

Page Notes:

- N1. The fluid used was ST55.
- N2. Fluid used for buoyancy, fluid head, and surface tension correction is water.

CERTIFICATE OF CALIBRATION

CERTIFICATE NUMBER

010966256

Page 4 of 6

MASS DETERMINATION

Weight Set S/No. 66256

Method of Calibration.

During the calibration, the laboratory environment was monitored and recorded.

The mass value of each component was determined on a weight in air basis by applying each mass individually to the receptor of a calibrated weighing machine. Measurements marked with "s" were carried out by using a substitution weighing procedure. The measured values reported in the third column of this certificate represent the mass of a hypothetical weight of density 8000 kg/cu.m which would balance the item identified in the first column in air of density 1.2 kg/cu.m and at 20 degC . The uncertainty associated with each measurement is given in the fourth column.

Results

Identification	Density Assumed (kg/cu.m)	Measured Value (g)	Uncertainty +/- (g)
1 bar (A)	7800	728.731	0.015
10 bar (B)	7800	797.755	0.016
5/50 bar (1)	7800	4109.62	0.08
5/50 bar (2)	7800	4109.64	0.08
5/50 bar (3)	7800	4109.66	0.08
5/50 bar (4)	7800	4109.69	0.08
5/50 bar (5)	7800	4109.66	0.08
5/50 bar (6)	7800	4109.63	0.08
1/10 bar (7)	7800	821.925	0.016
1/10 bar (8)	7800	821.919	0.016
1/10 bar (9)	7800	821.911	0.016
1/10 bar (10)	7800	821.926	0.016
0.5/5 bar (11)	7800	410.966	0.008
0.1/1 bar (12)	7800	82.1930	0.0016
0.1/1 bar (13)	7800	82.1925	0.0016
0.1/1 bar (14)	7800	82.1906	0.0016
0.1/1 bar (15)	7800	82.1910	0.0016

CERTIFICATE OF CALIBRATION

CERTIFICATE NUMBER

010966256

Page 5 of 6

Weight Set S/No.	66256	PCU S/No.	X4014
Std. Gravity	9.80665 m/sec ²	Temperature	20.0 degC
Fluid Density	998.23 kg/cu.m	Surface Tension	0.0728 N/m
Air Density	1.2 kg/cu.m	Weight Density	8000 kg/cu.m
PCU Thermal Coefficient	16.6 ppm/degC		

The Pressure Reference level was defined to be :
Top of test port seal.

Nominal Pressure (bar)	Computed Pressure (bar)	Weight Combination Assumed
1	1.00135	A
5	5.00196	A, 7-10
10	10.0027	A, 1, 7-10
15	15.0034	A, 1-2, 7-10
20	20.0041	A, 1-3, 7-10
25	25.0048	A, 1-4, 7-10
30	30.0054	A, 1-5, 7-10
35	35.0060	A, 1-10

Uncertainty of computed pressure: +/- 0.008%

CERTIFICATE OF CALIBRATION

CERTIFICATE NUMBER

010966256

Page 6 of 6

Weight Set S/No. 66256 PCU S/No. X3084
Std. Gravity 9.80665 m/sec² Temperature 20.0 degC
Fluid Density 998.23 kg/cu.m Surface Tension 0.0728 N/m
Air Density 1.2 kg/cu.m Weight Density 8000 kg/cu.m
PCU Thermal Coefficient 11.0 ppm/degC

The Pressure Reference level was defined to be :
Top of test port seal.

Nominal Pressure (bar)	Computed Pressure (bar)	Weight Combination Assumed
10	9.99991	B
50	49.9957	B,7-10
100	99.9901	B,1,7-10
150	149.984	B,1-2,7-10
200	199.978	B,1-3,7-10
250	249.971	B,1-4,7-10
300	299.963	B,1-5,7-10
350	349.955	B,1-10

Uncertainty of computed pressure: +/- 0.008%

H.2 SeaBird SBE 38



SEA-BIRD ELECTRONICS, INC.

1808 - 136th Place Northeast, Bellevue, Washington 98005 USA

Phone: (425) 643-9866 Fax: (425) 643-9954 www.seabird.com

Temperature Calibration Report

Customer:	Ole A. Nordby AS		
Job Number:	52867	Date of Report:	12/12/2008
Model Number	SBE 38	Serial Number:	3832689-0187

Temperature sensors are normally calibrated 'as received', without adjustments, allowing a determination sensor drift. If the calibration identifies a problem, then a second calibration is performed after work is completed. The 'as received' calibration is not performed if the sensor is damaged or non-functional, or by customer request.

An 'as received' calibration certificate is provided, listing coefficients to convert sensor frequency to temperature. Users must choose whether the 'as received' calibration or the previous calibration better represents the sensor condition during deployment. In SEASOFT enter the chosen coefficients using the program SEACON. The coefficient 'offset' allows a small correction for drift between calibrations (consult the SEASOFT manual). Calibration coefficients obtained after a repair apply only to subsequent data.

'AS RECEIVED CALIBRATION'

Performed Not Performed

Date:

Drift since last cal: Degrees Celsius/year

Comments:

'CALIBRATION AFTER REPAIR'

Performed Not Performed

Date:

Drift since Last cal: Degrees Celsius/year

Comments:

H.3 Weight used during the calibration of the torque transducer

KALIBRERINGSBEVIS
Certificate of calibration
 Nr./No: CAL 016-32/05/1



Kalibreringslaboratoriets navn:
 Name of the calibration laboratory:

JUSTERVEENET
 Oslo justerkammer

Laboratoriets adresse:
 Laboratory address:

Fetveien 66
 2007 KJELLER

Side/Page: 1 av/of: 4
 Ref. til målsprotokoll/Ref. to records

03/270

Tid og sted for kalibrering/ <i>Date and place of calibration:</i>	Bevisets utstedelsesdato/ <i>Date of issue:</i>
Kjeller, 3., 4., 7. og 8. mars 2005	Kjeller, 16. mars 2005
Kalibrering utført av/ <i>Calibration performed by:</i>	Ansvarlig/Responsible:
Arne Geirg Andersen, avdelingsingeniør	Nils M. Thomassen, justermeister

Kunde: NTNU-Vannkraftlaboratoriet, Alfred Getz v. 4, 7161 Trondheim
Customer

Instrument: Lodd
Item

Kapasitet: 2 kg - 6 kg
Capacity

Produsent: Ikke kjent
Manufacturer

Typebetegnelse: Se resultater side 2
Model

Serienummer: Ikke kjent
Serial number

Intern nummer: Se side 2.
Internal number

Tidligere kalibreringsbevis nr.: Ikke tidligere kalibrert ved Oslo justerkammer.
Previous calibration no.

Dette kalibreringsbeviset er utstedt av et laboratorium som er akkreditert i henhold til Norsk Akkreditering (NVA). Akkrediteringen medfører at laboratoriet oppfyller de kravene NVA stiller til kompetanse og kalibreringssystem for de kalibreringene akkrediteringen omfatter. Det innebærer også at laboratoriet har et tilfredsstillende kvalitetsstyringssystem og sporbarhet til akkrediterende eller nasjonale kalibreringslaboratorier. Kopiering av dette kalibreringsbeviset er kun tillatt dersom Ekvivalens Kopiering i sin helhet.

This certificate of calibration is issued by a laboratory accredited by Norwegian Accreditation (NVA). The accreditation states that the laboratory meets the NVA requirements concerning competence and calibration system for all the calibrations included in the accreditation. It also states that the laboratory has a satisfactory quality management system and traceability to accredited or national calibration laboratories. This certificate of calibration may not be reproduced other than in full.

KALIBRERINGSBEVIS

Certificate of Calibration

Justervesenet
Oslo justerkammer

Nr./No.: CAL 016-32/05/1

Side/Page: 2 av/et 4

Måleresultater med usikkerhet:

Nominell verdi	Kjennetegn	Konvensjonell verdi	Usikkerhet (k = 2)	k-faktor ref EA 4/02	V _{eff}
5 kg	NTNU VKL 1	5 kg + 0,33 g	± 0,21 g	k = 2	∞
5 kg	NTNU VKL 2	5 kg + 0,40 g	± 0,21 g	k = 2	∞
5 kg	NTNU VKL 3	5 kg + 0,29 g	± 0,21 g	k = 2	∞
5 kg	NTNU VKL 4	5 kg - 0,31 g	± 0,21 g	k = 2	∞
5 kg	NTNU VKL 5	5 kg + 0,44 g	± 0,21 g	k = 2	∞
5 kg	NTNU VKL 6	5 kg + 0,63 g	± 0,21 g	k = 2	∞
5 kg	NTNU VKL 7	5 kg + 1,00 g	± 0,21 g	k = 2	∞
5 kg	NTNU VKL 8	5 kg + 0,58 g	± 0,21 g	k = 2	∞
5 kg	NTNU VKL 9	5 kg + 0,30 g	± 0,21 g	k = 2	∞
5 kg	NTNU VKL 10	5 kg + 0,74 g	± 0,21 g	k = 2	∞
5 kg	NTNU VKL 11	5 kg + 0,40 g	± 0,21 g	k = 2	∞
5 kg	NTNU VKL 12	5 kg + 0,10 g	± 0,21 g	k = 2	∞
5 kg	NTNU VKL 13	5 kg + 0,08 g	± 0,21 g	k = 2	∞
5 kg	NTNU VKL 14	5 kg + 0,18 g	± 0,21 g	k = 2	∞
5 kg	NTNU VKL 15	5 kg + 0,32 g	± 0,21 g	k = 2	∞
5 kg	NTNU VKL 16	5 kg + 0,20 g	± 0,21 g	k = 2	∞
2 kg	NTNU VKL 21	2 kg - 0,088 g	± 0,088 g	k = 2	∞
2 kg	NTNU VKL 22	2 kg - 0,222 g	± 0,088 g	k = 2	∞
2 kg	NTNU VKL 23	2 kg - 0,221 g	± 0,088 g	k = 2	∞
2 kg	NTNU VKL 24	2 kg - 2,488 g	± 0,088 g	k = 2	∞
5 kg	NTNU VKL 28	5 kg - 1,78 g	± 0,21 g	k = 2	∞
5 kg	NTNU VKL 29	5 kg - 0,91 g	± 0,21 g	k = 2	∞
5 kg	NTNU VKL 30	5 kg - 0,71 g	± 0,21 g	k = 2	∞
5 kg	NTNU VKL 31	5 kg - 0,02 g	± 0,21 g	k = 2	∞
5 kg	NTNU VKL 32	5 kg - 1,40 g	± 0,21 g	k = 2	∞
5 kg	NTNU VKL 33	5 kg - 0,96 g	± 0,21 g	k = 2	∞
5 kg	NTNU VKL 34	5 kg - 0,83 g	± 0,21 g	k = 2	∞
5 kg	NTNU VKL 35	5 kg - 1,31 g	± 0,21 g	k = 2	∞
5 kg	NTNU VKL 36	5 kg - 1,40 g	± 0,21 g	k = 2	∞
5 kg	NTNU VKL 37	5 kg - 1,11 g	± 0,21 g	k = 2	∞
5 kg	NTNU VKL 38	5 kg - 1,50 g	± 0,21 g	k = 2	∞
5 kg	NTNU VKL 39	5 kg - 1,44 g	± 0,21 g	k = 2	∞
5 kg	NTNU VKL 40	5 kg - 1,62 g	± 0,21 g	k = 2	∞
5 kg	NTNU VKL 41	5 kg - 1,28 g	± 0,21 g	k = 2	∞
5 kg	NTNU VKL 42	5 kg - 1,24 g	± 0,21 g	k = 2	∞
5 kg	NTNU VKL 43	5 kg - 1,22 g	± 0,21 g	k = 2	∞
5 kg	NTNU VKL 44	5 kg - 0,40 g	± 0,21 g	k = 2	∞
5 kg	NTNU VKL 45	5 kg - 1,47 g	± 0,21 g	k = 2	∞

Kopiering av dette kalibreringsbeviset er kun tillatt dersom beviset kopieres i sin helhet.
This certificate of calibration may not be reproduced other than in full.

KALIBRERINGSBEVIS

Certificate of Calibration

Justervesenet

Oxfo justeremmer

Nr./No.: CAL 016-32/05/1

Side/Page: 3 av/af 4

Nominell verdi	Kjennetegn	Konversjonell verdi	Usikkerhet (k = 2)	k-faktor ref EA 4/02	V _{eff}
5 kg	NTNU VKL 46	5 kg - 1,47 g	± 0,21 g	k = 2	∞
5 kg	NTNU VKL 47	5 kg - 0,66 g	± 0,21 g	k = 2	∞
5 kg	NTNU VKL 48	5 kg - 0,55 g	± 0,21 g	k = 2	∞
5 kg	NTNU VKL 49	5 kg - 1,01 g	± 0,21 g	k = 2	∞
5 kg	NTNU VKL 50	5 kg - 0,10 g	± 0,21 g	k = 2	∞
2 kg	NTNU VKL 51	2 kg - 0,825 g	± 0,086 g	k = 2	∞
2 kg	NTNU VKL 52	2 kg - 1,005 g	± 0,086 g	k = 2	∞
2 kg	NTNU VKL 53	2 kg - 0,561 g	± 0,086 g	k = 2	∞
2 kg	NTNU VKL 54	2 kg - 0,222 g	± 0,086 g	k = 2	∞
2 kg	NTNU VKL 55	2 kg - 0,103 g	± 0,086 g	k = 2	∞
2 kg	NTNU VKL 56	2 kg - 0,745 g	± 0,086 g	k = 2	∞
2 kg	NTNU VKL 57	2 kg - 0,416 g	± 0,086 g	k = 2	∞
2 kg	NTNU VKL 58	2 kg - 0,202 g	± 0,086 g	k = 2	∞
2 kg	NTNU VKL 59	2 kg - 1,055 g	± 0,086 g	k = 2	∞
6 kg	NTNU VKL 101	6 kg + 153 g	± 0,096 g	k = 4,53	3,24
6 kg	NTNU VKL 102	6 kg - 200 g	± 0,021 g	k = 2,87	4,48

Loddene opplyses ikke spesifikasjoner iht DIML R111 og er derfor ikke vurdert iht denne.

Målemetode:

Substitusjonsveiling, prosedyre JV-LM-MAS-004 utgave nr. 3.1

Spørbarhet:

Loddene er sammenlignet med ioddnormaler som er sporbare til de nasjonale normaler for masse.

Forhold under kalibreringen:

Kalibreringen er basert på en antatt densitet 5000 kg/m^3 på loddene ved $20 \text{ }^\circ\text{C}$ og antatt densitet på $1,2 \text{ kg/m}^3$ på luften.

Temperatur under kalibreringen var fra $19,7 - 20,0 \text{ }^\circ\text{C} \pm 0,1 \text{ }^\circ\text{C}$

Fuktigheten under kalibreringen var fra $47,6 - 49,2 \text{ \% RH} \pm 1,5 \text{ \% RH}$

Måleusikkerhet, metode for beregning og hovedkomponenter:

Den rapporterte utvidede usikkerheten er fastslått som standard måleusikkerhet multiplisert med dekningsfaktor som angitt i tabellen over, som for en t-fordeling med effektive frihetsgrader (V_{eff}) som angitt i tabellen over, korresponderer til en deknings sannsynlighet på tilnærmet 95%. Standard måleusikkerhet har blitt bestemt i samsvar med EA publikasjonen "EA 4/02"

KALIBRERINGSBEVIS

Certificate of Calibration

Justervesenet

Oslo justarkammer

Nr./No.: CAL 016-32/05/1

Side/Page: 4 av/ot: 4

Benyttede instrumenter og normaler:

Temperatur og luftfuktighet ble bestemt ved å benytte termohygrograf, merket T/HYG-05L-08 og T/HYG-05L-02

Den konvensjonelle massen til loaddene ble bestemt ved hjelp av følgende vektter og normaler:

Nominell masse	Benyttet vekt	Benyttet normal
2 kg – 5 kg	Mettler PMS003, serienr. P48583	LM-E-08
6 kg	Sartorius CC60000, serienr. 30003465	LM-E-08

Kommentar:

Resultatet bekrefter loaddets tilstand på det tidspunkt og under de forhold kalibreringen ble utført.
Beregningsprogram Loddkal versjon 2.02